Phase-Sensitive Modified Cyclotron Frequency Measurements of a Single Trapped Antiproton

Master's Thesis

Philip Geißler

Universität Greifswald, Institut für Physik
University of Greifswald, Institute of Physics

2025-05-15

first assessor:	Prof. Lutz Schweikhard
second assessor:	Prof. Stefan Ulmer
supervisors:	Prof. Stefan Ulmer
	Dr. Barbara Latacz
thanks to:	The BASE Team,
	Tim & Kamal

Contents

List of Figures

1 Introduction

The Standard Model of particle physics [1] is the most accurate framework for describing physics at small scales. It has successfully predicted the W, Z, and Higgs bosons before their discovery at CERN, unified the weak and electromagnetic forces [2] and continues to provide consistent descriptions for particle quantities such as the electron and muon magnetic moments from its set of fundamental constants [3, 4].

Penning trap precision experiments offer a unique opportunity to probe these constants [5, 6, 7, 8, 9] and compare experimental results with theoretical predictions. With the Standard Model unable to explain gravity, neutrino masses, dark matter and matter-antimatter asymmetry [10, 11, 12], any observed discrepancies could provide vital clues for physics beyond the Standard Model, guiding new theoretical developments.

Penning traps are essential for these measurements for two reasons: First, such traps can retain charged particles indefinitely in a small volume with negligible power consumption and without interactions with external matter after trapping. They are viable for a multitude of charged particle species, whether produced internally or injected externally, and allow the formation of cold atoms without contaminants [13, 14]. This storage capability facilitates precision measurements of exotic particles [15, 16], including antimatter as used in this thesis. Second, highly optimized Penning traps enable extremely precise measurements, operating with as few as a single particle. This eliminates inter-particle interaction effects, allowing the particle's dynamics to depend solely on its energy and the detail of the electromagnetic field.

Penning Trap Measurements

Penning traps support diverse investigations depending on the stored species: plasmas, molecules, atoms, ions, or single fundamental particles. Historically, these traps were used for particle clouds until Wineland, Ekstrom, and Dehmelt [17] stored a single electron in 1973, enabling the first magnetic moment and charge-to-mass ratio measurements (e.g., [18, 19]). By 1981, Itano and Wineland [20] had also stored a single ion in a Penning trap, achieved in Paul traps a year earlier [21]. As the field matured, similar techniques were extended to other particles.

Potential asymmetries in antiparticle properties are candidates for combined charge, parity, and time-reversal symmetry (CPT) violations, while highly charged ions enhance quantum electrodynamic (QED) effects on electron energy states. Particles bound in exotic atoms, such as muons or antiprotons in helium [22], increase hadronic contributions, and the creation of exotic atoms enables tests of gravitational mass differences between matter and antimatter [23]. Additionally, molecular ions with low-energy vibrational and rotational transitions amplify QED perturbations and facilitate precise charge-to-mass ratio comparisons between electrons and nuclei [24].

Among these developments, two stand out: The first mass spectrometry and magnetic moment measurements of single (anti)protons [25, 26]. By the use of Penning traps, Gabrielse et al. [25] improved the antiproton charge-to-mass ratio precision by multiple orders of magnitude, a result that would initiate the CERN AD program [27]. In the magnetic moment measurement, the absolute frequency shifts from spin-state changes, measured via the continuous Stern-Gerlach effect, are about 10^6 times smaller than for the electron, making it significantly harder to measure. The first successful Penning trap measurement of the proton magnetic moment was achieved in 2014 by Mooser et al. [26] by working with and building on the statistical spin flip detection results of Ulmer [28], and has since been continuously improved by the BASE group.

To contextualize BASE's work within CERN's antimatter research, it is helpful to outline relevant experiments. The Max Planck Institute for Nuclear Physics in Heidelberg houses three precision matter traps. Alphatrap [15, 29] investigates changes in the electron magnetic moment in heavy ions, while µTEx focuses on nuclear magnetic moments of single ions by electron spectroscopy [30, 31]. Charge-to-mass ratios of highly charged ions are measured by Pentatrap [32, 33]. The Florida State University cryogenic Penning trap group, led by E. G. Myers, focuses on charge-to-mass ratios in singly charged ions and molecules [34, 35], a field previously advanced by the MIT group under D. E. Pritchard using the same trap [36]. Unstable ion charge-to-mass ratio measurements are performed by SHIPTRAP [37], JYFLTRAP [38], SMILETRAP [39, 40], TITAN [41, 42], and others, with ISOLTRAP [43, 44] at ISOLDE [45] serving as the other Penning trap group at CERN beside the antimatter experiments.

At CERN, antimatter research is divided into two main areas [46]. One focuses on antimatter gravity measurements, involving the creation and subsequent freefall observation of neutral antiatoms, as performed by experiments such as ALPHA-G [23] and potentially GBAR [47] and AEgIS [48]. Another area explores bound positron energy states, including 1S-2S spectroscopy conducted by ALPHA [49], fine-structure spectroscopy tried by GBAR [50], or hyperfine and antiprotonic helium spectroscopy carried out by ASACUSA [22, 51]. BASE specialises in geonium[1] line-shape spectroscopy [54], pushing the boundaries of precision measurements for fundamental properties of particles.

[1]The ”geonium atom” has been successfully [18, 52] introduced by Brown and Gabrielse [53] as a description of the trapped particle ”electrons” in the field of the external electrode ”nucleus”.

BASE Charge-to-Mass Ratio and Magnetic Moment Measurements

The central measured quantities of the BASE collaboration are the magnetic moment and charge-to-mass ratio of both protons and antiprotons [5, 6]. The antiproton experiment is located at CERN, as it is the only entity capable of providing trappable antiprotons, while the proton experiments are operated in Mainz and soon Düsseldorf, Germany. They are located in university laboratories separately from BASE CERN to escape unnecessary electromagnetic field fluctuations from active accelerator operation [55]. BASE is currently in the process of building BASE-STEP [56], a transportable Penning trap, to move antiprotons outside of CERN and to Düsseldorf [57]. The following paragraphs only give a surface-level overview of the two main measurements done at BASE CERN, with more details in the relevant publications [5, 6, 58] and a general overview in [54].

In the relative charge-to-mass ratio comparison of the proton and antiproton [6, 59], Geonium spectroscopy measurements are performed on antiprotons and hydrogen anions rather than directly on antiprotons and protons. Since they are both negatively charged, they can be compared in succession inside the same Penning trap, minimizing potential trap parameter changes between the measurements at the cost of systematic frequency shifts from the proton-electron interactions [60, 61, 62]. During the measurement sequence, both particles are continuously shuttled between the precision trap and their parking position. The particle's cyclotron frequency, $\omega_c = \frac{q}{m}B$, is proportional only to its charge-to-mass ratio and the magnetic field inside the trap. Although the magnetic field is slowly drifting over time, it remains very stable over the short time intervals used for the cyclotron frequency measurements. The cyclotron frequency ratio of the two particles thus allows a direct measurement of their relative charge-to-mass ratios up to systematic shifts. At a value of $-1.000\,000\,000\,003(16)$ [6], the results are consistent with one at a precision of 16 parts per trillion[2] making them the most precise test of CPT invariance to date.

In the magnetic-moment measurements of the antiproton [5, 58], cyclotron frequency measurements are again used as a reference measurement. Together with the spin-precession Larmor frequency ω_L, it allows the calculation of the antiproton magnetic moment from prior knowledge of the nuclear magneton[3] $\mu_\mathrm{N} = e\hbar / 2m_{\bar{p}}$. BASE actually measures the antiproton g-factor $g_{\bar{p}} = 2\omega_L / \omega_c = 2\mu_{\bar{p}} / \mu_\mathrm{N}$, removing the dependence on μ_N. Relating the magnetic moment $\mu_{\bar{p}}$ to the nuclear magneton $\mu_\mathrm{N} = \frac{m_e}{m_{\bar{p}}}\mu_\mathrm{B}$ is analogous to referencing the electron magnetic moment to the Bohr magneton μ_B, which specifies the axial magnetic moment increments with the orbital magnetic quantum number of a hydrogen atom. For the measurements of ω_c and ω_L, a multi-trap scheme is used [63].

---

[2] These results were achieved at absolute cyclotron frequency scatters of about 50 mHz in the sideband (Section 2.3.4) or 25 mHz in the peak campaign (Section 2.2.1).

[3] The nuclear magneton is ordinarily defined relative to the proton mass m_p. At BASE, the equivalent definition relative to the antiproton mass $m_{\bar{p}}$ is used since with this definition, the antiproton g-factor can be measured directly by the ratio of the Larmor frequency to the cyclotron frequency, It also separates potential proton-antiproton charge-to-mass ratio differences from magnetic-moment-to-mass ratio differences.

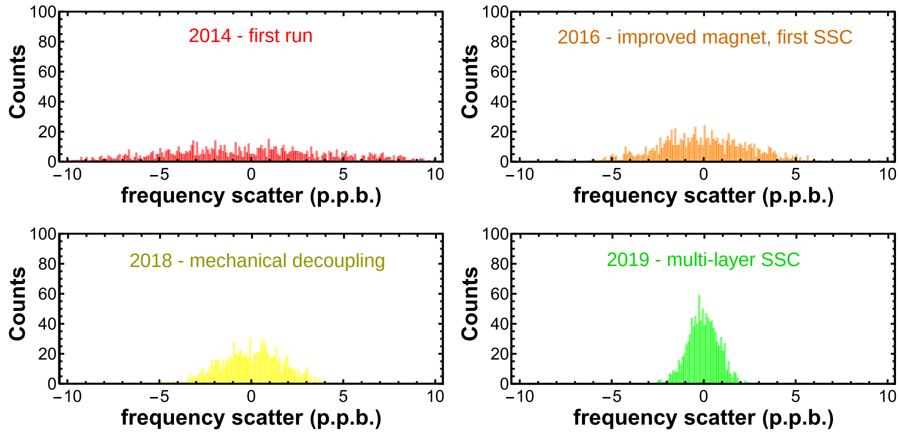

Figure 1.1: Successive upgrades to the BASE experiment have continuously improved the cyclotron frequency scatter, to the point where the current frequency estimation method (see Section 2.2.2) is the limiting factor. Afterwards, excluding phase-sensitive detection methods, further improvements like magnetic field shimming and the implementation of the cooling trap have optimized the measurement sequences further without direct effects on the cyclotron scatter. The four plots are taken from [65] and show peak-method data.

One Penning trap is located within a maximally homogeneous magnetic field, while the other has a strong magnetic bottle superimposed. Inside the homogeneous trap, one particle is continuously used to measure ω_c. Due to the interaction with the detection circuit, the cyclotron mode of the particle is somewhat hot. In the other trap, the two antiproton spin states of the other particle have different energy levels due to the continuous Stern-Gerlach effect, which can be determined from the resulting axial frequency shifts [64]. By radiating a broadband drive at roughly ω_L, the spin state can also be changed, and together with the spin state detection thus initialized in a known state [28]. Temporarily moving it into the homogeneous trap, the Larmor resonance becomes very sharp due to its sub-thermal cyclotron energy together with the best achievable energy independence of the cyclotron frequency. The Larmor frequency can then be determined by driving the Larmor resonance at multiple candidate frequencies and maximizing the spin-flip probability, or fitting the correct spin flip probability distribution [52].

In 2016, the trap stack was moved into a new magnet of improved homogeneity and a superconductive shielding coil (SSC) [66] was wrapped around the trap to counteract external electromagnetic fluctuations. 2018 saw the mechanical decoupling of the 4 K trap stack from the helium cryostats by tensioning it to the outer shielding with kevlar fibres [67], after which the shielding system was expanded to multiple shielding and shimming coils [68] in 2019. Each upgrade has improved the magnetic field stability inside the homogeneous trap, and thus the cyclotron frequency scatter shown in Fig. 1.1. Now, the antiproton g-factor resonance is limited by the cyclotron frequency estimation method. The last published result from 2017 constrains $g/2$ to a value of $-2.792\,847\,344\,1(42)$ with a relative precision of 1.5 parts per billion [5], with further improvements of the cyclotron frequency scatter up to 2019 further decreasing the uncertainty of g.

The Goal of this Thesis

In both measurements, improved cyclotron frequency estimation measurements will directly affect the attainable precision limits. The cyclotron frequency $\omega_c^2 = \omega_-^2 + \omega_z^2 + \omega_+^2$ depends on the values of the three Geonium mode frequencies $\omega_- \ll \omega_z \ll \omega_+$, with their shift and uncertainty contributions $\Delta\omega_c = \frac{\omega_-}{\omega_c}\Delta\omega_-$, $\frac{\omega_z}{\omega_c}\Delta\omega_z$, and $\frac{\omega_+}{\omega_c}\Delta\omega_+$ introducing a resulting uncertainty in ω_c. Due to the strong suppression of any uncertainties in ω_- from the scaling factor, a periodical estimation of ω_- already reduces their effect to insignificance. With ω_z located in an easy-to-work-with RF frequency range with high quality-factor resonators, ω_z can be determined quickly and to a high precision. Finally, the uncertainties in the modified cyclotron frequency ω_+ are neither suppressed nor as small as the uncertainties of ω_z. Thus, a precise measurement technique for the modified cyclotron frequency is paramount to improvements in BASE's measurements.

This thesis introduces the theoretical foundations of Penning trap measurements, going into detail about how the confined particle interacts with the detection circuitry and is itself affected by the drives able to be radiated into the experiment. It explores how the particle's mode frequencies are measured, how the particle dynamics behave when those modes are coupled, and how to extend the frequency measurements to include the oscillation phases (phase measurements). Building on the theoretical foundation, a test setup is presented to test the signal phase acquisition and characterize estimated frequency uncertainties as a function of the signal-to-noise ratio and phase measurement number. The experimental section continues with the measurement procedures for obtaining cyclotron phase data and the implementation of necessary instruments into the BASE electronics setup. It focuses on optimizing these measurements, addressing challenges encountered, and culminating in an improved measurement technique that enhances frequency precision by a factor of three over current methods. A dedicated chapter addresses systematic effects impacting the BASE g-factor measurement, done by the BASE group in parallel to the phase method implementation.

The phase-sensitive modified cyclotron frequency apparatus has been successfully assembled and installed in the BASE experimental zone. With CERN's decelerators shut down, this work promises to enable the most precise cyclotron frequency measurements ever conducted at BASE. In the short time that both decelerators came to an unplanned halt during the writing of this thesis, they were already optimized to a level that improved the cyclotron scatter, and will thus also improve the g-factor resonance, by a factor of roughly two.

2 Particle Detection Theory

This chapter summarizes the theory on how charged particles can be trapped inside a static electro-magnetic field, what behaviour this confinement creates, and how the effects of such behaviour can be modified and probed via external circuitry connected to the trap. Subsequently, two methods of particle frequency probing are explained in detail: passive (dip methods) and active (peak methods). Both methods have their own advantages and disadvantages, and method specific considerations, which are discussed. Relevant for this thesis, and for initial preparation of the BASE antiprotons, the concept of mode coupling is introduced and extended to cover thermalization and the intricacies of coupling at the mode sidebands. Sideband coupling will be used extensively in phase sensitive measurements for particle preparation and read-out.

2.1 Confined Particles in Penning Traps

The simplest way to confine a charged particle would be to create a potential well by means of an external electro- or magnetostatic field in which the particle is stationary and trapped indefinitely. However, such a field is forbidden by Earnshaw's Theorem [69], and one of three concessions must be made for successful confinement: Either the field has both electric and magnetic components, is non-static, or the particle will not be classically stationary. Each option has since grown to its own particle confinement field with different applicability regimes. Nonstationary magnetic confinement is commonly used in high-temperature fusion experiments, where the increased confinement volume benefits heat retention [70]. Paul traps use nonstatic quadrupolar electric fields [71] while Penning traps use a superimposed magnetic field to trap small particle clouds or even single particles [72]. Paul traps are generally less expensive, as they do not require large magnets to produce a homogenous magnetic field. Furthermore, there is no field in the centre of the trap, so the particle's motion is relatively unconstrained at the microscopic scale and multiple particles can interact with each other. Use cases of Paul traps include atomic clocks and quantum computing [73, 74]. Penning traps force the trapped particle into microscopic orbits, whose shapes and frequencies are determined by its fundamental properties, which can be determined by measuring those frequencies. BASE uses Penning traps to determine the g-factor and charge-to-mass ratio of the antiproton, so they are subsequently explained in further detail.

2.1.1 The Ideal Penning Trap

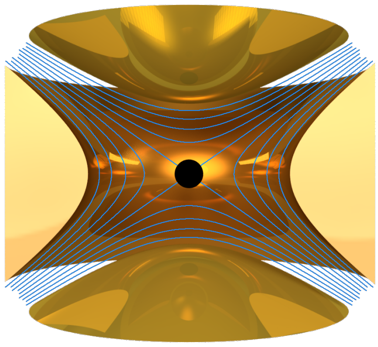

Figure 2.1: The ideal Penning trap with its hyperbolic electrodes. Some crossections of equipotential surfaces are highlighted in blue.

The Penning trap achieves particle confinement by superimposing a constant axial magnetic field $B(\vec{r}) = B_0\hat{e}_z$ on an electrostatic quadrupolar potential rotationally symmetric around the z-axis.

$$\vec{B} = B_0\hat{e}_z \qquad \Phi(z,\rho) = \left(z^2 - \frac{\rho^2}{2}\right)\Phi_2 \tag{2.1}$$

$$\vec{E}(z,\rho) = \left(\rho\hat{e}_\rho - 2z\hat{e}_z\right)\Phi_2 \tag{2.2}$$

Φ_2 is the radial, and half the axial curvature of $\Phi(\vec{r})$ around $\vec{r} = 0$. The relative scaling of the radial and axial components follows from Poisson's Equation: $\nabla^2\Phi = \nabla \cdot (3\vec{z} - \vec{r}) = 3 - 3 = 0$. The homogeneous magnetic field can be created by an infinite solenoid, Helmholtz coils, or some other current configuration, while the electric field can be recreated by working backwards from the potential and manufacturing electrodes with surfaces coincident to a set of equipotential surfaces of Φ. Such an electrode geometry is shown in Fig. 2.1, creating an imperfect hyperbolic Penning trap due to the finite extent of the electrodes. By placing radial and axial electrodes such that their closest point has a distance of ρ_0 and z_0 to the trap centre and applying a voltage U_0 between them, Φ can be rewritten as

$$\Phi(z,\rho) = \frac{z^2 - \frac{1}{2}\rho^2}{z_0^2 + \frac{1}{2}\rho_0^2} U_0 + c\,. \tag{2.3}$$

Using the Lorentz force, the particle's three equations of motion can be obtained.

$$\begin{aligned} m\ddot{\vec{r}} &= q\dot{\vec{\rho}} \times \vec{B} + q\vec{E} \\ &= qB_0\,\dot{\vec{r}} \times \hat{e}_z - q\Phi_2(3\vec{z} - \vec{r}) \end{aligned} \quad \Longrightarrow \quad \begin{aligned} 0 &= \tfrac{m}{q}\ddot{x} - B_0\dot{y} - \Phi_2 x \\ 0 &= \tfrac{m}{q}\ddot{y} + B_0\dot{x} - \Phi_2 y \\ 0 &= \tfrac{m}{q}\ddot{z} + 2\Phi_2 z \end{aligned} \tag{2.4}$$

Ignoring the effect of the potential curvature Φ_2 on the radial planar motion results in familiar terms for cyclotron motion and motion in a harmonic oscillator, with sinusoidal solutions $c_1\cos(\omega_i t + c_2)$.

$$\ddot{z} = \frac{qE_z}{m} = -2\frac{q}{m}\Phi_2 \cdot z = -\omega_z^2 \cdot z \qquad \omega_z := \sqrt{2\tfrac{q}{m}\Phi_2} \tag{2.5}$$

$$\begin{pmatrix}\ddot{x}\\ \ddot{y}\end{pmatrix} = \frac{q}{m}B_0 \cdot \begin{pmatrix}\dot{y}\\ -\dot{x}\end{pmatrix} = -\left(\frac{q}{m}B_0\right)^2 \cdot \begin{pmatrix}x\\ y\end{pmatrix} = -\omega_c^2 \cdot \begin{pmatrix}x\\ y\end{pmatrix} \qquad \omega_c := -\tfrac{q}{m}B_0 \tag{2.6}$$

It is of note that for the magnetic field in the positive z-direction, the rotation of a positive particle inside the xy-plane is mathematically negative, so ω_c is also negative. However, ω_c in this thesis subsequently refers to $+\frac{q}{m}B_0$. Including the radial effect of Φ_2 does not change the axial behaviour, and the planar and axial motions remain separable.

Introducing the in-plane radial vector $\vec{\rho} = \rho\hat{e}_\rho = x\hat{e}_x + y\hat{e}_y$, the planar motion can be written as

$$0 = \ddot{\vec{\rho}} - \frac{q}{m}B_0\begin{pmatrix} 0 & 1 \\ -1 & 0 \end{pmatrix}\dot{\vec{\rho}} - \frac{q}{m}\Phi_2\vec{\rho} = \ddot{\vec{\rho}} + \omega_c\begin{pmatrix} 0 & 1 \\ -1 & 0 \end{pmatrix}\dot{\vec{\rho}} - \frac{\omega_z^2}{2}\vec{\rho}, \tag{2.7}$$

and the cyclotron motion is perturbed by the electrostatic potential, vanishing as ω_z approaches 0. In both the perturbed and unperturbed cases, a circular orbit of constant velocity exists as a solution of Eq. (2.7). Larger values of ω_z decrease the total force at a given radius, decreasing the orbit curvature and thus increasing the radius of the particle's orbit. Consequently, the orbit's angular frequency decreases as the cyclotron motion $\vec{\rho}_+$ is impeded by the quadrupolar potential, reducing ω_c to its perturbed value ω_+, designated as the modified cyclotron frequency. If $\omega_z \ll \omega_c$, then $\ddot{\vec{\rho}}_+ \approx \omega_c^2\vec{\rho}_+$ is much larger than $\frac{1}{2}\omega_z^2\vec{\rho}_+$, and the total force and thus ω_+ is reduced.

$$\omega_+ \approx \left(1 - \frac{\omega_z^2}{2}\frac{|\vec{\rho}_+|}{|\ddot{\vec{\rho}}_+|}\right)\omega_c = \left(1 - \frac{\omega_z^2}{2\omega_c^2}\right)\omega_c = \omega_c - \frac{1}{2}\frac{\omega_z^2}{\omega_c} \qquad \text{for } \omega_z \ll \omega_c \tag{2.8}$$

If the modified cyclotron motion is not centred inside the trap, but at $\vec{\rho}_-$, the Coulomb force of the quadrupolar potential will try to accelerate the particle outwards. Over one cyclotron orbit, the resultant variation in orbital speed causes the particle to $\vec{E}\times\vec{B}$-drift with an approximate mean velocity $\vec{v}_D$ perpendicular to both the electric and magnetic fields [75]. v_D is most accurate if $\omega_z \ll \omega_c$. Since $\vec{E}$ is symmetric under rotation around the z-axis, so is the drift motion, causing a secondary orbit with angular frequency ω_-, designated as the magnetron frequency.

$$\omega_- \approx \frac{v_D}{\rho_-} = \frac{|\vec{E}\times\vec{B}\,|}{B_0^2\rho_-} = \frac{\Phi_2 B_0\rho_-}{B_0^2\rho_-} = \frac{\omega_z^2}{2\omega_c} \qquad \text{for } \omega_z \ll \omega_c \tag{2.9}$$

Recognizing the circular nature of both motions allows solving for ω_+ and ω_- analytically with the ansatz $\vec{\rho}(t) = \rho_0\binom{\cos\omega t}{\sin\omega t}$. Inserting this into Eq. (2.7) yields the equation $0 = \omega^2 - \omega_c\omega + \frac{1}{2}\omega_z^2$ with the exact solutions

$$\omega_\pm = \frac{1}{2}\left(\omega_c \pm \sqrt{\omega_c^2 - 2\omega_z^2}\right). \tag{2.10}$$

The approximate equations Eqs. (2.8) and (2.9) gained from physical intuition approximate the correct result under the $\omega_z \ll \omega_c$ assumption. Equation (2.10) yields the identities

$$\omega_c = \omega_+ + \omega_- \qquad \omega_z^2 = 2\omega_+\omega_- \tag{2.11}$$

that combine to give ω_c^2.

$$\omega_c^2 = \omega_+^2 + 2\omega_+\omega_- + \omega_-^2 = \omega_+^2 + \omega_z^2 + \omega_-^2 \tag{2.12}$$

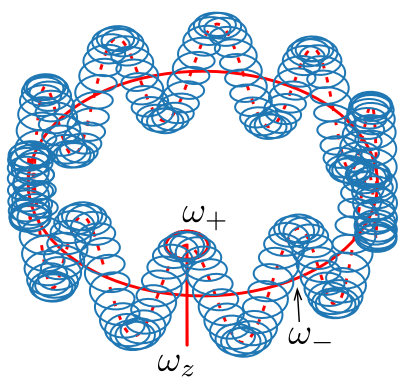

Figure 2.2: The particle's orbit inside the Penning trap is the superposition of its three fundamental oscillations. They result from axial harmonic motion inside the quadrupolar potential, and radial cyclotron and magnetron motion. For illustrative purposes, neither the frequencies not the amplitudes of the motions are to scale.

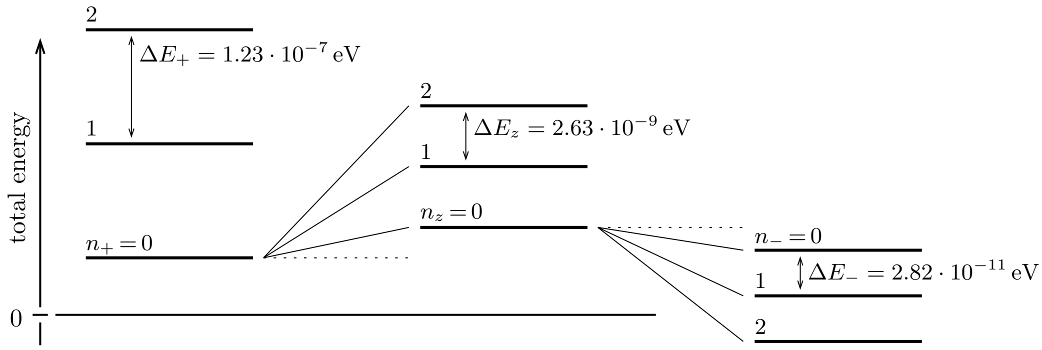

Figure 2.4: The energy level diagram of the trapped particle inside the BASE precision trap results from the energy contributions of the modified cyclotron, axial and magnetron modes. Due to the different energy scales, each subsequent mode acts only as an energy perturbation of the previous one. The magnetron mode is metastable, and increases in magnetron quantum number decrease the total energy, leading to eventual particle loss if the magnetron mode is allowed to thermalize.

This identity, called the Brown-Gabrielse invariance theorem, holds even for nonzero trap misalignment angles and elliptical traps [76]. Because of that, it is used extensively for the cyclotron frequency determination at BASE.

The relationship between ω_z, ω_-, and ω_+ depends on the axial and radial confinement, determined by Φ_2 and B_0. Penning traps normally operate in the regime of strong magnetic confinement in which $\omega_z \ll \omega_c$, so $\omega_- \ll \omega_z \ll \omega_+$. By increasing the voltage on the electrodes, or decreasing the magnetic field, ω_z can be increased until it is greater than ω_+, or even until the two radial modes degenerate and become unstable at $\sqrt{2}\omega_z \geqslant \omega_c$. This behaviour can be used to remove all particles below a critical charge-to-mass ratio from the trap by intentionally increasing the electrode voltage. In the course of the cleaning procedure, the remaining ions of a slightly higher charge-to-mass ratio may temporarily traverse $\omega_z = \omega_+$ at $\omega_z = \frac{2}{3}\omega_c$, where the axial and modified cyclotron mode will couple according to Section 2.3 with a degenerated sideband, exchanging energy without any external influences.

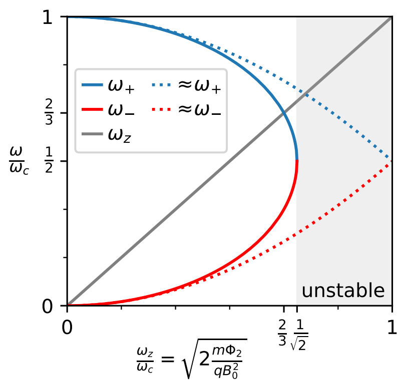

Figure 2.3: The ordering of the frequencies ω_z, ω_-, and ω_+ varies depending on the trap parameters Φ_2 and B_0 [77]. Equations (2.8, 2.9) are good approximations for $\omega_\pm$ only if $\omega_z \ll \omega_c$.

As the particle oscillates in its axial mode, its total energy E_z oscillates with frequency $2\omega_z$ between the kinetic and potential energy, analogous to any other harmonic oscillator. It can thus be calculated by looking at the maximum amplitude $\hat{z}$ or velocity $\hat{\dot{z}}$ only, where E_z is concentrated into one form. Looking at pure modified cyclotron or magnetron motion, the radius $\rho_\pm$ from the trap centre stays constant, so the potential energy $-\frac{1}{2}q\Phi_2\rho^2$ does too. If the combined motion is to be treated independently for the two modes, its potential energy E_{pot} must scale as the sum of the potential energies of the two pure motions.

$$\begin{aligned}\langle E_{\text{pot}}\rangle &= -\frac{q\Phi_2}{2}\left\langle\left(\rho_+\left(\begin{smallmatrix}\cos\omega_+ t\\ \sin\omega_+ t\end{smallmatrix}\right) + \rho_-\left(\begin{smallmatrix}\cos\omega_- t\\ \sin\omega_- t\end{smallmatrix}\right)\right)^2\right\rangle \\ &= -\frac{q\Phi_2}{2}\left\langle\rho_+^2 + \underbrace{2\rho_+\rho_-\cos\big((\omega_+-\omega_-)t\big)}_{\to 0 \text{ as } T_{\text{avg}}\to\infty} + \rho_-^2\right\rangle = -\tfrac{1}{2}q\Phi_2\rho_+^2 - \tfrac{1}{2}q\Phi_2\rho_-^2\end{aligned}$$

The kinetic energy is given by the velocity $v_\pm = \omega_\pm\rho_\pm$ defined by ρ as well. Putting everything together yields

$$E_z = \tfrac{m}{2}\dot{z}^2 + q\Phi_2 z^2 = \tfrac{m}{2}\hat{\dot{z}}^2 = \tfrac{m}{2}\omega_z^2\hat{z}^2 > 0 \tag{2.13}$$

$$E_+ = \tfrac{m}{2}\omega_+^2\rho_+^2 - \tfrac{1}{2}q\Phi_2\rho_+^2 = \tfrac{m}{2}\left(\omega_+^2 - \tfrac{1}{2}\omega_z^2\right)\rho_+^2 > 0 \quad \text{if } \sqrt{2}\omega_z < \omega_c \tag{2.14}$$

$$E_- = \tfrac{m}{2}\omega_-^2\rho_-^2 - \tfrac{1}{2}q\Phi_2\rho_-^2 = \tfrac{m}{2}\left(\omega_-^2 - \tfrac{1}{2}\omega_z^2\right)\rho_-^2 < 0 \quad \text{if } \sqrt{2}\omega_z < \omega_c\,. \tag{2.15}$$

At stable Penning trap parameters, the magnetron mode is thus only metastable, and ρ_- increases indefinitely if it can release its energy[1]. The inversion of the magnetron energy levels means that during mode coupling the absorption and emission of energy quanta have the exact opposite effect at a given coupling frequency, so upper and lower coupling sidebands need to be switched when working with the magnetron mode (see Section 2.3).

2.1.2 Cylindrical Penning Traps

Manufacturing the electrodes of the ideal Penning trap shown in Fig. 2.1 is difficult due to the parametric nature of the electrode surfaces. While hyperbolic surfaces are rotationally symmetric, they require curved toolpaths and modifications to the theoretical shape for assembly and particle injection. Cylindrically symmetric electrodes with rectilinear cross-sections would simplify the manufacturing process and could be made to much higher standards, but could not perfectly recreate the quadrupolar field without higher-order contributions, since the outer equipotential surfaces are given by the electrode shape. However, a long stack of many such electrodes as in Fig. 2.5 can be optimized to suppress the first higher orders in the trap center, leaves a convenient collinear access point to the trap centre along the magnetic field line for particles to be inserted and allows the creation of multi-trap assemblies such as the one shown in Fig. 4.2 [78].

[1] Thermalization effects concerning the magnetron mode are quite counterintuitive, and the author does not claim to understand them. When coupling the magnetron mode to any other system able to store energy, will this system then indefinitely absorb the magnetron mode energy or not? For two systems with positive energy levels, their expected energy relative to their ground state equalizes during thermalization. However, the magnetron mode has no ground state and as such no equilibration can be referenced against it. In practice, it suffices to say that coupling the particle to a resonator at magnetron frequency will allow the magnetron mode to dissipate enough energy for the particle to be lost [53].

For any such trap stack, each electrode contributes to the trap's total potential. These electrode-specific potential contributions can be calculated by solving for the potential in the trap stack where all but the respective electrode is grounded. At the position of the confined particles, the total potential Φ can then be approximated by the sum of the scaled axial Taylor expansions of all electrode contributions, revealing how the electrodes need to be biased to optimize Φ to be parabolic with minimal linear and higher-order coefficients. The radial behaviour follows from the axial expansion and Laplace's equation.

If the trap is symmetrical, and the corresponding electrode pairs are biased equally, the odd orders of all potential contributions vanish, and Φ is intrinsically harmonic up to the third order. The lengths and potentials of the electrodes can then be optimized to minimize the higher even orders and maximize the harmonicity of Φ. In any such trap, neither the trap dimensions nor the trap voltages will change the sign of any higher-order potential term if uniformly scaled. By referencing the trap dimensions to the electrode radius R and the trap voltages to the central electrode voltage V_R, the optimized values will hold for all sizes and voltages of topologically equivalent cylindrical trap stacks.

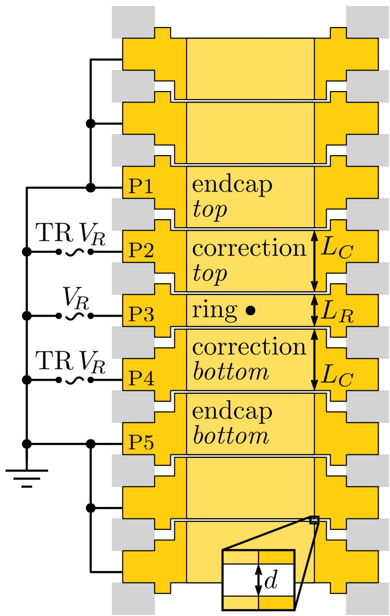

Figure 2.5: Cylindrical Penning traps consist of symmetrical stacks of electrodes at voltages emulating the ideal potential from Eq. (2.1). Due to manufacturing constraints on electrode variety, the endcap electrodes consist of three identical connected correction electrodes.

BASE currently uses symmetrical five-electrode traps with long grounded outer electrodes, using nomenclature consistent with the precision trap shown in Fig. 2.5, where the tuning ratio (TR) specifies the ratio between the correction and ring electrode voltages. The outer electrodes consist of three connected rings identical to the correction electrodes. They do not necessarily need to, and splitting them into more symmetric pairs would grant greater freedom in optimizing higher-order contributions of Φ [79]. In this thesis, as in [68, 80, 81], the i-th normalized coefficients of Φ and the correction and ring electrode potential contributions Φ_C and Φ_R are denoted as $C_i = D_i\mathrm{TR} + E_i$, D_i, and E_i. The following equations, taken from [68], show how Φ is constructed from its scaled components.

$$
\begin{array}{r}
\Phi_R(z) = \left(E_2 z^2 + E_4 z^4 + E_6 z^6 + E_8 z^8 + \mathcal{O}(z^{10})\right) V_R \\
+\ \Phi_C(z) = \left(D_2 z^2 + D_4 z^4 + D_6 z^6 + D_8 z^8 + \mathcal{O}(z^{10})\right) V_R \cdot \mathrm{TR} \\
\hline
\Phi(z) = \left(C_2 z^2 + C_4 z^4 + C_6 z^6 + C_8 z^8 + \mathcal{O}(z^{10})\right) V_R
\end{array}
\tag{2.16}
$$

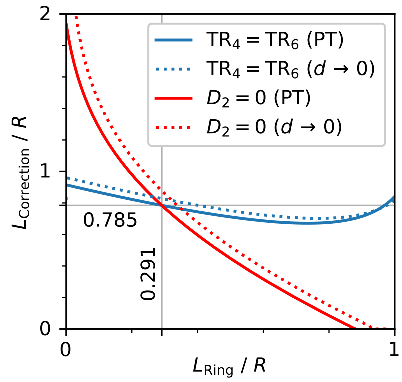

Figure 2.6: The working parameters of an orthogonal and compensated five-pole trap depend on its trap radius R and the electrode separation d. For the precision trap (PT), $d/R \approx 3.1\,\%$ and optimal electrode lengths decrease [68].

With the five-electrode geometry of the traps used at BASE and most other contemporary Penning trap experiments [28, 82, 83], three degrees of freedom remain to be used for trap optimization, namely TR, L_R/R, and L_C/R. Any optimization needs to take into account that the electrodes are separated from each other by a distance d to avoid short circuits. However, d is normally much smaller than R, only slightly changing the optimal parameters of an ideal cylindrical trap. Intuitively, the free parameters should be optimized to find a TR where $C_2 > 0$ and $C_4, C_6, C_8 = 0$ (compensation to eighth order), as the lowest order anharmonicities have the largest effect on the particle's frequencies. The axial frequency $\omega_z \propto C_2$ of such a trap would scatter with voltage fluctuations of any of the 3 electrodes. Abandoning the $C_8 = 0$ constraint allows optimizing for $D_2 = 0$ (orthogonality) instead, with two positive effects: A variation of the tuning ratio sometimes needed for measurements does not shift ω_z[2], and the frequency scatter contributions from the correction electrodes are suppressed, decreasing the voltage noise ω_z frequency scatter by a factor[3] of $\sqrt{3}$. Optimizing for orthogonality and compensation up to the sixth order yields a unique point in the parameter space, shown in Fig. 2.6 and with a TR of 0.881.

Equivalent unnormalized coefficients are defined for the axial component of the magnetic field, again relying on its axial symmetry, source- and curl-free nature and Laplace's equation to determine the radial behaviour and radial components, too.

$$B_z(z) = B_0 z^0 + B_1 z^1 + B_2 z^2 + B_3 z^3 + \mathcal{O}(z^4) \tag{2.17}$$

General optimization of these coefficients towards a perfectly homogenous magnetic field is usually left to the suppliers of the trap-encompassing magnet providing the dominant axial magnetic field of the Penning trap. Additionally, shimming coils can be wound around the trap stack to actively tune the lowest order magnetic field coefficients [68]. Special uses of Penning traps necessitate strong magnetic field curvature ($B_2 L_\mathrm{Ring} \sim B_0$), in which ferromagnetic electrode materials are chosen to create the necessary magnetic bottles (see Section 4.1.1, AT) [5, 58]. Resulting frequency shifts from imperfect electric and magnetic fields are presented and derived in [53, 81, 84, 85].

[2] In reality, due to manufacturing uncertainties and field inhomogeneities, changes in tuning ratio still shift ω_z, but the effect is strongly suppressed relative to a non-orthogonal trap.

[3] Since D_2 is both zero and the sum of the second-order Taylor coefficients D_{2t}, D_{2b} of the top and bottom correction electrodes, which are equal due to symmetry, both D_{2t} and D_{2b} are must be zero as well. Thus, for a vanishing D_2, $\sigma^2_{\omega_z} \propto \sigma^2_{E_2 V_R} + \sigma^2_{D_{2t} V_{Ct}} + \sigma^2_{D_{2b} V_{Cb}} = \sigma^2_{E_2 V_R} + 0 + 0$, and $\sigma^2_{\omega_z}$ is reduced by a factor of 3 relative to the case in which $E_2 \sim D_2$ and TR ~ 1.

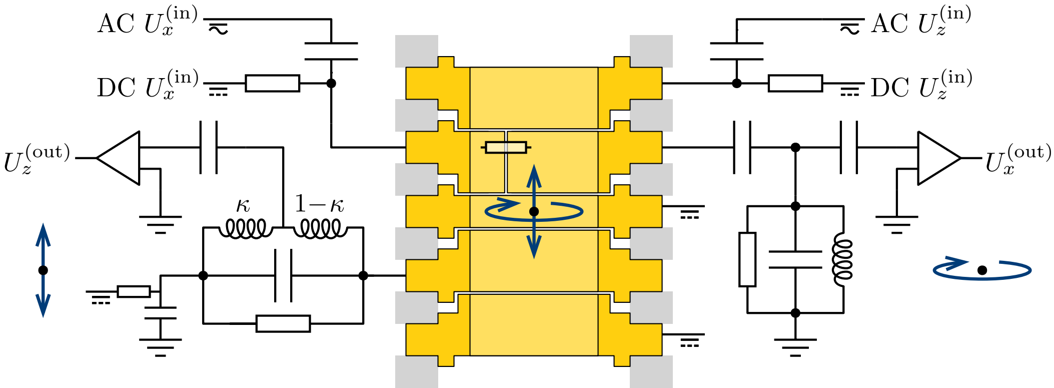

Figure 2.7: The BASE precision trap detection circuitry connects to the trap electrodes. The axial and radial resonators are connected to one of the correction electrodes to detect surface charge changes caused by the particle's motion. The radial detection electrode is split to break its radial symmetry so the radial motion leads to changes in surface potential. Multiple amplification stages then amplify a fraction κ of the resonator voltage to ground before it is fed into a signal analyzer, where κ is the fraction of the total resonator inductance at which the resonator is tapped. Decreasing κ will decrease the detection signal-to-noise ratio (SNR) with the upside of a broader dip width [86]. An axial and radial drive AC $U_i^{(\mathrm{in})}$ are connected to two electrodes to actively interact with the particle. All electrodes are DC-biased, explicitly shown for the drive electrodes, and otherwise by direct connection. The axial detection electrode is a special case and biased over the resonator.

2.2 Non-Destructive Particle Detection and Measurement

The three motional frequencies in a Penning trap are influenced by the particle's state via a multitude of correction terms and can be determined to a very high precision via downconversion interference, so they are a prime detection target for most Penning trap experiments. Since the particle induces surface currents in the trap electrodes at harmonics of its motional frequencies, measuring the surface currents enables the determination of the motional frequencies. If the electrodes are kept at a constant potential, then the surface currents only propagate outside of the electrode to ground if the electrodes are not symmetric to the mode oscillations. Otherwise, all induced currents are internal to the electrode. By connecting a resonator circuit with resonance frequency ω_{Res} to the electrodes, the surface currents of the mode close to ω_{Res} will be selectively amplified. Together with a subsequent amplifier chain, the resonator increases the surface currents from a few femtoampere to a scale detectable using over-the-counter signal analyzers. An example of such detection circuitry is shown in Fig. 2.7.

Following derivations in [28, 72, 87], after quantifying the surface current effect on voltage over the resonator, an equivalent circuit description of the particle's effect on the detection circuit will be found, which can then be used to understand the output signals of the detection system.

A high-quality parallel LC-resonator with resonance frequency $\tilde{\omega} = 1\big/\sqrt{L_p C_p}$, parallel inductance L_p, capacitance C_p, and residual parallel resistance $R_p = Q\omega L$ is connected to one trap electrode per relevant mode as shown in Fig. 2.7. The quantity Q is the quality factor of the resonator and is given by the ratio of $\tilde{\omega}$ to its resonance width $\Delta\tilde{\omega}$, in which its absolute impedance $|Z(\omega)|$ is at least half of $|Z(\tilde{\omega})|$. High values of Q signify a weak damping per oscillation[4].

The induced current $I_{\bar{p}}$ from the particle motion $r_\mu(t)$ of mode μ is given by

$$I_{\bar{p}} = \frac{q}{D_\mu}\dot{r}_\mu = \frac{q}{D_\mu}\omega_\mu r_\mu\,, \tag{2.18}$$

where the effective electrode distance D_μ is an experimental parameter proportional to the inner ring electrode diameter. In the motivating case of a particle oscillating inside an infinitely large plate capacitor, D_μ equals the distance between the plates. Since the electrode is connected in series to the resonator, the surface currents flow through the it. If $\tilde{\omega} = \omega_\mu$ for any mode μ, then $Z(\omega_\mu) = R_p$ and the current of the resonant mode maximizes the voltage drop and power dissipation over the resonator.

$$U_{\bar{p}} = Z(\omega_\mu)I_{\bar{p}} \xrightarrow{\omega_\mu\to\tilde{\omega}} R_p I_{\bar{p}} = R_p\frac{q\omega_\mu}{D_\mu}r_\mu \quad P_{\bar{p}} = U_{\bar{p}}I_{\bar{p}} \xrightarrow{\omega_\mu\to\tilde{\omega}} R_p I_{\bar{p}}^2 = R_p\frac{q^2\omega_\mu^2}{D_\mu^2}r_\mu^2 \tag{2.19}$$

The other modes are out of resonance with respect to the LC-resonator (off-resonator), where $|\tilde{\omega} - \omega_\mu| \gg \Delta\tilde{\omega}$, so $R_p \gg Z(\omega_\mu)$ and the respective voltage drops are negligable. The electrical quantities can now be related to the particle motion.

Assuming the particle behaves like an undriven oscillator with a damping coefficient γ_μ, its equations of motion are given by $\ddot{r}_\mu + 2\gamma_\mu\dot{r}_\mu + \omega_\mu^2 r = 0$. Taking the derivative of the total energy of the particle in its harmonic mode

$$P_{\bar{p}} = -\partial_t E_{\bar{p}} = \partial_t\big(\tfrac{1}{2}m\dot{r}_\mu^2 + \tfrac{1}{2}m\omega_\mu^2 r_\mu^2\big) = m\dot{r}_\mu\ddot{r}_\mu + m\omega_\mu^2 r_\mu\dot{r}_\mu = m\dot{r}_\mu(\ddot{r}_\mu + \omega_\mu^2 r_\mu) \tag{2.20}$$

shows that $-P_{\bar{p}}\big/m\dot{r}_\mu$ is equal to two of the terms in the particle's equation of motion. Inserting it into the equation of motion and substituting the alternative description of $P_{\bar{p}}$ from Eq. (2.19) yields

$$\frac{R_p q^2}{D_\mu^2}\dot{r}_\mu^2 = R_p I_{\bar{p}}^2 = P_{\bar{p}} = -m\dot{r}_\mu\ddot{r}_\mu - m\omega_\mu^2 r\dot{r}_\mu = 2m\gamma_\mu\dot{r}_\mu^2 \qquad \Longrightarrow \qquad \gamma_\mu = \frac{R_p q^2}{2mD_\mu^2}\,, \tag{2.21}$$

which allows rewriting the equation of motion without γ_μ and in terms of derivatives of $I_{\bar{p}}$ using $\dot{r}_\mu \propto I_{\bar{p}}$. The similarity to an ODE of a series RCL circuit then allows an equivalent circuit definition, shown in Fig. 2.8.

$$0 = \frac{mD_\mu^2}{q^2}\ddot{I}_{\bar{p}} + R_p\dot{I}_{\bar{p}} + \omega_\mu^2\frac{mD_\mu^2}{q^2}I_{\bar{p}} \overset{!}{=} L_{\bar{p}}\ddot{I}_{\bar{p}} + R_{\bar{p}}\dot{I}_{\bar{p}} + \frac{1}{C_{\bar{p}}}I_{\bar{p}} \tag{2.22}$$

The particle current flows through the resonator at its resonance frequency, where all current flows only through its parallel resistance R_p. Thus, R_p is part of the equivalent

[4]The envelope of a freely oscillating resonator with quality factor $Q \gg 1$ and period T will decay with a time constant $\tau \approx TQ/\pi$. This follows from the energy decay formulation of Q on page 42 of [88].

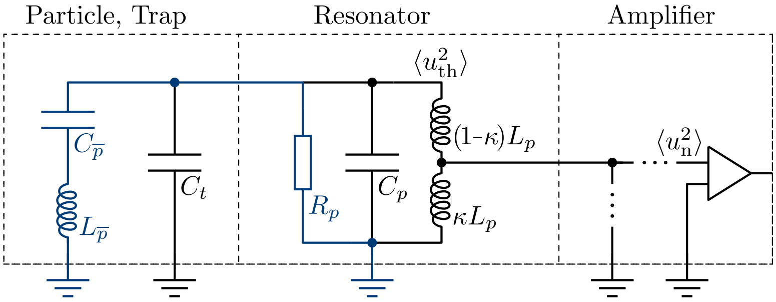

Figure 2.8: Circuit diagram for the axial particle detection setup in the precision trap including the particle and trap. The Equivalent circuit of the particle is highlighted in blue and overlaps the resonator circuit at its parallel resistance. All trap electrodes are DC biased via an RC circuit, so the detection electrode is grounded over a total capacitance C_t, which will not be considered further since it can be absorbed into the equivalent resonator components [86]. Since the electrode has an impedence to ground, its potential is contaminated by thermal Johnson-Nyquist noise $\langle u_{\mathrm{th}}^2 \rangle \propto k_{\mathrm{B}} T \, \mathrm{Re}(Z_p)$ [89], propagating to the amplification stage and combining with its approximately white input noise $\langle u_{\mathrm{n}}^2 \rangle$.

circuit of the particle shown in Fig. 2.8, explaining why $R_{\bar{p}} = R_p$. The series capacitance, inductance and pure particle impedance are given by

$$C_{\bar{p}} = \frac{1}{\omega_\mu^2} \frac{q^2}{m D_\mu^2} \qquad L_{\bar{p}} = \frac{m D_\mu^2}{q^2} \qquad Z_{\bar{p}} = i\sqrt{\frac{L_{\bar{p}}}{C_{\bar{p}}}} \left(\frac{\omega}{\omega_\mu} - \frac{\omega_\mu}{\omega} \right) , \tag{2.23}$$

while the total impedance and resistance of the resonator are given by

$$Z_p = \frac{1}{\frac{1}{R_p} + i\sqrt{\frac{C_p}{L_p}} \left(\frac{\omega}{\tilde{\omega}} - \frac{\tilde{\omega}}{\omega} \right)} \qquad \mathrm{Re}(Z_p) = \frac{|Z_p|^2}{R_p} = \frac{1}{R_p} \frac{1}{\frac{1}{R_p^2} + \frac{C_p}{L_p} \left(\frac{\omega}{\tilde{\omega}} - \frac{\tilde{\omega}}{\omega} \right)^2} . \tag{2.24}$$

Since the electrode is connected to the particle and resonator simultaneously, a parallel circuit of the two impedances above is created. Thus, the total impedance $Z_{\mathrm{tot}}(\omega)$ is small if the circuit is driven at the relevant mode frequency ω_μ, or at very small and large frequencies far away from $\tilde{\omega}$. If ω_μ and $\tilde{\omega}$ coincide, Z_{tot} increases sharply in a range approximately $\Delta\omega_\mu$ wide around ω_μ before converging to Z_p when moving further away from the combined resonance. The resulting $|Z_{\mathrm{tot}}|$ curve is proportional to the dip spectra shown in Fig. 2.13, which is explained in Section 2.2.2. A useful definition of $\Delta\omega_\mu$ to quantify the shape of Z_{tot} is the frequency span in which the particle shorts the resonator resistance to less than half of its maximum resistance R_p.

$$\begin{aligned} Z_{\mathrm{tot}} &= \frac{1}{\frac{1}{R_p} + i\left(\sqrt{\frac{C_p}{L_p}} \frac{\omega^2 - \tilde{\omega}^2}{\omega\tilde{\omega}} - \sqrt{\frac{C_{\bar{p}}}{L_{\bar{p}}}} \frac{\omega\omega_\mu}{\omega^2 - \omega_\mu^2} \right)} \\ \mathrm{Re}(Z_{\mathrm{tot}}) = \frac{|Z_{\mathrm{tot}}|^2}{R_p} &= \frac{1}{R_p} \frac{1}{\frac{1}{R_p^2} + \left(\sqrt{\frac{C_p}{L_p}} \frac{\omega^2 - \tilde{\omega}^2}{\omega\tilde{\omega}} - \sqrt{\frac{C_{\bar{p}}}{L_{\bar{p}}}} \frac{\omega\omega_\mu}{\omega^2 - \omega_\mu^2} \right)^2} \end{aligned} \tag{2.25}$$

In the limit of coinciding ω_μ and $\tilde{\omega}$, and $\Delta\omega_\mu \ll \Delta\tilde{\omega}$, the resonator can be approximated by its resistance $R_p = Z_p(\tilde{\omega})$ alone and Z_{tot} degenerates to the impedance of a parallel circuit of R_p and Z_p. Solving for $Z_{\text{tot}}(\omega) = \frac{1}{2}R_p$ to calculate $\Delta\omega_\mu$ yields four valid ω:

$$\omega_{1,2,3,4} = \pm\frac{R_p}{2L_{\bar{p}}} \pm \sqrt{\left(\frac{R_p}{2L_{\bar{p}}}\right)^2 + \frac{1}{C_{\bar{p}}L_{\bar{p}}}} = \frac{\omega_\mu}{2}\left(\pm\sqrt{\frac{C_{\bar{p}}}{L_{\bar{p}}}}R_p \pm \sqrt{\frac{C_{\bar{p}}}{L_{\bar{p}}}R_p^2 + 4}\right) \tag{2.26}$$

Two of the solutions correspond to negative frequencies. The second term is larger than the first, so the positive solutions $\omega_{1,2}$ are obtained using a positive second term. The difference of ω_1 and ω_2 then gives $\Delta\omega_\mu$. Since the simplified spectrum is asymmetric around ω_μ, it is not the average of ω_1 and ω_2, but their geometric mean because of the spectrum's symmetry in logarithmic frequency space.

$$\omega_\mu = e^{\frac{1}{2}\left(\ln\omega_1 + \ln\omega_2\right)} = \sqrt{\omega_1\omega_2} \qquad \Delta\omega_\mu = |\omega_1 - \omega_2| = \omega_\mu\sqrt{\frac{C_{\bar{p}}}{L_{\bar{p}}}}R_p \tag{2.27}$$

2.2.1 Peak Methods Using an Excited Particle

Driving a particle at ω_μ by applying a corresponding AC voltage to one of the electrodes breaking the motional symmetry will increase the particle's energy until it drifts out of resonance at very high energies due to the electromagnetic field imperfections of the trap. If the resonator is tuned to ω_μ, it is also excited by the drive, amplifying the drive's effect on the particle. After the excitation, the particle will drive the resonator even if the external drive is turned off, dissipating its energy into R_p. Thus, after the excitation drive, the electrode oscillation will first decay with the resonator energy decay time constant τ_p until the residual excitation from the particle increases the decay time to $\tau_{\bar{p}}$ of the equivalent particle circuit in Fig. 2.8. This bin-dependent particle decay behaviour is shown in Fig. 2.9. Using the fact that a resonator dissipates about $1/Q_\mu$ of its energy every $1/\tilde{\omega}$, the respective decay time τ_μ can be calculated in terms of the equivalent circuit quantities.

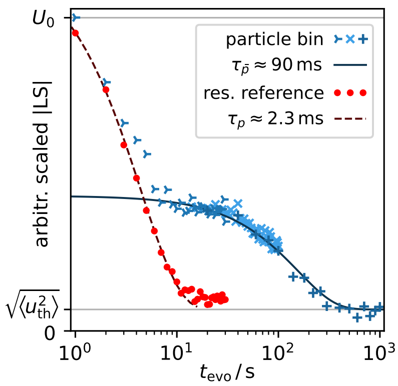

Figure 2.9: Both peak and reference resonator bin powers decay with increasing wait time after excitation for the BASE precision trap.

$$E_0 = \left(1 - \tfrac{1}{Q_\mu}\right)e^{\frac{1}{\omega_\mu\tau_\mu}}E_0 \quad\Longrightarrow\quad \tau_\mu = \frac{1}{\omega_\mu}\frac{1}{\ln\left(1 + \frac{1}{Q_\mu}\right)} \xrightarrow{Q_\mu\to\infty} \frac{Q_\mu}{\omega_\mu} = \frac{R_p}{\omega_\mu}\sqrt{\frac{C_p}{L_p}} \tag{2.28}$$

To measure only the particle signal, the acquisition should be delayed until the resonator oscillation has died down. After this point, the resonator is driven by the particle with current and voltage $\hat{I}, \hat{U} \propto \dot{r}_\mu \propto \sqrt{E_{\bar{p}}} \propto e^{-t/2\tau_{\bar{p}}}$, which corresponds to a time dependent power dissipation of $P \propto e^{-t/\tau_{\bar{p}}}$.

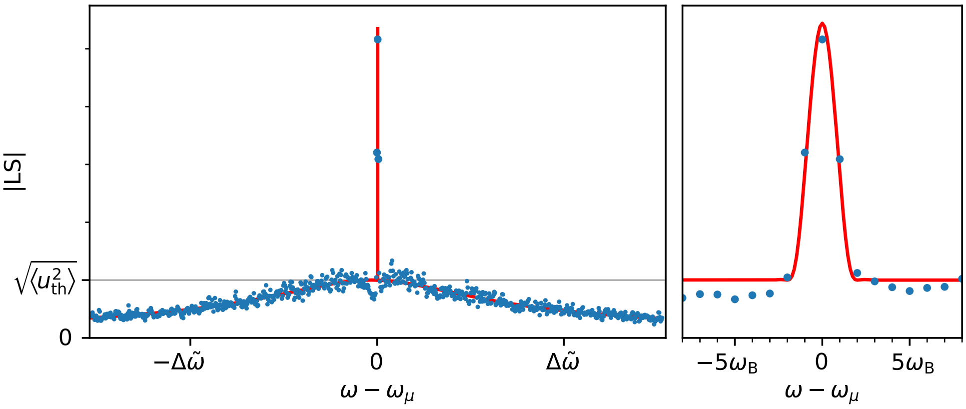

Figure 2.10: A representative peak spectrum, acquired in the BASE precision trap using a heavily attenuated continuous $\omega_+ + \omega_z$ drive to excite the particle's axial mode as described in Section 2.3.3. The particle signal is visible as a peak in the linear spectrum at the frequency bin containing ω_z. The increased linear spectrum of the two neighbouring bins is an effect of the broadened main lobe from applying a Hann window on the signal before calculating the DFT [90]. As the particle is moving slightly within the bin, the main lobe is wider than expected by the fit. As with dip spectra, a resonator background is visible around ω_z, amplifying the particle signal and creating a noise background limiting the peak SNR.

The frequency estimation uncertainty is inversely proportional to the peak SNR of $\mathrm{LS}_S \big/ \mathrm{LS}_N$, which can be optimized by the correct choice of acquisition time T. The particle voltage signal is assumed to be $U(t) = U_0 \cos(\omega_\mu t + \varphi_\mu)\, e^{-t/\tau}$ with an amplitude decay time constant $\tau := 2\tau_{\bar{p}}$. The data is acquired with a signal analyzer using an unwindowed discrete Fourier transform (DFT) with a sampling frequency f_S. With the above assumptions, the linear spectrum LS_S of the particle signal can be calculated.

$$\begin{aligned} \mathrm{LS}_S(\omega) &= \frac{1}{T}\left|\int_0^T U(t)\, e^{-i\omega t}\, \mathrm{d}t\right| = \frac{U_0}{T}\left|\int_0^T \cos(\omega_\mu t + \varphi_\mu)\, e^{-\frac{t}{\tau}} e^{-i\omega t}\, \mathrm{d}t\right| \qquad (2.29) \\ &= \frac{U_0}{T}\left|\frac{\xi(\omega_\mu T + \varphi_\mu) e^{-\frac{T}{\tau}} e^{-i\omega T} - \xi(\varphi_\mu)}{\omega_\mu^2 - \left(\omega - \frac{i}{\tau}\right)^2}\right| \qquad \xi(\varphi) := \omega_\mu \sin\varphi - i\left(\omega - \tfrac{i}{\tau}\right)\cos\varphi \end{aligned}$$

In a span of a few DFT bin widths ω_B around ω_μ, the resonator noise is approximately white, even if it is not tuned to ω_μ. This allows describing the resonator noise by a linear spectral density LSD_N, from which the corresponding linear spectrum for a given acquisition time can be obtained [90].

$$\mathrm{LS}_N(\omega) = \sqrt{\frac{\omega_B}{2\pi}}\, \mathrm{LSD}_N = \frac{1}{\sqrt{T}}\, \mathrm{LSD}_N \qquad (2.30)$$

Even with the effective exponential window from the decaying particle, the SNR is maximized at $\omega = \omega_\mu$, with the unnormalized Fourier transform $T\,\mathrm{LS}_S(\omega)$ converging to its maximum value. The SNR is dependent on φ_μ, but decreasingly so if $1 \ll \omega_\mu \tau, \omega_\mu T$, because the initial oscillation state loses its relevance as more oscillations occur before the particle signal is decayed and the acquisition stops. In that case, $\xi(\varphi) \to -i\omega_\mu e^{i\varphi}$ and the numerator in Eq. (2.29) simplifies, yielding an approximate SNR of

$$\mathrm{SNR}_\mathrm{peak} = \frac{\mathrm{LS}_S}{\mathrm{LS}_N} \approx \frac{U_0}{\mathrm{LSD}_N} \left| \frac{i\omega_\mu e^{i\varphi_\mu}}{\omega_\mu^2 - \left(\omega_\mu - \frac{i}{\tau}\right)^2} \right| \frac{1 - e^{-\frac{T}{\tau}}}{\sqrt{T}} \approx \frac{U_0}{2\,\mathrm{LSD}_N} \frac{\tau}{\sqrt{T}} \left(1 - e^{-\frac{T}{\tau}}\right). \tag{2.31}$$

The measured signal bin linear spectrum LS_S will partially scale with LSD_N according to Eq. (3.2), which becomes relevant if $\mathrm{LS}_S \lesssim \mathrm{LS}_N$. In those regimes, the inverse scaling of frequency uncertainty and SNR breaks down, too.

$$\partial_T \, \mathrm{SNR}_\mathrm{peak} = \frac{\tau}{\sqrt{T}} \left[\left(\frac{1}{\tau} + \frac{1}{2T} \right) e^{-\frac{T}{\tau}} - \frac{1}{2T} \right] \stackrel{!}{=} 0$$

$$\Longrightarrow \; T = \left[-\tfrac{1}{2} - W_{-1}\!\left(-\tfrac{1}{2} e^{-\frac{1}{2}} \right) \right] \tau \approx 1.2564\,\tau$$

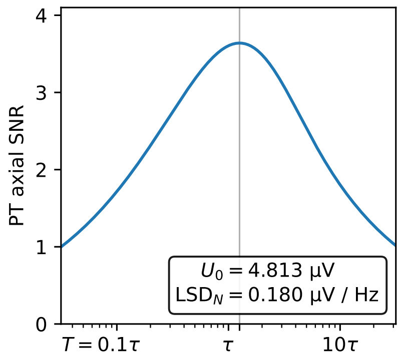

Figure 2.11: Theoretical scaling prediction of the PT axial peak with T for an initial axial amplitude of $\hat{z} = 1\,\mathrm{mm}$. With $\tau = 2 \cdot 90\,\mathrm{ms}$ from Fig. 2.9, $T \approx 226\,\mathrm{ms}$ is the optimal acquisition time.

The tuned SNR scaling[5] depending on T is shown in Fig. 2.11. Due to the resonant amplification of the particle signal on the resonator, the peak SNR stays constant when detuning the resonator for a fixed T, as $U_0 \propto |Z_p| \propto \mathrm{LSD}_N$. However, the optimal T and thus SNR increases when detuning, as $T_\mathrm{opt} \propto \tau \propto \gamma_\mu^{-1} \propto \mathrm{Re}(Z_p)^{-1} \propto \mathrm{LSD}_N^{-2}$.

C_8 Frequency Shifts

Besides the SNR effects, the peak frequency precision is limited by the particle frequency drift during the acquisition time, which is caused by two different effects: electrode voltage instabilities and systematic frequency shifts from the particle energy decay. The electrode voltages are very stable if not intentionally changed shortly beforehand, while the energy decay shifts are the most prominent. Figure 2.10 is the average of multiple excitations with different particle energies, where ω_μ is shifted more or less, broadening the peak shape. The fitted Hann window response is thus too narrow to perfectly fit the peak shape. In general, the higher-order electromagnetic field contributions shift ω_μ away from its harmonic value $\omega_{\mu,0}$. As the particle dissipates its energy into the resonator, its amplitude shrinks and the frequency shift decreases, causing the peak to drift back to $\omega_{\mu,0}$. In an optimized Penning trap, C_4 and C_6 are suppressed and odd components should be negligible due to the trap symmetry, leaving C_8 as the first electrostatic inhomogeneity. To be able to investigate the effect of frequency shifts on the axial peak shape, it is assumed that magnetic effects can be ignored in favour of C_8. The undampened axial motion can then be described as

$$\ddot{z} = -\frac{q}{m} V_R \left(2C_2 z + 8C_8 z^7 \right) = -\omega_{z,0}^2 \left(z + \epsilon \frac{z^7}{Z^6} \right) \qquad \dot{z}(0) = 0 \qquad z(0) = Z \tag{2.32}$$

[5] W_{-1} is the lower branch of the Lambert W function.

with the free axial frequency $\omega_{z,0} = 2\frac{q}{m}V_R C_2$ and a small unitless perturbation term $\epsilon := 4Z^6 C_8 / C_2$ proportional to C_8. Following the Linstedt renormalization procedure outlined in [91], the fundamental frequency ω_z and solution $z(t)$ to the equation of motion can be found by a perturbation ansatz

$$\omega_z = \omega_{z,0} + \epsilon\omega_{z,1} + \epsilon^2\omega_{z,2} + \ldots \qquad z(t) = z_0(t) + \epsilon z_1(t) + \epsilon^2 z_2(t) + \ldots\,, \tag{2.33}$$

together with the initial conditions $\dot{z}_0(0) = 0$, $z_0(0) = Z$, and $\dot{z}_k(0) = 0$, $z_k(0) = 0$. After rearranging the frequency perturbation term, both can be inserted into the undampened axial motion equation (2.32) to obtain

$$\left(\ddot{z}_0 + \epsilon\ddot{z}_1 + \ldots\right) + \left[\left(z_0 + \epsilon z_1 + \ldots\right) + \frac{\epsilon}{Z^6}\left(z_0 + \epsilon z_1 + \ldots\right)^7\right]\left(\omega_z - \epsilon\omega_{z,1} - \ldots\right)^2 = 0\,, \tag{2.34}$$

from which the effect of the perturbation can be calculated to any order by iteratively extracting terms with higher powers k of ϵ and solving the resulting equations for ω_k, z_k with the previously obtained solutions of $\omega_{<k}$, $z_{<k}$. The two lowest-order equations

$$\epsilon^0: \qquad \ddot{z}_0 + \omega_z^2 z_0 = 0 \qquad \dot{z}_0(0) = 0 \qquad z_0(0) = Z \tag{2.35}$$

$$\epsilon^1: \qquad \ddot{z}_1 + \omega_z^2 z_1 = 2\omega_z\omega_{z,1}z_0 - \omega_z^2 z_0^7 / Z^6 \qquad \dot{z}_1(0) = 0 \qquad z_1(0) = 0 \tag{2.36}$$

describe the unperturbed case $z_0(t) = Z\cos(\omega_z t)$ and the main perturbation effect. $z_0^7 / Z^7 = \frac{35}{64}\cos(\omega_z t) + \frac{21}{64}\cos(3\omega_z t) + \frac{7}{64}\cos(5\omega_z t) + \frac{1}{64}\cos(7\omega_z t)$ follows from trigonometric identities and can be inserted into Eq. (2.36) to yield

$$\ddot{z}_1 + \omega_z^2 z_1 = \underbrace{\left(2Z\omega_z\omega_{z,1} - \frac{35}{64}Z\omega_z^2\right)}_{\text{secular term} \overset{!}{=} 0}\cos(\omega_z t) - \sum_{k=1}^{3} c_k Z\cos\big((2k+1)\omega_z t\big)\,, \tag{2.37}$$

where the secular term must vanish since the oscillation with ω_z is already contained in $z_0(t)$. Rearranging for $\omega_{z,1}$ finally allows solving for the frequency shift $\delta\omega_z \approx \epsilon\omega_{z,1}$.

$$\delta\omega_z \approx \epsilon\omega_{z,1} = 4\frac{Z^6 C_8}{C_2}\frac{35}{128}\omega_z \approx \frac{35}{32}\frac{Z^6 C_8}{C_2}\omega_{z,0} \propto Z^6 \tag{2.38}$$

Solving Eq. (2.36) with the remaining terms would give the full perturbed movement of the axial mode, where the C_8 perturbation will introduce odd harmonics of ω_z op to the seventh order.

Summarizing some of the above results, the particle oscillates inside the Penning trap with an axial energy E_z proportional to the square of both the axial amplitude $\hat{z}$ and the induced peak voltage U on the electrode. Since the particle is coupled to the axial resonator, its energy E_z, and thus $\hat{z}^2$, U^2, and $\sqrt[3]{\delta\omega_z}$ decay as $e^{-t/\tau_{\bar{p}}}$. Thus, the particle moves through frequency space as it loses its energy, creating not just a singular LS peak bin, but a whole spectrum. Estimating the shape of the spectra is useful since it shows if the maximum SNR is expected for a still systematically shifted particle, or for an already converged one. Naively, the resulting LS_S spectrum could be calculated by

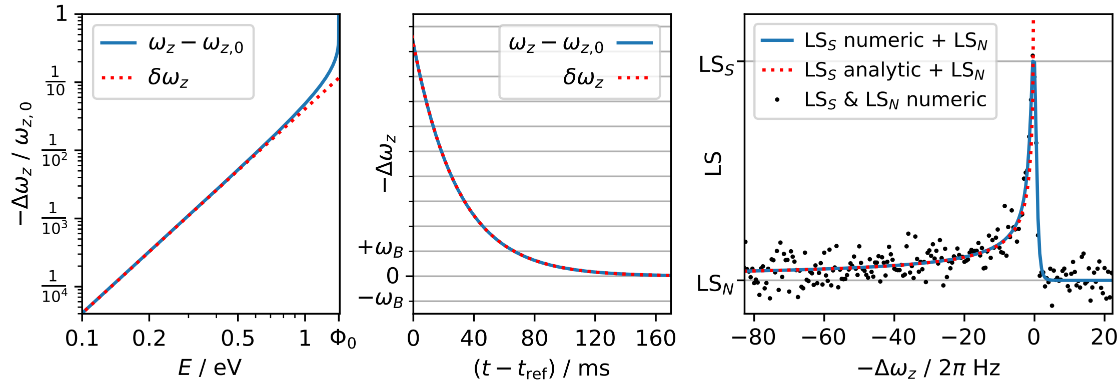

Figure 2.12: Expected C_8 effects on the axial peak frequency in the BASE precision trap, with estimated trap parameters from prior measurements. The left plot shows the region of validity for the calculated first-order frequency perturbation $\delta\omega_z$ from Eq. (2.38). It is a good approximation in the range of detectable frequency shifts $\Delta\omega_z \ll \omega_{z,0}$. At higher energies, the pure C_8 shift increases until the particle escapes the model trap at $E = \Phi_0$. The second plot shows how ω_z converges back exponentially to $\omega_{z,0}$ in relation to 4 Hz bin-widths. The time spent per bin is very short compared to $\tau_{\bar{p}}$, except for the last few bins. Exciting the particle to higher energies does not affect how it behaves in the last bins, it only starts the particle with a larger shift. The last plot summarizes the LS_S analysis done. The approximation Eq. (2.40) in red is overlaid onto numerical DFT calculations of a simulated decaying particle in the trap. One of the numerical calculations includes the noise floor in the time domain, while LS_N is added to the others using Eq. (3.2).

deriving the total time $\tilde{T}$ that $\omega_z = \omega_{z,0} + \delta\omega_z$ spends in each bin, together with the axial energy E_z at that time.

$$\tilde{T}(\Delta\omega) = \frac{\tau_{\bar{p}}}{3} \ln\left(1 + \frac{\omega_B}{\Delta\omega}\right) \qquad\qquad E_{z,0}(\Delta\omega) \propto \sqrt[3]{\Delta\omega + \omega_B} \tag{2.39}$$

If the axial energy does not change much inside one bin, the product $\tilde{T}\sqrt{E}$ would seem to approximate LS_S. However, as ω_z changes, so does the initial phase that the DFT would determine for the oscillation, should its frequency stay constant. Consequently, the measured LS_S is overestimated as the frequency contributions inside the bin partially destructively interfere due to their phase differences. Instead of calculating how the phase depends on ω_z, it will subsequently assumed to be random and uncorrelated for all values of ω_z. This approximates the phase variation inside the bin and allows treating the drifting signal as noise. The superposition of all frequency contributions inside one bin can then be calculated as their root sum square instead of their average.

$$\mathrm{LS}_S(\Delta\omega) \propto \sqrt{\int_t^{t+\tilde{T}} \sqrt{E(t)}^2 \mathrm{d}t} \propto \sqrt{\left(\sqrt[3]{\Delta\omega + \omega_B} - \sqrt[3]{\Delta\omega}\right)\tau_{\bar{p}}} \tag{2.40}$$

LS_S is maximized at $\Delta\omega = 0$, as shown in Fig. 2.12, so there is no reason to excite the particle to energies which shift it out of its equilibrium DFT bin. Decreasing T to $\tilde{T}$ for a specific shifted bin at $\Delta\omega$ will theoretically increase the SNR inside the bin, but drastically decrease the frequency precision as given by ω_{B}, as $\omega_{\mathrm{B}} \propto 1/T$.

Direct Excitation and Initial Energy Scatter

A mathematical description of the excitation process makes it possible to quantify the state distribution of the particle after excitation, and the subsequent effect on the recorded peak spectrum. This description is given here, starting from the particle's known equation of motion with a sinusoidal driving term generating a maximum electric field $\mathcal{E}_{\text{drive}}$ at the trap center. The derivation will focus on the axial mode ($\mu = z$).

$$\ddot{r}_\mu + 2\gamma_\mu \dot{r}_\mu + \omega_\mu^2 r_\mu = \frac{1}{m} F_{\text{drive}}(t) = \frac{q}{m} \mathcal{E}_{\text{drive}} \cos(\omega_\mu t) \tag{2.41}$$

Focussing on the axial mode ($\mu = z$), The resulting equation of motion is that of a dampened harmonic oscillator driven at its resonance frequency, of which the solutions with and without damping are known [92], where $\tilde{A}$ and $\tilde{\varphi}$ are free parameters.

$$z(t) = \begin{cases} \dfrac{q}{m} \dfrac{\mathcal{E}_{\text{drive}}}{2\omega_z} t \sin(\omega_z t) + \tilde{A} \cos(\omega_z t + \tilde{\varphi}) & \gamma_z = 0 \\ \dfrac{q}{m} \dfrac{\mathcal{E}_{\text{drive}}}{2\omega_z} \dfrac{1}{\gamma_z} \sin(\omega_z t) + \tilde{A} \cos(\omega_z t + \tilde{\varphi})\, e^{-\gamma_z t} & \gamma_z > 0 \end{cases} \tag{2.42}$$

In both cases, the undriven general solutions of the homogeneous ODE diminish in comparison to the particular solution for sufficient excitation times. For the measurements done at BASE and in this thesis, the excitation times are normally much shorter than the decay time[6], where $z(t)$ is well approximated by the undampened solution.

Since the particle's axial energy E_z is constant and the sum of its potential $E_{\text{pot}} = \frac{m}{2}\omega_z^2 z^2$ and kinetic component $E_{\text{kin}} = \frac{m}{2}\dot{z}^2$, a variable $\alpha \coloneqq E_{\text{kin}} \big/ E_z$ can be defined as the fraction of the particles energy currently stored in its motion. The initial conditions can then be specified up to changes in sign by the axial energy and its current division.

$$\dot{z}(0) = \pm\sqrt{\tfrac{2E_{z,0}}{m}\alpha} \qquad\qquad z(0) = \pm\sqrt{\tfrac{1}{\omega_z^2}\tfrac{2E_{z,0}}{m}(1-\alpha)} \tag{2.43}$$

Solving Eq. (2.42) for those initial conditions yields the axial position

$$z(t) = \frac{q}{m} \frac{\mathcal{E}_{\text{drive}}}{2\omega_z} t \sin(\omega_z t) + \sqrt{\frac{2E_{z,0}}{m\omega_z^2}} \cos\big(\omega_z t + \varphi(\alpha)\big) \tag{2.44}$$

with the α-dependent initial phase $\varphi(\alpha)$ distributed uniformly for a particle with fixed $E_{z,0}$ and unknown phase[7]. Equation (2.44) can then be used to calculate the total axial energy $E_z(t)$ via $\dot{z}(t)$, $E_{\text{kin}}(t)$, $E_{\text{pot}}(t)$, and the substitution $A \coloneqq q\mathcal{E}_{\text{drive}} \big/ \sqrt{8m}$.

$$\begin{aligned} E_z(t) = {} & \Big[A^2 t^2 - 2At\sqrt{E_{z,0}} \sin\big(\varphi(\alpha)\big) + E_{z,0}\Big] \\ & + \frac{A}{\omega_z} \sin(\omega_z t) \left[\frac{A}{\omega_z} \sin(\omega_z t) - 2\sqrt{E_{z,0}} \sin\big(\omega_z t + \varphi(\alpha)\big) + 2At \cos(\omega_z t)\right] \end{aligned} \tag{2.45}$$

[6] Rough excitation and decay timescales are given by $0.1\,\text{ms} \lesssim T_{\text{exc}} \lesssim 10\,\text{ms}$ and $100\,\text{ms} \lesssim \frac{1}{\gamma_z} \lesssim \infty$.

[7] $\mathcal{P}_\alpha(x) = 1 \big/ \pi\sqrt{1-x}\sqrt{x}$ with a domain $[0, 1]$ and $\mathcal{P}_\varphi(x) = \frac{1}{2\pi} = \text{const.}$ with a domain $[0, 2\pi]$.

Of the six terms on the right side of Eq. (2.45), one scales with t^2, two with t, and three are constant. During a peak measurement, the particle's excited energy $E_{z,*}$ is much greater than its initial energy $E_{z,0}$, so $At \gg \sqrt{E_{z,0}}$ and $t\omega_z \gg 1$ and the terms growing with time become dominant. Thus, the energy equation can be used to roughly approximate the distribution of $E_z(t)$ directly.

$$E_{z,*} \approx A^2t^2 \qquad \sigma_{E_{z,*}} \approx 2At\sqrt{E_{z,0}} \cdot \sigma(-\sin\varphi) = \sqrt{2E_{z,*}E_{z,0}} \tag{2.46}$$

Temporarily moving to the phase space $\xi = \sqrt{m}\left(\begin{smallmatrix}\dot z\\ \omega z\end{smallmatrix}\right) \mathrel{\hat=} \sqrt{m}\,(\dot z + i\omega z)$ of the driven oscillation with energy $E_z = |\xi|^2$, the particle's motion satisfies

$$\xi(t) = At\begin{pmatrix}\cos(\omega_z t) + \frac{1}{t\omega_z}\sin(\omega_z t)\\ \sin(\omega_z t)\end{pmatrix} + \sqrt{E_{z,0}}\begin{pmatrix}-\sin(\omega_z t+\varphi)\\ \cos(\omega_z t+\varphi)\end{pmatrix}. \tag{2.47}$$

Since $t\omega_z \gg 1$, the extra term in the $\dot z$-component can be neglected to simplify the equation of motion to

$$\xi(t) = \left(At + i\sqrt{E_{z,0}}\,e^{i\varphi}\right)e^{i\omega_z t} = \left(At + \xi_0\right)e^{i\omega_z t}. \tag{2.48}$$

If the particle is thermalized before its excitation (see Section 2.2.2), its initial energy $E_{z,0}$ is Boltzmann-distributed. Due to φ being uniformly random, ξ_0 is symmetrically normally distributed in two dimensions. The properties of ξ_0 are given by

$$\langle\xi_0\rangle = 0 \qquad \sigma_{\mathrm{Re}(\xi_0)} = \sigma_{\mathrm{Im}(\xi_0)} = \sqrt{\tfrac{1}{2}E_{z,0}} \qquad \sigma_{\xi_0} = \sqrt{E_{z,0}}\,. \tag{2.49}$$

$\xi(t)$ is thus exactly the kind of Rice-distributed random variable investigated later in Section 3.1.2, with $\Lambda = At$, $\Lambda_v \mathrel{\hat=} \Lambda\hat e_1$, $\xi_0 \mathrel{\hat=} \vec\xi_{\mathrm{N}}$, and $\sigma = \sqrt{E_{z,0}/2}$. Using Eq. (3.3) together with the first moments[8] of ξ_0 and Λ_v allows determining $E_{z,*}$ and $\sigma_{E_{z,*}}$.

$$\begin{aligned}
\langle E_{z,*}\rangle &= \langle\xi^2\rangle = \Lambda^2 + 2\langle\Lambda_v\xi_0\rangle + \langle\xi_0^2\rangle &&= \Lambda^2 + 2\sigma^2\\
\langle E_{z,*}\rangle^2 &= \langle\xi^2\rangle^2 = (\Lambda^2+2\sigma^2)(\Lambda^2+2\sigma^2) &&= \Lambda^4 + 4\Lambda^2\sigma^2 + 4\sigma^4\\
\langle E_{z,*}^2\rangle &= \langle\xi^4\rangle = \Lambda^4 + 2\Lambda^2\langle\xi_0^2\rangle + 4\langle(\Lambda_v\xi_0)^2\rangle + \langle\xi_0^4\rangle &&= \Lambda^4 + 8\Lambda^2\sigma^2 + 8\sigma^4\\
\langle E_{z,*}^2\rangle - \langle E_{z,*}\rangle^2 &= \Lambda^4 + 8\Lambda^2\sigma^2 + 8\sigma^4 - \Lambda^4 - 4\Lambda^2\sigma^2 - 4\sigma^4 = 4\sigma^2\left(\Lambda^2+\sigma^2\right)
\end{aligned}$$

$$\langle E_{z,*}\rangle = A^2t^2 + E_{z,0} \tag{2.50}$$

$$\begin{aligned}
\sigma_{E_{z,*}} &= \sqrt{\langle E_{z,*}^2\rangle - \langle E_{z,*}\rangle^2} = \sqrt{2A^2t^2E_{z,0} + E_{z,0}^2} = \sqrt{2E_{z,*}E_{z,0} - E_{z,0}^2} \qquad (2.51)\\
&\xrightarrow{E_{z,0}/E_{z,*}\to 0} \sqrt{2E_{z,*}E_{z,0}}\left(1 - \frac{1}{4}\frac{E_{z,0}}{E_{z,*}}\right)
\end{aligned}$$

The result disagrees slightly with Borchert [80], who investigates the expected value and standard deviation of the total energy $E_{z,*}$ in terms of the energy increase A^2t^2 instead of $E_{z,*}$ itself. The analytic results agree, but the approximation given in [80] breaks down as $A^2t^2 \to 0$.

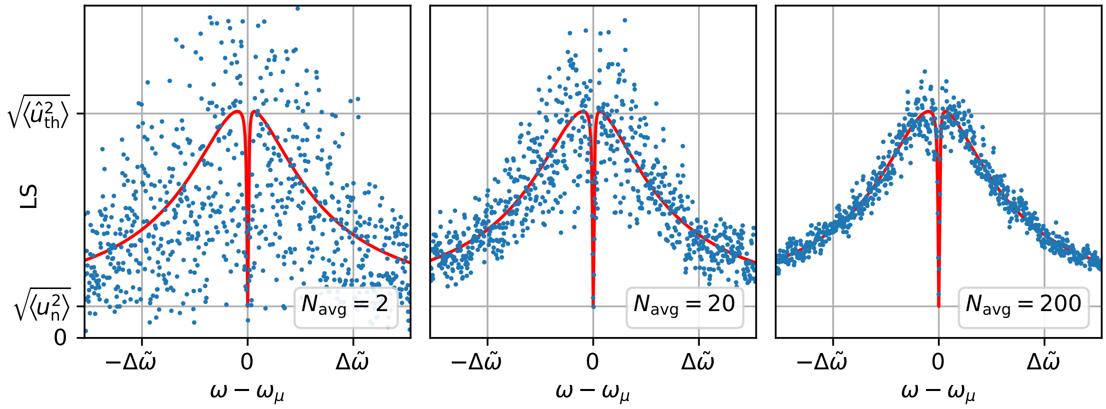

Figure 2.13: Representative dip spectra, acquired in the BASE precision trap. The amplified Johnson-Nyquist noise generated by the frequency-dependent detection electrode resistance $\mathrm{Re}(Z_{\mathrm{tot}})$ is detected by the signal analyzer, and creates a rayleigh-distributed linear spectrum with expected value $\langle \mathrm{LS} \rangle \propto \sqrt{\mathrm{Re}(Z_{\mathrm{tot}})}$ on the resonator. Since the standard deviation σ_{LS} of LS is on the order of $\langle \mathrm{LS} \rangle$, the dip frequency determination from a single acquired spectrum is both unreliable and numerically unstable. Averaging multiple spectra decreases σ_{LS} and increases the reliability of the fit as the average converges to $\langle \mathrm{LS} \rangle$.

2.2.2 Dip Methods Using a Cold Particle

A cold particle inside the trap will not actively drive the resonator. Instead, its main effect is the effective series LC circuit parallel to the resonator from the electrode voltage to ground as described in Eqs. (2.23) and (2.24). Such a parallel circuit will decrease the impedance Z_{tot} from the electrode to ground, with the strongest reduction at the resonance frequency ω_μ of the particle. For the axial mode, the reduction in impedance is normally very strong but contained to a small region of the resonator's resonance curve since $\Delta\omega_z \ll \Delta\tilde{\omega}$, creating a dip in $|Z_{\mathrm{tot}}|$. With $N \lesssim 10^4$ particles in the trap, $1/L_{\bar{p}}$ and $C_{\bar{p}}$, and thus $\Delta\omega_z$ are increased proportionally to N [72]. In general, $\delta\omega_z \propto R_p \propto 1/\delta\tilde{\omega}$, so an improvement in the resonator's quality is necessarily accompanied by a wider dip. Varying κ in the detection circuit has similar effects due to the dependence of Z_{tot} on κ. As $\kappa \to 1$, the amplifier's input resistance limits the effective R_p, maximizing $\hat{Z}_p$ while broadening the dip. Conversely, as $\kappa \to 0$, the effective R_p is maximized at the cost of a greater voltage division of the tapped signal [86].

In any floating node connected to ground by a resistor R, the thermal agitation of the electrons generates an approximately white voltage noise with a flat spectral density

$$\langle \mathrm{PSD} \rangle = 4k_{\mathrm{B}}TR \qquad \Longrightarrow \qquad \langle \mathrm{LSD} \rangle = \frac{\sqrt{\pi}}{2}\sqrt{\langle \mathrm{PSD} \rangle} = \sqrt{\pi k_{\mathrm{B}}TR} = \frac{\langle \mathrm{LS} \rangle}{\sqrt{\frac{\omega_B}{2\pi}\mathcal{N}_{\mathrm{w}}}} \tag{2.52}$$

over a wide range of frequencies $\omega \ll \frac{k_{\mathrm{B}}}{\hbar}T$, where T is the electrical temperature of the resonator and $\mathcal{N}_{\mathrm{w}}$ is the normalized equivalent noise bandwidth of the window used to

[8] The moments are given by $\langle \Lambda_v \xi_0 \rangle = 0$, $\langle \xi_0^2 \rangle = 2\sigma^2$, $\langle (\Lambda_v \xi_0)^2 \rangle = \Lambda^2\sigma^2$, $\langle \Lambda_v \xi_0^3 \rangle = 0$, and $\langle \xi_0^4 \rangle = 8\sigma^4$.

acquire the linear spectrum [89, 93]. This so-called Johnson-Nyquist noise generalizes to complex and frequency-dependent impedances Z as well, still scaling with the resistant part $\mathrm{Re}(Z)$. For all of the circuits considered here, $R_p \,\mathrm{Re}(Z) = |Z|^2$, so $\langle \mathrm{LSD}_N \rangle \propto |Z|$, which was already used in Section 2.2.1 to compare the off-resonator peak level with the resonator background.

Qualitatively, the particle acts as an energy storage. Driven by an excited resonator, it absorbs its electrical energy around ω_z into the kinetic and potential energy of its axial mode. The effect decreases as the driving frequency moves away from resonance, and more of the resonator's energy is absorbed and converted to heat via its parallel resistance R_p. If the resonator is in thermal equilibrium, it will only drive the particle via its Johnson-Nyquits noise with a uniformly randomly distributed phase over time. The particle thus absorbs no net energy above its thermal equilibrium, as the energy absorbed and emitted by the constructive and destructive drive phases cancel each other out. As a result, ignoring background noise effects described below, the detected noise spectrum is that of the free resonator, suppressed around ω_z.

By exploiting the Johnson-Nyquist noise as a proxy for the resonator's impedance, a trapped particle can be detected by the noise at ω_z that is *not* generated by the resonator. The detected linear spectral density is the amplified combination of the thermal noise $\langle \mathrm{LSD}_{N,\bar{p}}(\kappa)\rangle\kappa$ from Z_{tot} and the background $\langle \mathrm{LSD}_{\mathrm{Bg}}\rangle$ from the amplifier's input noise shown in Fig. 2.8. For a fixed κ, $\langle \mathrm{LSD}_{N,\bar{p}}\rangle$ is only dependent on ω and

$$\langle \mathrm{LSD}_{\mathrm{tot}}\rangle \propto \sqrt{\langle \mathrm{LSD}_{N,\bar{p}}\rangle^2\kappa^2 + \langle \mathrm{LSD}_{\mathrm{Bg}}\rangle^2} = \sqrt{\pi\kappa^2 k_{\mathrm{B}} T \,\mathrm{Re}(Z_{\mathrm{tot}}) + \langle \mathrm{LSD}_{\mathrm{Bg}}\rangle^2}\,, \tag{2.53}$$

with such fits for some dip measurements shown in Fig. 2.13. At ω_z, the particle shorts the resistance of the electrode to ground to $Z_{\mathrm{tot}} \approx 0$, so the remaining noise density is given by $\mathrm{LSD}_{\mathrm{tot}} \approx \mathrm{LSD}_{\mathrm{Bg}}$. If $\Delta\omega_z \ll \Delta\tilde{\omega}$, then $\max_\omega \mathrm{Re}(Z_{\mathrm{tot}})$ still approximates $\max_\omega \mathrm{Re}(Z_{\mathrm{p}}) = R_p$, so the dip SNR turns out to be

$$\mathrm{SNR}_{\mathrm{dip}} = \frac{\max_\omega \langle \mathrm{LSD}_{\mathrm{tot}}(\omega)\rangle}{\langle \mathrm{LSD}_{\mathrm{tot}}(\omega_z)\rangle} = \frac{\sqrt{\pi\kappa^2 k_{\mathrm{B}} T R_p + \langle \mathrm{LSD}_{\mathrm{Bg}}\rangle^2}}{\langle \mathrm{LSD}_{\mathrm{Bg}}\rangle}\,. \tag{2.54}$$

Fitting Dip Spectra

While $\langle \mathrm{LSD}_{\mathrm{tot}}\rangle$ can be described according to Eq. (2.53), a single measurement of $\mathrm{LSD}_{\mathrm{tot}}$ is Rayleigh-distributed and scatters around the mean with $\sigma_{\mathrm{LSD}_{\mathrm{tot}}} = \sqrt{4/\pi - 1}\langle \mathrm{LSD}_{\mathrm{tot}}\rangle$. As shown in Fig. 2.13, the dip feature is not visible in any single spectrum due to the scatter, and only becomes clearer when averaging multiple independently acquired spectra. Averaging overlapping spectra as done in [94] increases the convergence, but the standard error of the resulting $\langle \mathrm{LSD}_{\mathrm{tot}}\rangle$ is more difficult to calculate. Fitting the linear spectrum is also complicated, as $\sigma_{\mathrm{LSD}_{\mathrm{tot}}}$ depends on ω. Transforming the Rayleigh distribution to log-LSD space and normalizing it results in a function

$$\mathcal{P}_{\mathrm{lin}}\big(x; \mu = \langle \mathrm{LSD}_{\mathrm{tot}}\rangle\big) = \frac{\pi}{2}\frac{x}{\mu^2} e^{-\frac{\pi}{4}\frac{x^2}{\mu^2}} \qquad \mathcal{P}_{\mathrm{log}}\big(x; \mu = \langle \mathrm{LSD}_{\mathrm{tot}}\rangle\big) = e^{x-\mu} e^{-\frac{\pi}{4}e^{2(x-\mu)}}$$

$$\mu_{\mathrm{lin}} = \mu, \quad \sigma_{\mathrm{lin}} = \mu\sqrt{\tfrac{4}{\pi} - 1} \qquad \mu_{\mathrm{log}} \approx \mu - \tfrac{1}{2}(\gamma - \ln \pi), \quad \sigma_{\mathrm{log}} = \tfrac{\pi^2}{8}$$

that is solely dependent on the difference $x - \mu$, so the integration over $\mathbb{R}$ performed in the calculation of the logarithmic standard deviation $\sigma_{\log}$ removes the dependence on μ, meaning $\sigma_{\log}$ is constant over the whole logarithmic spectrum. This is the reason why most dip spectra in the literature are illustrated and fitted in logarithmic space. By including $\mathcal{P}_{\log}$ into the error function to be minimized, fitting can be improved to such an extent that single spectra taken in the precision trap are directly fitable.

To improve precision compared to the hard-to-fit single spectrum, a noise measurement over a timespan T is normally split into N segments, which are individually converted into linear spectra before being averaged together in frequency space. Overlapping the segments allows increasing their number without decreasing their length, improving the averaged $\sigma_{\mathrm{LSD_{tot}}}$ further. This is how noise spectra are obtained at BASE. Alternatively, the full single spectrum can be calculated, and the neighbouring frequency bins can be averaged together, resulting in an average spectrum with equal bin width, but an improved drop-off rate.

Thermalization of the Resonator-Coupled Particle

A highly excited particle coupled to the resonator will dissipate its energy into it, causing the respective mode to decay exponentially down to some equilibrium energy, where the decay stops. Instead, the coupled mode will continuously exchange energy with the resonator, sampling a Boltzmann distribution with equivalent background temperature T_{Bg}. The transition from the known excited state to an increasingly broadly distributed equilibrium state has to be described using the methods of statistical physics, as is done for example in Fleck [87]. In analogy to a driven dampened oscillator, the particle will become increasingly decoherent from its initial state as it interacts further with the resonator, behaving roughly as $\mu(T_0 + t) \sim e^{-\lambda_{\mathrm{dec}} t}\mu(T_0) + (1 - e^{-\lambda_{\mathrm{dec}} t})\tilde{\mu}$ with the equilibrium state distribution $\tilde{\mu}$ and decoherence time $1 \big/ \lambda_{\mathrm{dec}}$.

By treating the particle's velocity $|\vec{v}_\mu|$ as a variable subject to a random walk under the resonator-particle interaction, the statistical treatment leads to the equipartition theorem in the equilibrium, with an expected energy $\frac{1}{2}k_{\mathrm{B}}T_{\mathrm{Bg}}$ stored in its motion, and consequently its potential as well due to the virial theorem. While the origin of T_{Bg} is not explained here, it is influenced by the thermodynamic temperature of the resonator but can be changed by deliberately applying a phase-shifted copy of the resonator's Johnson-Nyquist noise onto the electrode potential to either increase or decrease its strength [95, 96]. The application of this noise is called a feedback drive. As an example, the BASE precision trap axial resonator is about 4 K, since it is connected to a liquid-helium cryostat. However, without feedback, T_{Bg} is around 10 K and can be decreased to about 1 K, or increased to more than 60 K with negative or positive feedback.

Negatively feedbacking into unmeasured modes minimizes their systematic error into the measurements of other modes. For the phase sensitive measurements implemented in this thesis and described in Section 4.2, negative feedback also allows preparing the particle in a lower energy initial state than otherwise possible, decreasing the uncertainties propagating into the measured frequency.

2.3 Mode Coupling of ω_+ and ω_z

Utilizing an oscillating quadrupolar field which breaks the cylindrical symmetry of the Penning trap allows coupling and energy transfer between the motional modes of the particle, and is necessary for the cyclotron phase measurement scheme used in this thesis. The use of mode coupling between the modified cyclotron and axial mode is motivated in Section 4.2, whereas the following paragraphs describe the theoretical foundation of the coupling behaviour, following derivations of Sturm et al. [82] and Cornell et al. [97] for coupling along the lower and upper sidebands, which respectively give rise to the ”Pulse and Phase” (PnP) and ”Pulse and Amplify” (PnA) schemes for phase detection [80]. Brown and Gabrielse [53] provide a more formal derivation of mode coupling on the lower sideband in the context of mode thermalization[9], and a quantum mechanical description of mode coupling is given by Kretzschmar [98].

In a typical Penning trap, one of the correction electrodes is segmented to break cylindrical symmetry and allow the excitation and detection of radial modes. As usual, $\hat{e}_z$ specifies the axial direction, the trap centre is located at $\vec{r} = 0$, and the electrode is separated along the $\hat{e}_y\hat{e}_z$ plane. At BASE, one of the two segments is capacitively coupled to the resonator circuit and connected via a high-impedance resistor to the other, ”hot” segment, connected to both the DC bias and RF radial drive lines. Applying an RF drive $U(t) = U_0 \cos(\tilde{\omega}t)$ to the hot segment shifts its voltage relative to the other segment, superimposing a dipole contribution along $\hat{e}_x$ onto the Penning potential. The resulting potential Φ_R is symmetric in y and thus dependent only on y^2, but since all other electrode voltages stay constant relative to only the ”cold” segment, the reflection symmetry in x is broken, allowing perturbative potential contributions linear in x.

$$\begin{aligned}\Phi_\mathrm{R}(\vec{r},t) &= \Phi(\vec{r}) + \Big(\varepsilon_x x + \varepsilon_z z + \varepsilon_{x^2} x^2 + \varepsilon_{y^2} y^2 + \varepsilon_{z^2} z^2 + \varepsilon_{xz} xz + \mathcal{O}\big(r^3\big)\Big)\cos(\tilde{\omega}t) \\ &\approx \big(z^2 - \tfrac{1}{2}x^2 - \tfrac{1}{2}y^2\big)\,\Phi_2 + \varepsilon_{xz} xz \cdot \cos(\tilde{\omega}t) \qquad\qquad [\Phi_2] = [\varepsilon_{xz}] = \mathrm{V/m^2}\end{aligned}$$

For small drive voltages, $\varepsilon_{xz} \ll \Phi_2$, so the drive field only slowly affects the particle's motion. Only terms dependent on the radial and axial coordinate will couple the axial with a radial mode by linking their equations of motion. The lowest order such term is the quadrupolar potential $\varepsilon_{xz} xz \cdot \cos(\tilde{\omega}t)$. Higher order coupling terms are increasingly irrelevant at small distances from the trap centre if not designed for, and couple at different drive frequencies [99], so they are subsequently discarded.

Referencing Section 2.1 and specifically Eq. (2.10), the particle's radial equation of motion in an unperturbed Penning trap can be written as a superposition of a fast pure modified cyclotron ω_+ and slow magnetron ω_- motion. Since the external force of the drive power is assumed to be small against both the electric and magnetic components of the Lorentz force, the mode separation holds and both radial motions can be treated independently.

[9] Since the energy spectrum of the magnetron mode is inverted, the effects of lower and upper sideband coupling are switched, and upper sideband coupling is used for any thermalization involving the magnetron mode.

Gyrokinetically, the time-averaged drive potential at the gyrocenter $\vec{r}_-$ remains equivalent to averaging over N modified cyclotron orbits if the drive and modified cyclotron frequencies are detuned such that $\omega_+ / \tilde{\omega} \ll N \ll \omega_+ / \omega_-$. The averaging must be performed on timescales smaller than the magnetron period, explaining the latter inequality. Thus, if the particle is driven at frequencies above or comparable to ω_+, the gyrokinetic potential is shifted only by a constant $f(r_+)$ dependent on the modified cyclotron mode radius r_+, leading to an electric field identical to the undriven case and thus undriven magnetron motion.

$$\begin{aligned}\left\langle \Phi_\mathrm{R}\big(\vec{r}_- + \vec{r}_+(t)\big)\right\rangle &= \frac{\omega_+}{2\pi N}\oint_0^{\frac{2\pi N}{\omega_+}} \Phi_\mathrm{R}\big(\vec{r}_- + r_+\hat{e}_x\cos(\omega_+ t) + r_+\hat{e}_y\sin(\omega_+ t)\big)\,\mathrm{d}t \\ &= \left(z^2 - \frac{x_-^2}{2} - \frac{y_-^2}{2} - \frac{r_+^2}{2}\right)\Phi_2 + \underbrace{\left(\frac{\tilde{\omega}^2}{\tilde{\omega}^2-\omega_+^2}r_+ + x_-\right)\operatorname{sinc}\left(2\pi N\frac{\tilde{\omega}}{\omega_+}\right)}_{\longrightarrow\, 0 \text{ if } \omega_+ \ll N\tilde{\omega}}\varepsilon_{xz}z \\ &\approx \left\langle \Phi_\mathrm{R}(\vec{r}_-)\right\rangle + f(r_+) = \Phi(\vec{r}_-) + f(r_+)\end{aligned} \tag{2.55}$$

At modified cyclotron motion timescales, $\vec{r}_-$ is constant, the magnetron motion decouples from the cyclotron motion and is expressed as a constant drift velocity in the total radial motion. With the decoupled magnetron mode, the particle's equation of motion can be stated in axial and modified cyclotron mode coordinates x_+, y_+, z.

$$\partial_t^2\begin{pmatrix}x_+\\y_+\\z\end{pmatrix} + \omega_+\begin{pmatrix}0&1&0\\-1&0&0\\0&0&0\end{pmatrix}\partial_t\begin{pmatrix}x_+\\y_+\\z\end{pmatrix} + \omega_z^2\frac{\varepsilon_{xz}}{2\Phi_2}\begin{pmatrix}0&0&\cos\tilde{\omega}t\\0&0&0\\\cos\tilde{\omega}t&0&\frac{2\Phi_2}{\varepsilon_{xz}}\end{pmatrix}\begin{pmatrix}x_+\\y_+\\z\end{pmatrix} = 0 \tag{2.56}$$

At lower drive frequencies $\tilde{\omega} \lesssim \omega_-$, the averaging suppression of the neglected term decreases ($\operatorname{sinc}\tau \to 1$ as $\tau \to 0$). The drive potential average over the cyclotron motion converges to the potential in the gyrocenter, now constant at modified cyclotron motion timescales, and the magnetron motion is driven while the modified cyclotron motion perceives a constant drive potential in time[10]. This regime is not investigated further, since only the coupling of the modified cyclotron and axial mode is relevant for the modified cyclotron phase detection.

Continuing from Eq. (2.56), the differential equation of y_+ can be integrated and substituted into the equation for x_+ to eliminate the dependence on y_+ and reduce the system of differential equations to that of 2 coupled one-dimensional harmonic oscillators[11].

$$\partial_t^2\begin{pmatrix}x_+\\z\end{pmatrix} + \begin{pmatrix}\omega_+^2 & \frac{q}{m}\varepsilon_{xz}\cos\tilde{\omega}t\\ \frac{q}{m}\varepsilon_{xz}\cos\tilde{\omega}t & \omega_z^2\end{pmatrix}\begin{pmatrix}x_+\\z\end{pmatrix} = 0 \tag{2.57}$$

With $\varepsilon_{xz} \ll \Phi_2$, the coupling terms $\frac{q}{m}\varepsilon_{xz}\cos\tilde{\omega}t$ are small against the diagonal elements and the modes are weakly coupled. Their behaviour is thus perturbed from the uncoupled

[10] In general, the quadrupolar potential being time-invariant does not suffice to prevent mode coupling.

[11] Subsequent students are invited use $c_+ = x_+ + iy_+$, $c_z = z + i\dot{z}/\omega_z$ to treat the motion of the particle, in which the behaviour of the modes is inherently a pure complex oscillation. The uncoupled equations of motion are given by $\dot{c}_x = -i\omega_+ c_x$, $\dot{c}_z = -i\omega_z c_z$ at the cost of a less beautiful coupling term of $\operatorname{Re}\ddot{c}_{x/z} = \frac{q}{m}\varepsilon_{xz}\cos(\tilde{\omega}t)\operatorname{Re}c_{z/x}$.

case, with slight frequency variation and slowly changing amplitude. The perturbations motivate the ansatz $z(t) \coloneqq \eta_z A_z(t) \cos(\omega_z t)$ and $x_+(t) \coloneqq \eta_x A_x(t) \cos(\omega_+ t)$ with explicit normalized complex motional amplitudes $A_i(t)$ and a normalization factor $\eta_i \in \mathbb{R}^+$ scaling the uncoupled particle motion. Substituting the ansatz into Eq. (2.57) allows writing a system of ordinary differential equations for the amplitudes directly.

Both $A_i(t)$ should vary slowly with negligible second derivative. They are fundamentally approximative since switching on the coupling drive causes only a finite discontinuity in the driving force, so the particle position and thus $A_i(t)$ should be once differentiable everywhere. However, since the drive can be switched off at any time, forcing both $A_i(t)$ to be constant afterwards, they would need to be constant everywhere to stay differentiable independent of drive switching. Still, the approximation is sufficient in most relevant cases, as can be seen in Fig. 2.14.

$$\dot{A}_x = \frac{\eta_z}{\eta_x} \frac{q}{m} \frac{\varepsilon_{xz}}{2\omega_+} \frac{\cos(\tilde{\omega} t)\cos(\omega_z t)}{\sin(\omega_+ t)} A_z \qquad \dot{A}_z = \frac{\eta_x}{\eta_z} \frac{q}{m} \frac{\varepsilon_{xz}}{2\omega_z} \frac{\cos(\tilde{\omega} t)\cos(\omega_+ t)}{\sin(\omega_z t)} A_x \tag{2.58}$$

Both η_z and η_x are constant, and η_z/η_x may be chosen such that the initial factors above are equal, simplifying the system of ODEs by requiring $(\eta_z/\eta_x)^2 = \omega_+/\omega_z$. Inserting this term into Eq. (2.58) allows the simplification of both equations using a shared scaling factor frequency[12] $\Omega \propto \varepsilon_{xz} \propto \sqrt{P_{\text{drive}}}$, resulting in a normalized description.

$$\dot{A}_x = \frac{\Omega}{2} \frac{\cos(\tilde{\omega} t)\cos(\omega_z t)}{\sin(\omega_+ t)} A_z \qquad \dot{A}_z = \frac{\Omega}{2} \frac{\cos(\tilde{\omega} t)\cos(\omega_+ t)}{\sin(\omega_z t)} A_x \qquad \Omega \coloneqq \frac{q}{m} \frac{\varepsilon_{xz}}{\sqrt{\omega_+ \omega_z}} \tag{2.59}$$

Since the equations for both A_i are equivalent using the above definition for η_z/η_x, their range of values will be too. Recalling the substitutions for z and x_+ and inserting both η_i, one finds that the amplitude of the axial mode is larger than the radial mode by a factor of $\sqrt{\omega_+/\omega_z}$. Thus, $\hat{z} \sim \sqrt{\omega_+/\omega_z}\, \hat{x}$.

Equation (2.58) will subsequently be solved by reformulating it for the complex domain and retaining only one $e^{i\omega t}$ component for all three trigonometric terms, equivalent to substitutions $\cos\tilde{\omega}t \mapsto e^{\pm_1 i\tilde{\omega}t}$, $z(t) \mapsto \sqrt{\omega_+}\, Z(t)\, e^{\pm_2 i\omega_z t}$, and $x_+(t) \mapsto \sqrt{\omega_z}\, X(t)\, e^{\pm_3 i\omega_+ t}$ in Eq. (2.60). This allows combining all oscillations into one, with the total frequency being the signed sum of all component frequencies. The eight sign combinations of $\pm_1, \pm_2, \pm_3$ will result in 4 different absolute frequencies.

$$\dot{A}_x = \mp_3 \frac{\Omega}{2i} e^{i(\pm_1\tilde{\omega} \pm_2 \omega_z \mp_3 \omega_+)t} A_z \qquad \dot{A}_z = \mp_2 \frac{\Omega}{2i} e^{i(\pm_1\tilde{\omega} \mp_2 \omega_z \pm_3 \omega_+)t} A_z \tag{2.60}$$

If one of them is much smaller than the others, then all but the lowest absolute total frequency terms $\pm\delta$ are discarded by use of the rotating wave approximation [100], since the high-frequency effects will cancel across timescales of δ^{-1}. Of the remaining frequencies $\pm\delta$, only one is chosen per coupling term, and they must have opposite signs. Keeping single frequencies of equal sign, or both frequencies in both terms will lead to incorrect results. The mathematical justification for the preceding steps is unclear to me, but they match derivations in [53, 80, 97] and they do successfully approximate the behaviour of Eq. (2.57) as seen in Fig. 2.14 and Fig. 2.16.

[12] Cornell et al. [97] use $V_{[97]} = i\Omega$ for their derivations, but still erroneously define it as $V_{[97]} \coloneqq i\Omega/2$.

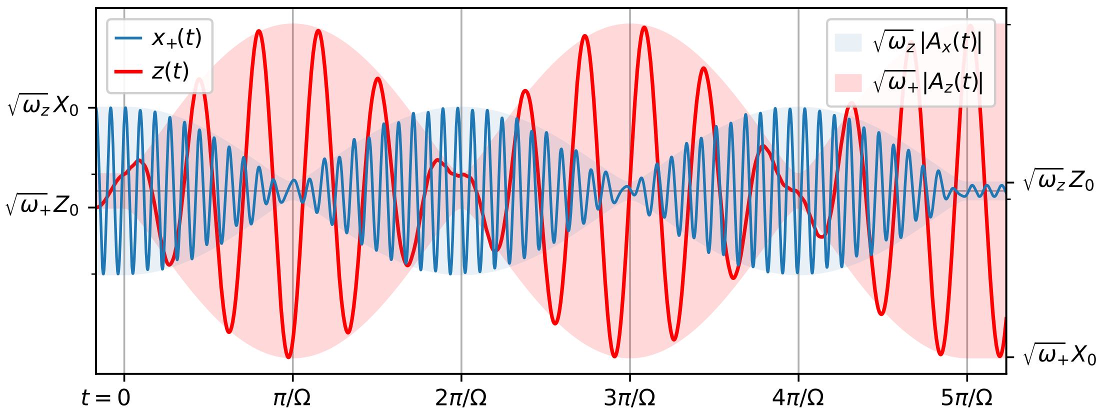

Figure 2.14: Time evolution of the radial x_+ and axial z modes, and rescaled motional amplitude envelopes A_x and A_z. Between $t = 0$ and $t = 5\pi/\Omega$, the modes are coupled via a tuned drive on the lower sideband frequency $\omega_+ - \omega_+$. During the coupling, the initial mode energy quanta evolve according to Eq. (2.64), being fully swapped in after the coupling. For illustrative purposes, the frequencies are rescaled to $8\Omega = 1.4\omega_z = 0.35\omega_+$ such that the mode behaviour is visible on both oscillation and Rabi timescales.

2.3.1 Pulse and Phase (PnP) coupling: $\tilde{\omega} \coloneqq \omega_+ - \omega_z + \delta$

The particle described by Eq. (2.60) is assumed to be imperfectly driven at the lower sideband frequency $\tilde{\omega} = \omega_+ - \omega_z + \delta$, with a small frequency detuning $|\delta| \ll \omega_z, \omega_+$. Therefore, δ fulfils the conditions for the minimum total frequency required by the rotating wave approximation. After selecting the remaining oscillating coupling terms by the above procedure, the system of ODEs is separable, and the resulting homogeneous ODE can be solved analytically by an $A_x(t) \propto e^{i\varpi_x t}$, $A_z(t) \propto e^{i\varpi_z t}$ ansatz to obtain the eigenfrequencies of the homogeneous solutions.

$$\left.\begin{aligned} \dot{A}_x &= i\tfrac{\Omega}{2}e^{i\delta t}A_z \\ \dot{A}_z &= i\tfrac{\Omega}{2}e^{-i\delta t}A_x \end{aligned}\right\} \implies \left\{\begin{aligned} 0 &= \ddot{A}_x - i\delta\dot{A}_x + \tfrac{\Omega^2}{4}A_x \\ 0 &= \ddot{A}_z + i\delta\dot{A}_z + \tfrac{\Omega^2}{4}A_z \end{aligned}\right\} \implies \begin{cases} 0 = \varpi_x^2 - \delta\varpi_x - \frac{\Omega^2}{4} \\ 0 = \varpi_z^2 + \delta\varpi_z - \frac{\Omega^2}{4} \end{cases} \tag{2.61}$$

$$\begin{aligned} \varpi_x &= \frac{1}{2}\Big(+\delta \pm \sqrt{\Omega^2+\delta^2}\Big) & \varpi_z &= \frac{1}{2}\Big(-\delta \pm \sqrt{\Omega^2+\delta^2}\Big) & \Omega' &\coloneqq \sqrt{\Omega^2+\delta^2} \\ &= \frac{1}{2}\big(+\delta \pm \Omega'\big) & &= \frac{1}{2}\big(-\delta \pm \Omega'\big) & & \end{aligned} \tag{2.62}$$

If the coupling drive $\tilde{\omega} = \omega_+ - \omega_z + \delta$ is detuned by $\delta \ll \Omega$, the two ϖ_i frequency branches interfere to produce a beat[13], coupling the motional amplitudes at half the Rabi frequency Ω'. When the drive is tuned, the frequency branches degenerate and the modes couple at half the resonant Rabi frequency $\Omega \leq \Omega'$. The cause of the scaling by one half is that the Rabi frequency describes the power transfer between the two modes, which happens at twice the amplitude coupling frequency. These coupling frequencies reoccur in the solution of Eq. (2.61) with given initial conditions of $A_x(0) = X_0$ and $A_z(0) = Z_0$,

[13] $\cos\big(\frac{1}{2}(\pm\delta+\Omega')t\big) + \cos\big(\frac{1}{2}(\pm\delta-\Omega')t\big) = 2\cos\big(\pm\frac{\delta}{2}t\big)\cos\big(\pm\frac{\Omega'}{2}t\big) \approx 2\cos\big(\pm\frac{\Omega'}{2}t\big)$ for $\delta \ll \Omega, t^{-1}$.

and converge to Ω in the simple limit of a correctly tuned drive. Alternatively, the initial conditions can also be specified by using $A'_x(0) = -\frac{\Omega}{2i} Z_0$ or $A'_z(0) = \frac{\Omega}{2i} X_0$.

$$A_x(t) = \Big(X_0 \cos\big(\tfrac{\Omega'}{2}t\big) - i\Big(\frac{\delta}{\Omega'}X_0 - \frac{\Omega}{\Omega'}Z_0\Big)\sin\big(\tfrac{\Omega'}{2}t\big)\Big)\, e^{i\frac{\delta}{2}t} \xrightarrow{\delta\to 0} X_0\cos\big(\tfrac{\Omega}{2}t\big) + iZ_0\sin\big(\tfrac{\Omega}{2}t\big)$$

$$A_z(t) = \Big(Z_0 \cos\big(\tfrac{\Omega'}{2}t\big) + i\Big(\frac{\delta}{\Omega'}Z_0 + \frac{\Omega}{\Omega'}X_0\Big)\sin\big(\tfrac{\Omega'}{2}t\big)\Big)\, e^{-i\frac{\delta}{2}t} \xrightarrow{\delta\to 0} Z_0\cos\big(\tfrac{\Omega}{2}t\big) + iX_0\sin\big(\tfrac{\Omega}{2}t\big)$$

The beat envelope frequency $\delta/2$ only affects the phase of both A_i, while the absolute value is fully determined by the carrier frequency $\Omega'/2$. Starting with all energy in the radial mode so $Z_0 = 0$ causes energy to be transferred from the radial into the axial mode until $T = \pi/\Omega'$, when the axial mode reaches its maximum amplitude $\hat{A}_z = \frac{\Omega}{\Omega'}X_0$, after which the process reverses. Thus, $\hat{A}_z \propto 1/\Omega'$ relative to changes in δ and is maximized using a tuned drive for a time-span of $T = \pi/\Omega$ so the most energy is transferred from the radial into the axial mode. Such a sequence is called a π-pulse, because $\pi = \Omega/T$. When sweeping over the detuning and coupling time, the increase in coupling frequency causes a distinct chevron-like amplitude pattern [101] used in qubit characterization.

Most importantly concerning the implementation of the phase-sensitive frequency measurements performed in this thesis, if the initial energy of the axial mode is negligible, the phase $\angle X_0$ of the radial mode is also imprinted onto the axial mode $\angle A_z(\pi/\Omega)$ after a π-pulse.

$$\angle x_+(0) - \angle z(\pi/\Omega) = \text{const.} \tag{2.63}$$

Since the radial energy transferred into the axial mode is $X_0 \sin\big(\frac{\tau}{2}\big)$ for a pulse of length τ/Ω', the phase imprinting is indeed successful for a wide range of possible pulse durations so long as $Z_0 \ll X_0 \sin\big(\frac{\tau}{2}\big)$. Phase imprinting is possible even with a small drive detuning if the pulse length is referenced against Ω'. However, the constant in phase difference depends on pulse length and drive detuning, so any differential measurements using Eq. (2.63) require them to be consistent.

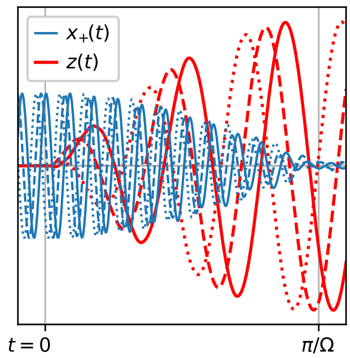

Figure 2.15: Phase transfer during a π-pulse for different initial $\angle x_+(0)$ causing equally shifted $\angle z(\pi/\Omega)$.

Adding the squares of the normalized amplitudes and simplifying by using the definition of Ω', it can be shown that $|A_x|^2 + |A_z|^2 =: A^2$ is constant. This, together with the amplitude $\hat{x}_+ = \sqrt{\omega_z}\, A_x$, $\hat{z} = \sqrt{\omega_+}\, A_z$ and mode energy formulas $E_+ = \frac{m}{2}\omega_+^2\hat{x}_+^2$, $E_z = \frac{m}{2}\omega_z^2\hat{z}^2$ can be used to show that the total particle energy varies during mode coupling, while the total number $N_+ + N_z$ of energy quanta $E_i = \hbar\omega_i N_i$ stays constant.

$$E_+ + E_z = \frac{m}{2}\big(\omega_+^2\hat{x}_+^2 + \omega_z^2\hat{z}^2\big) = \frac{m}{2}\omega_+\omega_z\big(\omega_+ A_x^2 + \omega_z A_z^2\big) \tag{2.64}$$

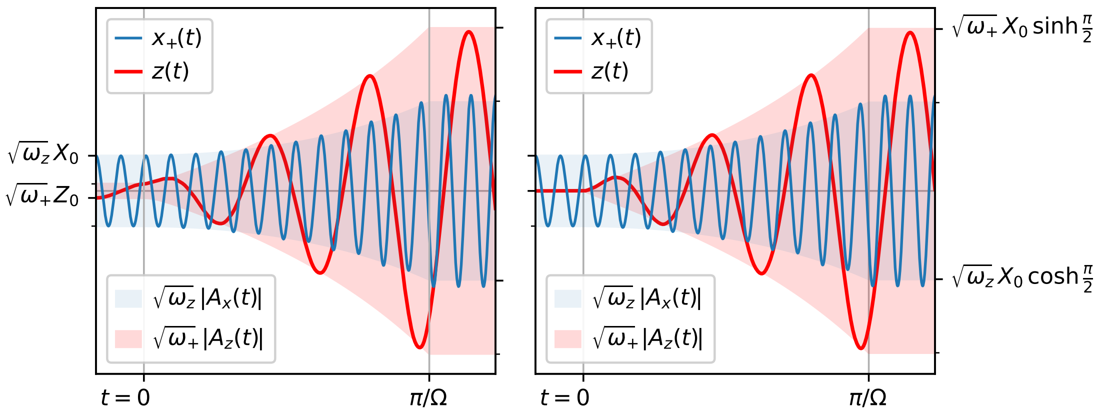

Figure 2.16: Time evolution of the radial x_+ and axial z modes, and rescaled motional amplitude envelopes A_x and A_z. Between $t = 0$ and $t = \pi/\Omega$, the modes are coupled via a tuned drive on the upper sideband frequency $\omega_+ + \omega_+$; with and without residual energy in the axial mode. During the coupling, the initial mode energy quanta evolve according to Eq. (2.69), increased by the same amount after the coupling. Again, $8\Omega = 1.4\omega_z = 0.35\omega_+$.

$$N_+ + N_z = \tfrac{E_+}{\hbar\omega_+} + \tfrac{E_z}{\hbar\omega_z} = \tfrac{m}{2\hbar}\big(\omega_+\hat{x}_+^2 + \omega_z\hat{z}^2\big) = \tfrac{m}{2\hbar}\omega_+\omega_z\big(A_x^2 + A_z^2\big) = \tfrac{m}{2\hbar}\omega_+\omega_z A^2 \qquad (2.65)$$

Quantum-mechanically, the coupling drive emits $\hbar(\omega_+ - \omega_z)$ quanta, which are absorbed or duplicated in a quadrupole interaction by incrementing either N_z or N_+, and decrementing the other. This mimics absorption and stimulated emission in excited atoms.

2.3.2 Pulse and Amplify coupling: $\tilde{\omega} \coloneqq \omega_+ + \omega_z + \delta$

In analogue to the derivation of the PnP coupling equations, the particle is driven at $\tilde{\omega} = \omega_+ + \omega_z + \delta$ with $|\delta| \ll \omega_z, \omega_+$. Again, terms with the lowest absolute frequency δ can be selected from Eq. (2.60) so the resulting system of ODEs is separable, and the resulting homogeneous ODE can be solved analytically by an $A_x(t) \propto e^{i\varpi_x t}$, $A_z(t) \propto e^{i\varpi_z t}$ ansatz to obtain the eigenfrequencies of the homogeneous solutions.

$$\left.\begin{matrix} \dot{A}_x = -i\frac{\Omega}{2}e^{i\delta t}A_z \\ \dot{A}_z = i\frac{\Omega}{2}e^{-i\delta t}A_x \end{matrix}\right\} \implies \left\{\begin{matrix} 0 = \ddot{A}_x - i\delta\dot{A}_x - \frac{\Omega^2}{4}A_x \\ 0 = \ddot{A}_z + i\delta\dot{A}_z - \frac{\Omega^2}{4}A_z \end{matrix}\right\} \implies \left\{\begin{matrix} 0 = \varpi_x^2 - \delta\varpi_x + \frac{\Omega^2}{4} \\ 0 = \varpi_z^2 + \delta\varpi_z + \frac{\Omega^2}{4} \end{matrix}\right. \qquad (2.66)$$

$$\begin{aligned} \varpi_x &= \frac{1}{2}\Big(+\delta \pm i\sqrt{\Omega^2 - \delta^2}\Big) & \varpi_z &= \frac{1}{2}\Big(-\delta \pm i\sqrt{\Omega^2 - \delta^2}\Big) & \Omega'' &\coloneqq \sqrt{\Omega^2 - \delta^2} \\ &= \frac{1}{2}\big(+\delta \pm i\Omega''\big) & &= \frac{1}{2}\big(-\delta \pm i\Omega''\big) \end{aligned} \qquad (2.67)$$

In contrast to coupling on the lower sideband, the solution of the system of ODEs with initial condition $A_x(0) = X_0$ and $A_z(0) = Z_0$ grows exponentially with time instead of oscillating. For the separated ODEs, the corresponding initial conditions are $A_x'(0) = \frac{\Omega}{2i}Z_0$ or $A_z'(0) = -\frac{\Omega}{2i}X_0$. This is the result of the imaginary component $\pm i\Omega''$ in the eigenfrequencies, which also specifies the growth rate of both A_i. Since

$|A_i| \propto |e^{i\varpi_i t}| = \exp(\mp\Omega''/2)$, the $\frac{1}{2}(\pm\delta - \Omega'')$ eigenfrequency will dominate the other, exponentially shrinking solution after $t \gtrsim 1/\Omega''$. In the limiting case of a tuned drive $\delta = 0$, both eigenfrequencies degenerate again and the absolute amplitude evolution becomes purely exponential.

$$A_x(t) = \Big(X_0 \cosh\big(\tfrac{\Omega''}{2}t\big) - i\big(\tfrac{\delta}{\Omega''}X_0 + \tfrac{\Omega}{\Omega''}Z_0\big)\sinh\big(\tfrac{\Omega''}{2}t\big)\Big)\, e^{i\frac{\delta}{2}t} \xrightarrow{\delta\to 0} X_0\cosh\big(\tfrac{\Omega}{2}t\big) - iZ_0\sinh\big(\tfrac{\Omega}{2}t\big)$$
$$A_z(t) = \Big(Z_0 \cosh\big(\tfrac{\Omega''}{2}t\big) + i\big(\tfrac{\delta}{\Omega''}Z_0 + \tfrac{\Omega}{\Omega''}X_0\big)\sinh\big(\tfrac{\Omega''}{2}t\big)\Big)\, e^{-i\frac{\delta}{2}t} \xrightarrow{\delta\to 0} Z_0\cosh\big(\tfrac{\Omega}{2}t\big) + iX_0\sinh\big(\tfrac{\Omega}{2}t\big)$$

Besides sign changes and the substitution from trigonometric to hyperbolic functions, the PnA amplitude evolution is equivalent to PnP. Thus, the absolute value changes over time are still fully determined by Ω'', while δ only affects the angle. Coupling for a time span of $T = \pi/\Omega'$ without initial axial energy increases the radial amplitude to $x_+(T) = \cosh\frac{\pi}{2}\, x_+(0)$ while the axial amplitude reaches $z(T) = \sqrt{\omega_+/\omega_z}\,\sinh\frac{\pi}{2}\, x_+(0)$.

The initial phase of the radial mode is also imprinted into the axial mode, and is robust against different detunings and drive durations as long as they are constant. Notably, changes of the initial radial phase $\angle X_0$ result in opposite changes to the axial phase $\angle A_z(\tau/\Omega)$ where τ is fixed.

$$\angle x_+(0) + \angle z(\tau/\Omega) = \text{const.} \tag{2.68}$$

But since the driven modes envelopes are strictly increasing, there is no need for specific π-type pulses anymore. The phase will stay imprinted independently of the coupling time, which for PnA will mostly be determined by higher-order behaviour of the system, trap potential depth and other experimental parameters. Imprinting is successful as long as $Z_0 \ll \tanh\big(\frac{\tau}{2}\big)X_0$.

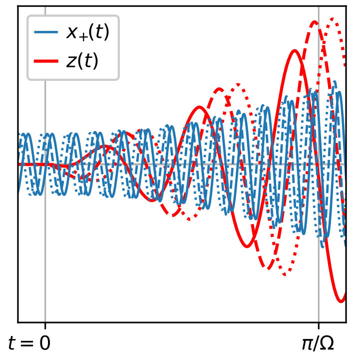

Figure 2.17: PnA phase transfer for different initial $\angle x_+(0)$ and resulting inversely shifted angles $\angle z(\pi/\Omega)$.

Quantum-mechanically, the coupling drive emits $\hbar(\omega_+ + \omega_z)$ quanta, which are absorbed or duplicated in a quadrupole interaction by lifting and lowering both N_z and N_+ by one. Thus, neither the total particle energy, nor the total number $N_+ + N_z$ of energy quanta $E_i = \hbar\omega_i N_i$ stays constant. However, since both quantum numbers are changed in tandem, their difference should be constant. Subtracting the squares of the normalized amplitudes and simplifying by using the definition of Ω'', it can be shown that $|A_x|^2 - |A_z|^2 =: A^2$ is constant. Reusing the amplitude $\hat{x}_+ = \sqrt{\omega_z}\,A_x$, $\hat{z} = \sqrt{\omega_+}\,A_z$ and mode energy formulas $E_+ = \frac{m}{2}\omega_+^2\hat{x}_+^2$, $E_z = \frac{m}{2}\omega_z^2\hat{z}^2$, this implies the conservation of $N_+ - N_z$.

$$N_+ - N_z = \frac{E_+}{\hbar\omega_+} - \frac{E_z}{\hbar\omega_z} = \frac{m}{2\hbar}\big(\omega_+\hat{x}_+^2 - \omega_z\hat{z}^2\big) = \frac{m}{2\hbar}\omega_+\omega_z\big(A_x^2 - A_z^2\big) = \frac{m}{2\hbar}\omega_+\omega_z A^2 \tag{2.69}$$

2.3.3 Mode Thermalization through Sideband Coupling

If an axially excited particle is thermally coupled to a cold axial detection resonator, then they will exchange energy quanta, exponentially cooling the axial mode $E_z(t) = E_{z,0}e^{-t/\tau_E}$ as shown in Eq. (2.21) with an energy decay time of $\tau_E \coloneqq 1/2\gamma_z$ until it thermalizes at the resonator temperature T_{Bg}. The expected axial quantum number N_z can then be determined from the resonator temperature via $k_{\mathrm{B}}T_{\mathrm{Bg}} = \langle E_z\rangle = \hbar\omega_z\langle N_z\rangle$.

If the axial mode is coupled on the lower sideband to the radial mode and resonator simultaneously, even with a detuned drive, then energy is continuously transferred between the two modes while the axial mode dissipates its energy into the resonator. After some time $t \gtrsim \tau_E, 1/\Omega'$, an equilibrium in resonator and axial mode energies, and axial and radial quantum numbers is reached, relating the temperature of the cooled modes.

$$T_z = \frac{1}{k_{\mathrm{B}}}\langle E_z\rangle = \frac{\hbar\omega_z}{k_{\mathrm{B}}}\langle N_z\rangle \overset{!}{=} T_{\mathrm{Bg}} \overset{!}{=} \frac{\hbar\omega_z}{k_{\mathrm{B}}}\langle N_+\rangle = \frac{1}{k_{\mathrm{B}}}\frac{\omega_+}{\omega_z}\langle E_+\rangle = \frac{\omega_+}{\omega_z}T_+ \tag{2.70}$$

The temperature ratio between two sideband cooled modes is thus equal to their frequency ratio, and the resonator-coupled mode thermalizes to the electronics background temperature. This is used during the cooling phase of the phase sensitive measurements (PM) described in Section 4.2 to quickly cool both the axial and modified cyclotron mode back to their pseudo-thermal equilibrium.

If the axial mode is instead coupled on the upper sideband to the radial mode, the exponential growth of the driven axial mode and its decay from the resonator coupling impede each other. To model the decay, the axial ODE in Eq. (2.66) acquires the amplitude decay term $\frac{1}{\tau_A}A_z$. The amplitude decay time $\tau_A = 2\tau_E$ is twice the energy decay time since $e^{2t/\tau_A} = (e^{t/\tau_A})^2 \propto A_z^2 \propto E_z \propto e^{t/\tau_E}$. The changed ODE then results in a new Rabi-like frequency and axial eigenfrequencies.

$$\begin{aligned}
\dot{A}_x &= -i\tfrac{\Omega}{2}e^{i\delta t}A_z & \qquad \Omega''' &\coloneqq \sqrt{\Omega^2 - \delta^2 - 2i\delta\tau_A^{-1} + \tau_A^{-2}} \\
\dot{A}_z &= i\tfrac{\Omega}{2}e^{-i\delta t}A_x - \tfrac{1}{\tau_A}\dot{A}_z & \qquad \varpi_z &= \tfrac{1}{2}\left(i\tau_A^{-1} - \delta \pm i\Omega'''\right)
\end{aligned} \tag{2.71}$$

As $|e^{i\varpi_z t}| = e^{-\mathrm{Im}(\varpi_z)t}$, the solution of A_z will be bounded only if $0 \leqslant \mathrm{Im}(\varpi_z)$. Otherwise, the normalized amplitudes will grow exponentially and the particle energy will diverge.

$$0 \overset{!}{\leqslant} \min\bigl(\mathrm{Im}(\varpi_z)\bigr) = \min\bigl(\tau_A^{-1} \pm \mathrm{Re}(\Omega''')\bigr) = \tau_A^{-1} - \mathrm{Re}(\Omega''') \xrightarrow{\delta\to 0} \tau_A^{-1} - \sqrt{\Omega^2 + \tau_A^{-2}} < 0$$

The above limit shows that a tuned drive violates the restriction for bounded solutions of A_z, and more involved calculations show the same for detuned drives. Consequently, even when the particle is coupled to an axial resonator, a continuous PnA drive will excite the particle to inharmonic regimes.

2.3.4 Avoided Crossing and Precise $\omega_+ \pm \omega_z$ Determination

When measuring the axial frequency of the particle using dip methods as explained in Section 2.2.2, the axial mode is coupled to the resonator and absorbs the noise at its resonant frequency ω_z. If a drive on the lower sideband also couples the radial and axial modes, their energies will behave as described in Section 2.3.3 and their frequencies will be perturbed by the amplitude modulation of their envelopes A_i according to Eq. (2.62). In frequency space, the beat $\varpi_z = \frac{1}{2}\big(-\delta \pm \Omega'\big) = \frac{1}{2}\big(-\delta \pm \sqrt{\Omega^2+\delta^2}\big)$ modulating the free axial frequency ω_z equates to a superposition of two oscillations[14] at $\omega_{z,l/r} = \omega_z - \frac{\delta}{2} \pm \frac{\Omega'}{2}$.

For a tuned drive, the axial frequency dip will split into two, separated by Ω and symmetrical around the undriven axial dip. If the drive is detuned, the measured dips will become increasingly asymmetrical; one diverging away from ω_z with $\pm\delta$, the other converging as $\Omega^2/4\delta$. The dips also grow unbalanced, with the axial component of the diverging dip shrinking and absorbing less of the resonator noise. The axial component argument follows from an alternative treatment in Cornell et al. [97] where the mode evolution during coupling is treated as a time-independent superposition state of the axial and radial modes. The two frequency branches then correspond to distinct superpositions with different axial components and thus resonator interaction strengths.

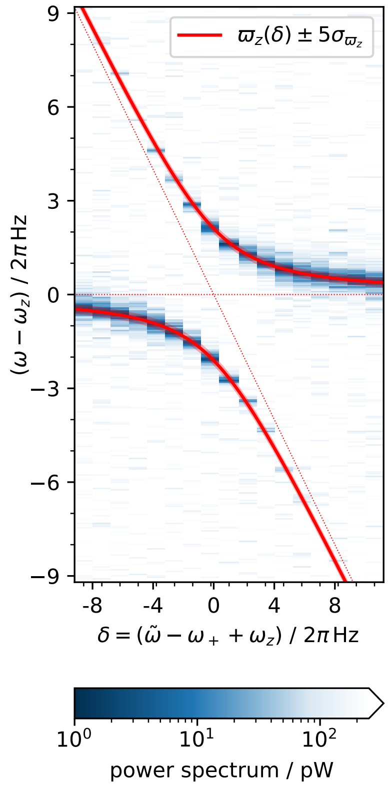

Figure 2.18: An avoided crossing when coupling at $\omega_+ - \omega_z + \delta$, measured using dip spectra. For a coupling drive at $-20\,\mathrm{dB_m}$, $\Omega_{\mathrm{fit}} = 4.22(5)$ Hz.

Making use of the above dip behaviour, a procedure can be defined to estimate the cyclotron frequency from the axial resonator signal alone. In the simplest case, the free axial frequency dip is measured, and a coupling drive $\tilde{\omega}$ is swept from the prior modified cyclotron frequency ω_+ guess downward until two symmetrical dips are visible. Due to the long acquisition time of dip spectra, however, a direct excitation drive of ω_+ is more sensible to determine a moderately precise initial value quickly. Afterwards, ω_+ can be refined in the above way, or via a bisection method. Instead of optimizing $\tilde{\omega}$ until the split dips are symmetrical, the precision can further be improved by using the scaled frequency sum

$$\tilde{\omega} + \omega_{z,l} - \omega_z + \omega_{z,l} = \big(\omega_+ - \omega_z + \delta\big) + \big(\omega_z - \tfrac{\delta}{2} - \tfrac{\Omega'}{2}\big) - \omega_z + \big(\omega_z - \tfrac{\delta}{2} + \tfrac{\Omega'}{2}\big) = \omega_+$$

to calculate ω_+ from ω_z, $\omega_{z,l}$, $\omega_{z,r}$, and $\tilde{\omega}$ directly. Since this method is independent of δ, no precision is lost when measuring ω_+ while slightly detuned.

[14] $\cos\big((\omega_z + \varpi_z)t\big) + \cos\big((\omega_z - \varpi_z)t\big) = 2\cos(\omega_z t)\cos(\varpi_z t)$

3 | Synthetic Phase Data

3.1 Signal Detection with a DFT

Using a discrete Fourier Transform, frequency components of sampled time domain signals can be calculated. For a pure sinusoidal signal, even if superimposed on other fluctuations, it allows a precise estimation of the signal amplitude and phase. However, both phase and amplitude are influenced by background noise and detuning of the signal frequency from the DFT frequency bins. These effects are described in this section.

3.1.1 Peak-Bin Misalignment

If the signal is sampled at an integer multiple rate of the signal frequency f_S, the DFT will yield the signal amplitude $|\vec{\rho}_\mathrm{S}|$ at the respective bin. Sampling at a slightly different frequency, and thus detuning the signal from the bin frequency, will decrease the maximum amplitude as the signal power is split between two DFT bins (Fig. 3.1, red trace); reaching its minimum of $\frac{2}{\pi}|\vec{\rho}_\mathrm{S}|$ at a sampling rate of $(k+\frac{1}{2})f_S$. To decrease this effect, a sinc function can be fitted to the DFT spectra to determine the actual maximum between the bins. Alternatively, the sampled signal can be windowed before applying the DFT to minimize tuning effects [90]. However, as shown in Fig. 3.1, this also decreases the absolute signal bin value and thus the SNR.

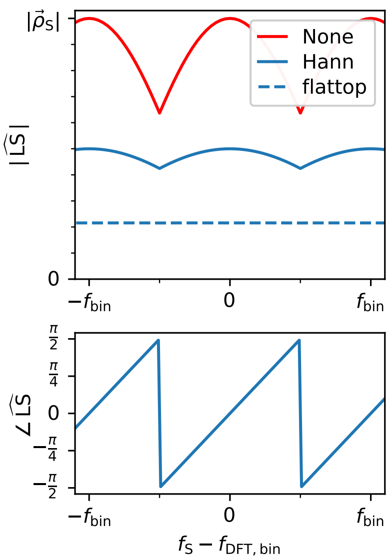

Figure 3.1: Signal bin DFT amplitude (top) and phase (bottom) dependence on frequency tuning and window choice.

The signal phase depends even more strongly on the detuning, sweeping over half of the phase domain inside every f_bin wide frequency span. This shift is independent of the window choice[1] and behaves as in Fig. 3.1 for conventional windows. Appendix A.2 further discusses phase flatness optimization.

[1]The phase shift is a result of minimizing the average squared phase deviation of the frequency-perturbed $f_\mathrm{S} = f_{\mathrm{S},0} + \delta f$ to equal phases in the time domain centre and $\pi\delta f/f_\mathrm{bin}$ shifted at the start.

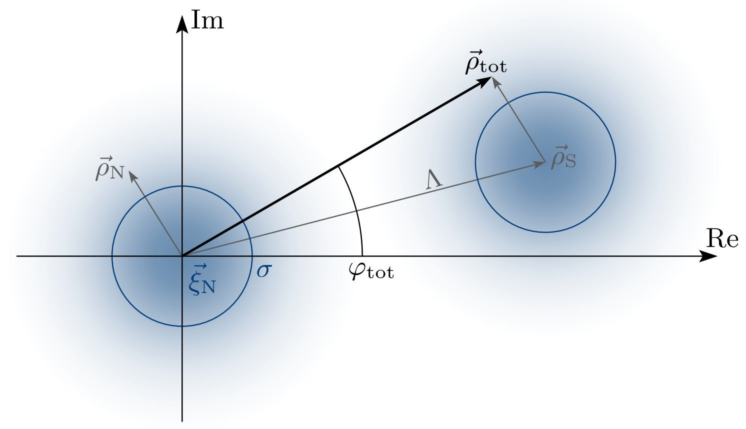

Figure 3.3: Signal $\vec{\rho}_S$ and Noise $\vec{\rho}_N$ contributions to the measured total value $\vec{\rho}_{\mathrm{tot}}$ in the DFT signal bin. $\sigma := \sigma(\mathrm{Re}\,\vec{\xi}_N) = \sigma(\mathrm{Im}\,\vec{\xi}_N)$, $\Lambda := |\vec{\rho}_S|$. $|\vec{\rho}_{\mathrm{tot}}|$ is Rice-distributed.

3.1.2 Noise-Contaminated Signals

When measuring a correctly binned sinusoidal signal with an FFT instrument like the SR1+ [138], the signal $\vec{\rho}_S$ will also be contaminated by noise from ADC binning, component Johnson-Nyquist noise etc. Furthermore, all the particle frequency measurements are done with a tuned resonator, whose Johnson-Nyquist noise $\vec{\rho}_{\mathrm{N,ref}}(f)$ dominates the other contributions for any acquired peak spectra such as Fig. 3.2, and changes both the signal bin amplitude and phase if the SNR is small.

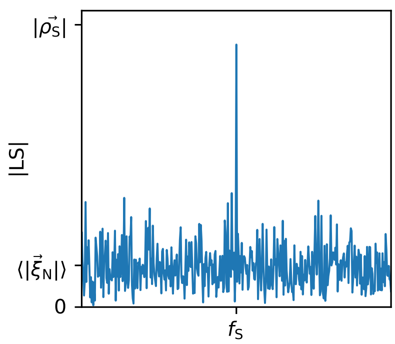

Figure 3.2: Signal DFT peak contaminated with approximately white noise in the frequency span.

If the peak is measured while roughly centred on the resonator, or if the DFT frequency span is thin enough that the relative change in absolute resonator impedance is negligible, then the background noise can be approximated as white, and its spectral density as constant. The scaling of noise power in the signal bin is then given by the $\vec{\rho}_N = \mathrm{NENBW}\,\vec{\rho}_{\mathrm{N,ref}}$ (see Section 3.4).

Let $\vec{\rho}_S$ be the complex DFT signal value with amplitude Λ and phase 0. Furthermore, let $\vec{\xi}_N$ be a circularly symmetric central complex normal distribution with standard deviation σ from which a noise vector $\vec{\rho}_N$ is sampled when acquiring a DFT spectrum. Using Eq. (3.14), σ can be calculated from the measured spectra with sampling frequency f_{S} or spectral densities using

$$\sigma = \sqrt{\frac{2f_{\mathrm{S}}}{\pi}}\,\langle \mathrm{LSD}_{\mathrm{noise}}\rangle = \sqrt{\frac{1}{2}}\sqrt{\langle|\vec{\xi}_N|^2\rangle} = \sqrt{\frac{2}{\pi}}\,\langle|\vec{\xi}_N|\rangle = \sigma_{\mathrm{Re}\,\vec{\xi}_N} = \sigma_{\mathrm{Im}\,\vec{\xi}_N}. \tag{3.1}$$

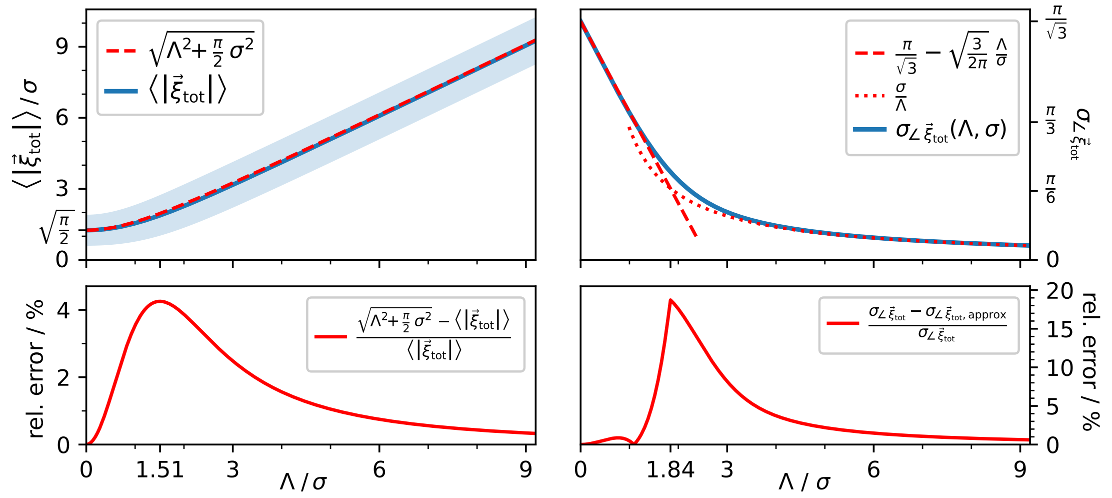

Figure 3.4: SNR dependence of $\left\langle\left|\vec{\xi}_{\rm tot}\right|\right\rangle$ (left) and $\sigma_{\angle\vec{\xi}_{\rm tot}}$ (right) and their closed-form analytical approximations for both. They deviate by less than 4.3 % and 18.8 % respectively.

When measuring a peak spectrum, the signal bin DFT value $\vec{\rho}_{\rm tot}$ will then sample from the distribution $\vec{\xi}_{\rm tot} = \vec{\rho}_S + \vec{\xi}_N = \Lambda + \vec{\xi}_N$, $\langle\vec{\xi}_{\rm tot}\rangle = \Lambda$ with the following properties:

$$\mathcal{P}(r,\varphi) = \frac{1}{2\pi\sigma^2}e^{-\frac{r^2-2r\Lambda\cos\varphi+\Lambda^2}{2\sigma^2}}, \qquad \mathcal{P}_\varphi(\varphi) = \int_0^\infty r\mathcal{P}(r,\varphi)\,\mathrm{d}r\,, \qquad \mathcal{P}_r(r) = \int_{-\pi}^{\pi}\mathcal{P}(r,\varphi)\,\mathrm{d}\varphi$$

$$\left\langle\left|\vec{\xi}_{\rm tot}\right|\right\rangle = \int_0^\infty r\mathcal{P}_r(r)\,\mathrm{d}r = \int_0^\infty e^{-\frac{r^2+\Lambda^2}{2\sigma^2}} I_0\!\left(\frac{\Lambda r}{\sigma^2}\right)\frac{r^2}{\sigma^2}\,\mathrm{d}r \approx \sqrt{\Lambda^2+\frac{\pi}{2}\sigma^2} \tag{3.2}$$

$$\left\langle\left|\vec{\xi}_{\rm tot}\right|^2\right\rangle = \Lambda^2 + 2\vec{\Lambda}\langle\vec{\xi}_{\rm N}\rangle + \langle\vec{\xi}_{\rm N}^{\,2}\rangle = \Lambda^2 + 2\sigma^2 \tag{3.3}$$

$$\sigma_{|\vec{\xi}_{\rm tot}|} = \sqrt{\left\langle\left|\vec{\xi}_{\rm tot}\right|^2\right\rangle - \left\langle\left|\vec{\xi}_{\rm tot}\right|\right\rangle^2} \approx \sqrt{2-\frac{\pi}{2}}\,\sigma \tag{3.4}$$

$$\left\langle\left(\angle\,\vec{\xi}_{\rm tot}\right)\right\rangle = 0 \qquad\qquad \zeta := \frac{\Lambda}{\sqrt{2}\sigma}\cos\varphi \tag{3.5}$$

$$\left\langle\left(\angle\,\vec{\xi}_{\rm tot}\right)^2\right\rangle = \int_{-\pi}^{\pi}\varphi^2\mathcal{P}_\varphi(\varphi)\,\mathrm{d}\varphi = \int_{-\pi}^{\pi}\varphi^2\left[\tfrac{1}{2\pi}+\tfrac{1}{2\sqrt{\pi}}\zeta\left(1+\operatorname{erf}\zeta\right)e^{\zeta^2}\right]e^{-\frac{\zeta^2}{\cos^2\varphi}}\,\mathrm{d}\varphi \tag{3.6}$$

$$\sigma_{\angle\,\vec{\xi}_{\rm tot}} = \sqrt{\left\langle\left(\angle\,\vec{\xi}_{\rm tot}\right)^2\right\rangle - \left\langle\left(\angle\,\vec{\xi}_{\rm tot}\right)\right\rangle^2} \approx \begin{cases} \frac{\sigma}{\Lambda} & \text{for } \Lambda > 1.84\sigma \\ \frac{\pi}{\sqrt{3}} - \sqrt{\frac{3}{2\pi}}\frac{\Lambda}{\sigma} & \text{for } \Lambda < 1.84\sigma \end{cases} \tag{3.7}$$

Notes:

(3.2): The approximation for $\left\langle\left|\vec{\xi}_{\rm tot}\right|\right\rangle$ is equivalent to treating the signal-noise superposition as a noise-noise superposition of Λ and $\left\langle\left|\vec{\xi}_N\right|\right\rangle = \sqrt{\frac{\pi}{2}}\sigma$.

(3.6): At decreasing SNR, $\mathcal{P}_\varphi(\pi) \not\approx 0$, the phase distribution begins to wrap, and $\sigma_{\angle\,\vec{\xi}_{\rm tot}}$ converges to $\frac{\pi}{\sqrt{3}}$. In this regime, $\sigma_{\langle\angle\,\vec{\xi}_{\rm tot}\rangle} = \frac{1}{\sqrt{N}}\sigma_{\angle\,\vec{\xi}_{\rm tot}}$ sharply underestimates the mean phase uncertainty for small sample sizes $N \lesssim 4\sigma^2/\Lambda^2$ (rough estimation).

3.2 Frequency Estimation from Phase Data

Contemporary fields, including microscopy, optical component characterization, surface topography, and holography repeatedly face the problem of reconstructing positional data from periodic phase data, and have done so by implementing algorithms [102, 103, 104] trying to unwrap these phases into some non-repeating domain from which the desired data can be calculated.

Here, the quantity to recover is the total number of oscillations performed by the particle in the time between initialization and readout. Fortunately, this number is proportional to the non-repeating phase domain, simplifying the required calculations. The only information to recover the oscillation number are the initial and final phases of the particle for a set of wait times, the exact lengths of those times, and a rough prior guess of the frequency. The following three algorithms give increasingly robust ways of recovering the oscillation number from the above information.

3.2.1 Algorithm 1: Phase Unwrapping

Let $X \subseteq \mathbb{R}^{\mathrm{dim}}$ be the measurement domain. (1D for time series and 2D for terrain data). Over this domain, some physical quantity $q\colon X \to \mathbb{R}$ needs to be recovered. Only the phase data $\varphi\colon \mathbb{R} \to \mathbb{R}/2\pi\mathbb{Z}, q \mapsto \varphi(q)$ is known at each point $\vec{x} \in X$: $\varphi(\vec{x}) := \varphi\big(q(\vec{x})\big)$. It is assumed that φ is smooth and increasing, and X is complete and connected. φ should be strongly monotonic in q. Otherwise, there is no unambiguous way to locally infer changes in q from changes in φ. However, φ is also periodic over q with some period τ. The apparent contradiction is circumvented since increasing a phase by 2π results in itself again because the topological space on which phases exist is an oriented topological circle with circumference 2π. Now the *unwrapped phase* function $\tilde{\varphi}$ can be constructed from φ:

$$\tilde{\varphi}\colon \mathbb{R} \to \mathbb{R},\ \tilde{\varphi}(q) \mapsto 2\pi\tau \left\lfloor \frac{q}{\tau} \right\rfloor + \varphi(q \bmod \tau). \tag{3.8}$$

$\tilde{\varphi}$ is still smooth and strictly monotonic, but not constrained into a 2π interval anymore. It is also not periodic. Increasing q by one period increases $\tilde{\varphi}$ by 2π. Inverting Eq. (3.8), the unwrapped phase can be transformed directly into the desired physical quantity. However, the phase measurement only produces $\varphi(\vec{x})$. And without prior knowledge about $q(\vec{x})$, the $\vec{x}$ dependent unwrapped phase $\tilde{\varphi}(\vec{x})$ is also unknown. However, the difference in $\tilde{\varphi}$ between two points $\vec{x}_1, \vec{x}_2 \in X$ can be calculated from $\tilde{\varphi}$ by integrating its gradient along any path $\mathcal{C}_{\vec{x}_1,\vec{x}_2}$ from $\vec{x}_1$ to $\vec{x}_2$:

$$\Delta\tilde{\varphi}(\vec{x}_1, \vec{x}_2) = \varphi(\vec{x}_2) - \varphi(\vec{x}_1) = \int_{\mathcal{C}_{\vec{x}_1,\vec{x}_2}} \boldsymbol{\nabla}_{\vec{x}}\, \varphi(\vec{x}) \cdot \mathrm{d}\vec{x} \tag{3.9}$$

Using Eq. (3.9), $\tilde{\varphi}(\vec{x}) = \tilde{\varphi}(\vec{x_0}) + \Delta\tilde{\varphi}(\vec{x}_0, \vec{x}) + 2\pi k$ can be reconstructed over X up to a constant offset $2\pi k \in 2\pi\mathbb{Z}$. And since $\tilde{\varphi}^{-1}(\varphi + 2\pi k) = \tilde{\varphi}^{-1}(\varphi) + \tau k$, q can also be reconstructed up to a constant offset τk, or fully with any reference $q(\vec{x}_0)$:

$$\Delta q(\vec{x}_1,\vec{x}_2) = \tilde{\varphi}^{-1}\big(\varphi(\vec{x}_1) + \Delta\tilde{\varphi}(\vec{x}_1,\vec{x}_2)\big) - \tilde{\varphi}^{-1}\big(\varphi(\vec{x}_1)\big) = q(\vec{x}_2) + k\tau - q(\vec{x}_1) - k\tau$$

$$q(\vec{x}) = \tilde{\varphi}^{-1}\big(\varphi(\vec{x}_0)\big) + \Delta q(\vec{x}_0,\vec{x}) + k\tau \qquad \text{reconstruction up to const. } k\tau \tag{3.10}$$

$$= q(\vec{x}_0) + \Delta q(\vec{x}_0,\vec{x}) \qquad \text{full reconstruction} \tag{3.11}$$

In practice, only a finite amount of data exists, so X is not connected. Rather than integrating the phase gradient along a domain path to obtain the unwrapped phase difference, the sum over phase differences along a sequence in the domain must be taken instead. For this, reasonable assumptions about the maximum change $\Delta\varphi_{\max}$ between two neighbouring data points must be made. Because if $\Delta\varphi_{\max} \not\ll \pi$, the change magnitude starts to become ambiguous. For the naive 1D unwrappings implemented in most programming languages[2], phase changes are always assumed to be as small as possible, so a phase change between two data points by an amount greater than π leads to a shift of all later data points by $\pm 2\pi$ such that the current difference decreases below π. See [105] for a comparison of improvements on one-dimensional naive unwrapping. Many sophisticated algorithms exist, trying to extend unwrapping to phase dataset in higher dimensions [103, 106].

Unwrapping Phases for Frequency Measurements

Running the phase measurement of length N described in Chapter 3 yields particle phases $(\varphi_k)_{k<N}$ at delays $(k\Delta t + t_0)_{k<N}$. These delays are not exactly known in the experimental setup since instruments and setup cabling introduce further delays after triggering. However, the additional delay t_0 is constant, so it does not affect the unwrapped phase differences and can be ignored. With $q = \tilde{\varphi}$ and the sequence $k_1, \ldots, k_2$ as the only path between k_1 and k_2, Eq. (3.11) reduces to

$$\tilde{\varphi}(t_2) = \tilde{\varphi}(t_1) + \Delta\tilde{\varphi}(t_1,t_2) = \tilde{\varphi}(t_1) + \int_{t_1}^{t_2} \boldsymbol{\nabla}_t\, \varphi_p(t) \cdot \mathrm{d}t$$

$$\longrightarrow \tilde{\varphi}_{k_2} = \tilde{\varphi}_{k_1} + \Delta\tilde{\varphi}_{k_1,k_2} = \tilde{\varphi}_{k_1} + \sum_{k=k_1}^{k_2-1} (\varphi_{k+1} - \varphi_k)$$

where again it is assumed that $\Delta\varphi_{\max} = \varphi_k - \varphi_{k-1} < \pi$ for all $k < N$, so the phase difference is unambiguous. Using that $\tilde{\varphi}$ is the integral of angular frequency ω over time, the particle frequency is finally calculated as $\omega_p = \mathrm{d}/\mathrm{d}t\, \Delta\tilde{\varphi}_+(t_0,t)$ by linearly fitting the unwrapped phases against t_k. The unknown constant offset φ_0 of the unwrapped phase will only influence the y-intercept, not the slope. φ_0 is therefore not problematic for the frequency estimation, but it means that at least two phases need to be measured for any information about ω.

The precision of the estimated frequency scales with the delay time increments (see Section 3.5), so the aim is to maximize them. Consequently, $\Delta\varphi_{\max}$ such that $\Delta\varphi_{\max} \not\ll \pi$ increases, so other ways must be found to keep unwrapping unambiguous. Using prior

[2] Python (Numpy), Mathematica, Matlab, and Octave API references

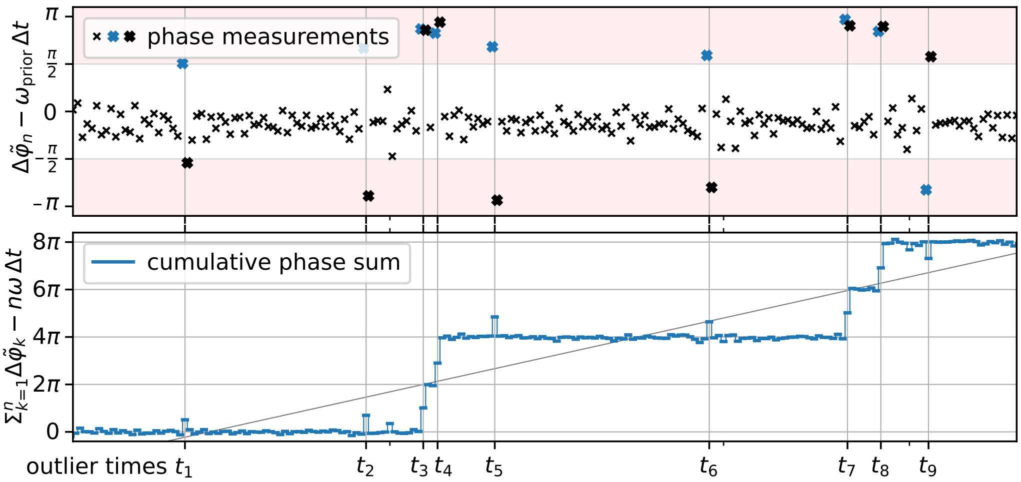

Figure 3.5: Unwrapped phase errors due to misdetected phases for a synthetic measurement with $\text{SNR}_{\text{measured}} = 13\,\text{dB}$, $\omega_{\text{prior}} = 2120\,\text{Hz}$ and $\omega = 2100\,\text{Hz}$ (see Chapter 3). Shown are the differences between the unwrapped phase changes $\Delta\tilde{\varphi}_{k,k+1}$ and the expected change $\omega_{\text{prior}}\Delta t$ (top), and between the total estimated and correct unwrapped phase $\tilde{\varphi}_k - \omega t_k$ (bottom). In this case, the phase drift leads to an extra frequency error of 7.1(3) Hz.

knowledge about ω, large $\Delta\tilde{\varphi}$ can be recovered by estimating the expected phase increase $\Delta\tilde{\varphi}_{\text{prior}} = \omega_{\text{prior}}\Delta t$ and choosing $\Delta\tilde{\varphi}$ as the value $\Delta\varphi + 2\pi k, k \in \mathbb{N}$ closest to $\Delta\tilde{\varphi}_{\text{prior}}$, which fails only when the uncertainty in $\Delta\tilde{\varphi}_{\text{prior}}$ propagated from ω_{prior} increases above π, resulting in multiple permissible $\Delta\tilde{\varphi}$. For example, if $\omega \approx 4(1)\,\text{Hz}$ is known, and a phase difference of $\frac{\pi}{2}$ over $\frac{3}{8}$s is measured, $\omega = \frac{10}{3}$Hz can be recovered, even though $\Delta\tilde{\varphi} = \frac{5}{4}\pi \not\ll \pi$. Larger delay time increments are limited by the required increasingly precise prior frequency knowledge.

3.2.2 Algorithm 2: Misdetection Improvements on Alg. 1

Noisy signals during the acquisition of phase data lead to a larger scatter in the measured phases and may even cause misdetection of the signal FFT bin, effectively randomizing the measured phase. For scatter $\sigma_\varphi \ll \pi$, it will only translate into the unwrapped phase scatter $\sigma_{\tilde{\varphi}} = \sigma_\varphi$ and thus into the linear fit of the slope frequency. For scatter $\sigma_\varphi \lesssim \pi$, incorrect unwrappings may occur because even though each measured phase can not deviate further than π from its correct value, their difference can deviate up to 2π. Differences with deviations larger than π then directly cause incorrect unwrappings. Two illuminating example cases are considered for a signal with phase $\tilde{\varphi}_{\text{k,signal}} \approx 2\pi k$, $\varphi_{\text{k,signal}} \approx (2\pi k \bmod 2\pi) = 0$, and phase scatter $\sigma_\varphi \lesssim \pi$:

Case 1: $\varphi_k = (0.3\pi, -0.9\pi, -0.2\pi)_k$.
Calculating the phase differences results in $\Delta\varphi_{k,k+1} = (-1.2\pi, 0.7\pi)_k$. Expecting $\Delta\tilde{\varphi} = 2\pi$, they will be unwrapped to $\Delta\tilde{\varphi}_{k,k+1} = (2.8\pi, 2.7\pi)_k$. Thus, $\Delta\tilde{\varphi}_{0,2} = 5.5\pi$, even though the actual phase has only increased by $3.8\pi - 0.3\pi = 3.5\pi$. All $\varphi_{\geq 1}$ are unwrapped by an extra 2π, and the fitted frequency is too large.

Case 2: $\varphi_k = (0.3\pi, -0.9\pi, 0.2\pi)_k$.
Now, $\Delta\varphi_{k,k+1} = (-1.2\pi, 1.1\pi)_k$ and $\Delta\tilde{\varphi}_{k,k+1} = (2.8\pi, 1.1\pi)_k$. Thus, $\Delta\tilde{\varphi}_{0,2} = 3.9\pi$, the same as the actual phase increase $4.2\pi - 0.3\pi = 3.9\pi$. Only φ_1 is unwrapped incorrectly, to 3.1π instead of 1.1π. All subsequent $\tilde{\varphi}_{>1}$ are corrected because the overestimated unwrap $\Delta\tilde{\varphi}_{0,1}$ is followed by an underestimated unwrap $\Delta\tilde{\varphi}_{1,2}$.

In both cases a single phase outlier with a deviation $> \frac{\pi}{2}$ causes itself, and potentially all future points to be unwrapped incorrectly. Identifying and removing those outliers is thus beneficial for improving the estimated frequency. Direct detection via the measured frequencies is only possible in the above examples because the expectation phase was constant. However, case 1 will cause two consecutive unwrapped phase changes $\Delta\tilde{\varphi}$ to be increased similarly against the background. Conversely, case 2 will cause one of the two consecutive unwrapped phase changes to be increased, and the other to be decreased. Figure 3.5 shows these patterns, and the effects of the phase outliers on unwrapping for one of the synthetic test data sets from Chapter 3. The two behaviours described in cases 1 and 2 are by far the most common effects of phase misdetection in the $\sigma_\varphi \lesssim \pi$ regime because they result from an isolated misdetection. For $\sigma_\varphi \approx \pi$, misdetection rates increase and compound effects will dominate.

The above outliers are detected by convolving the difference between the measured and expected phase changes with 2 different kernels, $[1, 1]$ and $[1, -1]$. Large absolute values after convolution correspond to misdetections equivalent to cases 1 and 2. The resultant arrays are then combined by taking the maximum of the absolute values at each index. If any of the entries is larger than π, an outlier pair like the ones in Fig. 3.5 has been found, the misdetected phase can be deleted, and all subsequent phases can be corrected if the large entry resulted from the $[1, 1]$-kernel convolution.

3.2.3 Algorithm 3: FFT-Based Complex-Space Phase Fitting

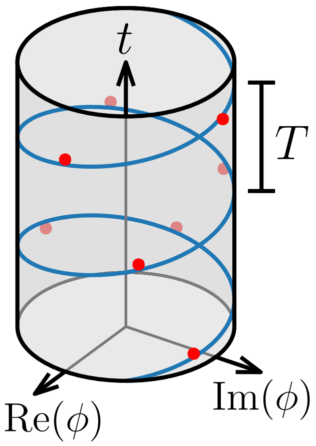

Figure 3.6: A $(\phi_{\text{signal}}(t), t)$ helix and (ϕ_k, t_k) visualized on a cylinder in $\mathbb{C} \times \mathbb{R}$

The previous algorithms have tried to circumvent the fundamental problem of real number phase embeddings not being smooth with respect to phase changes by unwrapping the mapped phases. While somewhat intuitive, unwrapping may introduce additional errors into the phase data as shown in Section 3.2.2. Directly analyzing the phase data in its domain avoids this problem, but working in $\mathbb{R}/2\pi\mathbb{Z}$ is problematic. However, $\mathbb{R}/2\pi\mathbb{Z}$ can be mapped as a unit circle into $\mathbb{C}$ by $\phi_{\mathbb{C}} = e^{i\varphi_{\mathbb{R}/2\pi\mathbb{Z}}}$ without any discontinuities or distortions, and with the only caveat that phase difference can not directly be substituted by complex distance. Instead, a function mapping complex distance $\|\phi_2 - \phi_1\|$ between two points ϕ_1, ϕ_2 on the unit circle to their phase difference $\angle(\phi_1, \phi_2)$ needs to be applied:

$$|\varphi_2 - \varphi_1| \stackrel{!}{=} \angle(\phi_1, \phi_2) := 2\arcsin\left(\tfrac{1}{2}\|\phi_2 - \phi_1\|\right) \quad (3.12)$$

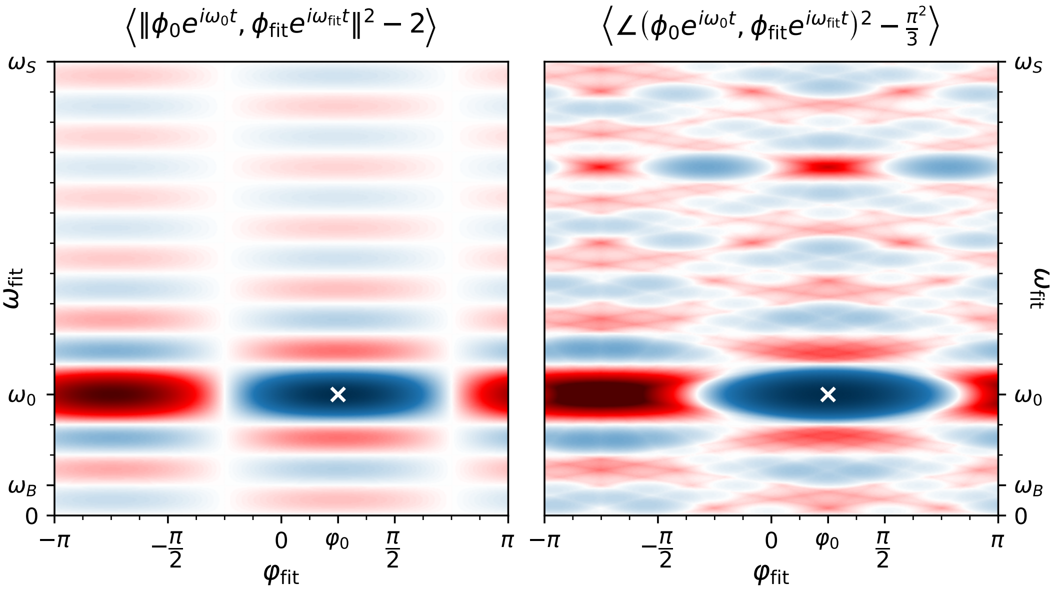

Figure 3.7: Residuals of the phase function $\phi_{\text{fit}} e^{i\omega_{\text{fit}} t}$ for a sequence of $N = 15$ phases $\phi_0 e^{i\omega_0 k\Delta t}$ with $\omega_0 = 4\omega_B$ and $\phi_0 = \frac{\pi}{4}$. The residuals are periodic over $\Delta\phi_{\text{fit}} = 2\pi$ and $\Delta\omega_{\text{fit}} = \omega_S$ due to the phase nature and frequency aliasing. Phases and times are mean-normalized to orthogonalize ϕ_{fit} and ω_{fit}. Otherwise, the residuals are skewed along ϕ_{fit}. Even though the global minimum is correctly located at (ϕ_0, ω_0), a multitude of other local minima are scattered over the space and prevent fitting. For $N \gg 1$, the square root of the phase residual envelope along ω_{fit} resembles Thomae's function [109]. $\omega_S = \frac{2\pi}{\Delta t}$ and $\omega_B = \frac{2\pi}{N\Delta t}$ are the sampling and bin width frequencies of the phase sequence.

In $\mathbb{C}$, a signal component with frequency ω_0 will have a phase $\phi(t) = \phi_0 e^{i\omega_0 t}$ and can be fitted against the measured complex phases without further modifications to obtain ω. Residuals can either use the squared complex distances or map them to squared phase differences using Eq. (3.12). While technically less correct, squared complex distances are easier to calculate and penalize large phase differences less strongly, so the effect of misdetected phase outliers on the frequency estimation is diminished. As in the phase unwrapping procedure, the range of ω that this approach can correctly estimate without prior frequency information is limited by aliasing. Using Fig. 3.6 for clarification; If ω_0 is increased such that the $(\phi_0 e^{i\omega_0 t}, t)$ helix completes one additional turn between two neighbouring points, it will still intersect all the drawn $(\phi_k, k\Delta t)$ and minimize the fit residuals. It is only possible to determine the underlying frequency from which the phases were sampled up to $\omega_0 \in \omega_{\text{fit}} + k\omega_S$, where $k \in \mathbb{Z}$ and $\omega_S := 2\pi \big/ \Delta t$ is the angular sampling frequency [107, 108]. Using prior frequency information, the correct frequency can be selected.

Complicating the direct fit approach further, even initial fit parameters $(\phi_{\text{fit}}, \omega_{\text{fit}})$ within $\pi \big/ \Delta t$ of ω_0 will generally not converge to ω_0. As shown in Fig. 3.7, the fit residual is locally minimized (blue) at many $(\phi_{\text{fit}}, \omega_{\text{fit}})$ points, so without exhaustive sampling of the fit space, preceding data analysis is needed to choose favourable initial fit parameters. Applying a DFT on $(\phi_k, k\Delta t)$ yields an amplitude and a phase for each frequency component $\tilde{k}\omega_B$ of the phase data if it were periodic with a period of $N\Delta t$. If the phase data is dominated by the signal at angular frequency ω_0, the frequency component $\hat{\omega}_{\mathrm{DFT}}$ closest to ω_0 will have the greatest DFT amplitude, so ω_0 can be determined down to $\hat{\omega}_{\mathrm{DFT}} \pm \frac{\omega_B}{2}$. At higher noise levels and $\omega_0 \approx (\tilde{k} + \frac{1}{2})\omega_B$, the next closest frequency component may have a higher amplitude, which increases the determined frequency span to a width of $\lesssim 2\omega_B$.

Referring again to Fig. 3.7, the global minimum's basin of attraction is $\lesssim 2\omega_B$ wide for both residual types, so $\hat{\omega}_{\mathrm{DFT}}$ can be used as the initial fit frequency. The corresponding DFT phase, however, strongly depends on the difference between $\hat{\omega}_{\mathrm{DFT}}$ and ω_0 and can not be used to estimate ϕ_0. Since the global minimum's basin of attraction covers around half of the ϕ_{fit} span, independent of ω_S and ω_B, sampling the fit residuals at 4 or more equidistant phases[3] and using the phase with minimum error as the initial fit phase is sufficient.

After determining suitable initial $(\phi_{\mathrm{fit},0}, \omega_{\mathrm{fit},0})$ via the DFT and phase sampling, the phase data can be least-square fitted by any optimization routine[4]. Similar methods are used in accelerator [112] and astrophysics [113] for precisely determining a dominating frequency. As phase difference scales linearly even with non-infinitesimal variations in both ϕ_{fit} and ω_{fit} sufficiently close to (ϕ_0, ω_0) where $\angle\left(\phi_k, \phi_{\mathrm{fit}} e^{i\omega_{\mathrm{fit}} k\Delta t}\right) \ll \pi$, using phase difference residuals results in a parabolic error function in a region X around (ϕ_0, ω_0) as in the right part of Fig. 3.7. This permanently degenerates fitting into a *linear* least square problem after the optimization routine reaches X, guaranteeing convergence to the global minimum. This is the main advantage of using phase-difference residuals, and the reason why they are used in the Python implementation in Appendix A.3 that is used for the cyclotron phase frequency estimation.

3.3 Test Setup for Generation of Synthetic Phase Data

To develop and test the acquisition of the downconverted axial signal in advance of real data, a test setup emulating the signals resulting from the phase-sensitive measurements was needed. These signals are downconverted sinusoidal oscillations of varying amplitude, together with noise of approximately constant linear spectral density in the frequency band around the signal, also with varying amplitude. However, scaling the signal proportionately to the noise would change neither the SNR nor the precision with which the SR1 [138] can resolve its phase. Thus, only the ratio of $U_{\mathrm{signal,pp}}$ to σ_{noise} is relevant[5] and the signal amplitude can be kept constant. The signal downconversion via a single-sideband-downconverter [139] is well understood and only decreases the axial frequency before measuring it with the SR1. Therefore, this step can be skipped in the

[3] The implementation in Appendix A.3 samples 12 phases for improved resilience against further localized minima in the small gradient regions of the global minimum's attraction basin due to noise...

[4] ...and uses the Levenberg-Marquardt algorithm [110] implemented in SciPy [111] for fitting the phase data. It is partially based on gradient descent.

[5] Or any other quantity scaling linearly with signal amplitude and inverse noise standard deviation.

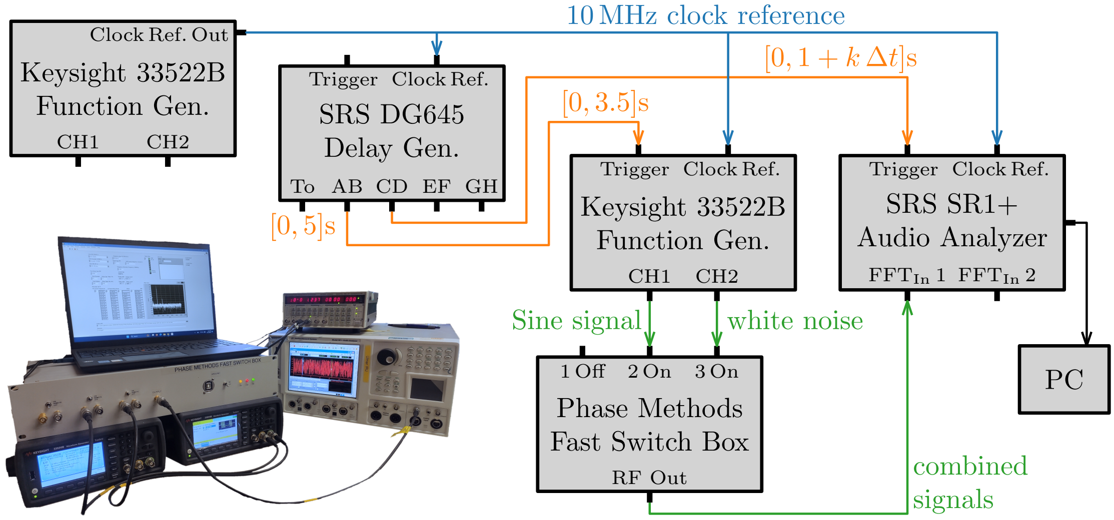

Figure 3.8: Synthetic phase data can be created by a triggered function generator, yielding both the noise and signal components, together with a power combiner circuit and a triggered DTF signal analyzer. The signal flow diagram illustrates how the synthetic measurements sequence was realized, how the delays were timed, and which instruments were used. The resulting instrument assembly is diplayed in the inset photograph.

test setup by using a signal in the FFT bandwidth of the SR1 directly. Finally, the test setup should support initializing the sinusoidal signal at a constant phase and measuring it after variable delays, emulating the phase-sensitive measurement scheme. After the phase measurements of the SR1, this also allows benchmarking of potential frequency estimation algorithms on realistic phase data, which is discussed in the next section. Decaying signal amplitudes are deliberately not included in the setup and will be considered later. The test setup shown in Fig. 3.8 is arranged to provide such synthetic data to the SR1.

All instruments run on the same 10 MHz reference clock provided by one of the 33522B function generators [140]. In the final setup, the referencing will be done by a rubidium clock [141]. Every five seconds, the DG645 delay generator [142] initiates a standalone measurement sequence leading to one measured FFT spectrum and one signal phase. At $t = 0\,\mathrm{s}$, both outputs of the other 33522B function generator are activated and source their respective functions until the delay pulse ends at $t = 3.5\,\mathrm{s}$: a sinusoidal signal pulse with amplitude $U_{\mathrm{signal,pp}} \in \{5\,\mathrm{mV}, 500\,\mathrm{mV}\}$ and phase $\varphi_0 = 0$, and digital white noise with a bandwidth of $100\,\mathrm{kHz} > f_{S,\mathrm{FFT}}$ and maximum amplitude of $4.64\sigma_{\mathrm{noise}} \approx U_{\mathrm{noise,pp}} \in 1.1^n \cdot 3\,\mathrm{mV}, n \in \mathbb{N}$. Both functions are combined with equal relative weight by feeding them into RF ports 2 and 3 of the PM switch box [143], which are manually switched to non-blocking via the front panel switches. Internally, the signals are fed through the open switches [144] into power combiners [145], otherwise acting only as single signal passthroughs. Combined into one signal, they are then fed into the input port of the SR1. After letting the signal evolve for at least one second, the SR1 FFT is triggered with a falling edge at $t = 1\,\mathrm{s} + k\Delta t$, where $k \in \mathbb{N}$ is incremented each sequence, and Δt is a setup specific constant minimum time increment to keep sequence timings invariant[6]. Starting after the trigger the signal is acquired over a span of time T_sample equal to the inverse of the desired FFT spectrum Bandwidth[7], after which the SR1 raises a service request over its GPIB connection to the PC, prompting it to store the FFT spectrum for analysis of the evolved signal phase after $t = 1\,\mathrm{s} + k\Delta t < 3.5\,\mathrm{s} - T_\mathrm{sample}$ in the last 1.5 s of the sequence. Afterwards, the sequence repeats until all required k, $U_\mathrm{signal,pp}$, and $U_\mathrm{noise,pp}$ are sampled.

3.4 Validation of Generated Data

At given FFT parameters, setting $U_\mathrm{signal,pp}$ and $U_\mathrm{noise,pp}$ and subsequently running a single measurements sequence results in an FFT spectrum, which is quantified by storing the phase and SNR of the signal spectrum, where the noise level is approximated as the median bin value of the linear spectrum to avoid the need for filtering the signal peak and its harmonics out of the background spectrum before averaging. For the measured values, this leads to the SNRs shown in Fig. 3.10. To calculate the expected SNRs, all instruments are characterized.

Keysight 33522B Function Generator [140]
By correctly setting the 33522B output and SR1 input impedances, a sinusoidal signal can be sourced at a given peak-to-peak voltage of $U_\mathrm{signal,pp}$. In the generator interface, the noise voltage range is defined by another peak-to-peak voltage $U_\mathrm{noise,pp}$, which the output signal should never exceed. The generated noise is specified as white up to a maximum frequency $\hat{f}_\mathrm{noise}$ and is supposed to be normally distributed, and thus defined most meaningfully via its standard deviation σ_noise, for which the manual [140] provides a conversion crest factor of $U_\mathrm{noise,pp} \approx 4.6\sigma_\mathrm{noise}$. Testing the distribution for relevant values of $U_\mathrm{noise,pp} = 0.1\,\mathrm{V}$ and $1\,\mathrm{V}$ and $\hat{f}_\mathrm{noise} = 50\,\mathrm{Hz}$ to $6\,250\,000\,\mathrm{Hz}$ (e.g: Fig. 3.9) shows that it approximates a normal distribution sufficiently well up to about $2\sigma_\mathrm{noise}$, after which it starts undersampling the distribution tails[8]. Numerical

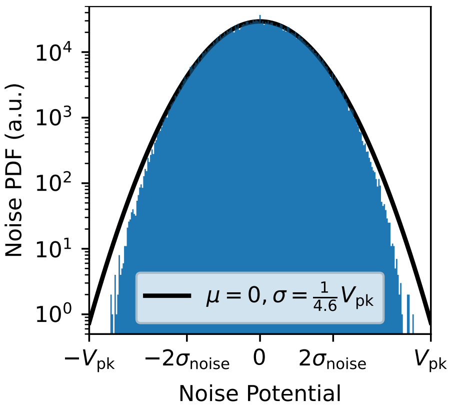

Figure 3.9: Measured and expected normal distribution of the generated 33522B white noise with $f_\mathrm{S} = 312.5\,\mathrm{kHz}$, $\hat{f}_\mathrm{noise} = 20\,\mathrm{kHz}$ and $V_\mathrm{pk} = 0.5\,\mathrm{V}$. The high-variance tails are undersampled.

[6]The SR1 FFT sampling rate of 64 kHz is clocked independently from the external trigger. An unknown extra delay of up to $T_\mathrm{sample} = 15.625\,\mu\mathrm{s}$ is thus introduced depending on the trigger timing when initiating the data acquisition, causing artificial phase noise. Using multiples of T_sample for both sequence periods and phase-measurement delay time increments keeps the extra delay, and thus the phase offset, constant. Subdividing the maximum FFT span proportionately increases T_sample.

[7]FFT parameters of $N = 8192$, $T = 256\,\mathrm{ms}$, $f_\mathrm{S} = 32\,\mathrm{kHz}$, $f_\mathrm{BW} = 3.906\,25\,\mathrm{Hz}$ were used.

[8]The noise signal was recorded with $f_S \gg \hat{f}_\mathrm{noise}$ and thus measures mostly intermediate values. However, as the total power of the noise is split into its frequency components and the standard deviation

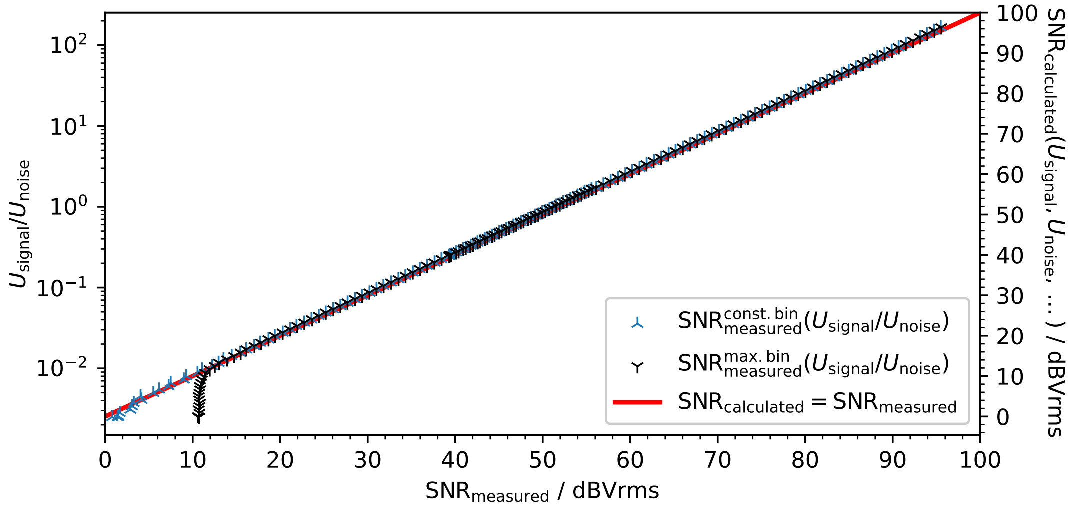

Figure 3.10: To validate the theoretical description of the synthetic phase measurments, measured and calculated SNRs of the generated synthetic data ($f = 2.1$ kHz) are compared for function generator signal-noise voltage ratios between $2 \cdot 10^{-2}$ and $num2e2$. The measured values agree well with the semi-analytical prediction. Either the maximum LS bin or a predefined bin can be chosen as the one containing the signal. Choosing the maximum bin, the signal starts to get misqualified at SNR $\lesssim 12$. However, a constant bin can only be chosen via prior knowledge of the signal frequency.

calculations of the distribution mean ($\mu = 6.5(2) \cdot 10^{-4}\, U_{\text{noise,pp}}$) and standard deviation ($4.642(1)\,\sigma = U_{\text{noise,pp}}$) are in good agreement with the manual, with an insignificant mean offset, and an improved crest factor value of 4.642(1).

Phase Methods Fast Switch Box [143]

The 3 inputs of the PM switch box are individually switched and then combined pairwise as a binary tree, after which the resulting line is switched again ahead of its connection to the box output. Inputs 2 and 3 are combined first, and then the output of the first combination step is combined again with input 1. To keep the relative strengths between the noise and sinusoidal signal constant, inputs 2 and 3 are used, and input 1 is switched to a 50 Ω ground termination.

Each combining step in a resistive power splitter attenuates the signals by at least 6 dB[9], with the manual of the ZFRSC-42+ 0°, 50 Ω resistive power splitters [145] used in the PM switch box specifying a total loss of at most 6.2 dB in the frequency range from DC to 100 MHz. Together with the switching losses of approximately 0.6 dB per ZASWA-2-50DRA+ switch [144], a total attenuation of 13.2 dB ($U_{\text{out}} \approx 0.22\, U_{\text{in}}$) is measured for both input ports.

of a sine wave does not change with sampling rate, this does not affect the estimation of σ_{noise}.

[9]Resistive power splitters are symmetric with respect to their ports, so the power of any input signal will be split evenly between the two other ports when correctly terminated, irrespective of the use as splitter or combiner (−3 dB). Furthermore, half of the of the input power is dissipated in the internal resistances required for impedance matching (−3 dB)

SRS SR1+ Audio Analyzer [138]

Inputs fed into the SR1+ are potentially heterodyned and decimated depending on the chosen FFT frequency span, and are filtered to eliminate alias effects from the discarded portions of the frequency spectrum ([138], page 128). As no information about the kind of filtering is available, the SR1 time domain standard deviation σ_{SR1} was measured for white noise of constant standard deviation and varying noise bandwidths, shown in Fig. 3.11. Using the model of a perfect low pass filter with its cutoff at f_C, σ_{SR1} should stay constant up to $\hat{f}_{\mathrm{noise}} = f_C$, after which it should decrease proportional to $\hat{f}_{\mathrm{noise}}^{-1/2}$, as only $f_C \,/\, \hat{f}_{\mathrm{noise}}$ of the noise power remains in the unfiltered frequency region, with σ_{SR1} scaling as the square root of noise power. Figure 3.11 agrees well to the model and predicts $f_C = 15.342(3)\,\mathrm{kHz}$. With the full FFT spectrum going up to 16 kHz, the filter knee will distort the upper edge, which explains why only frequencies up to 12.5 kHz are available from the SR1 FFT analyzer panel. For the 100 kHz noise bandwidth used in the synthetic data generation, the noise attenuation of the SR1 can be calculated as 8.141(1) dB ($\sigma_{SR1} = 0.3917(1), \sigma_{\mathrm{noise,pp}}$).

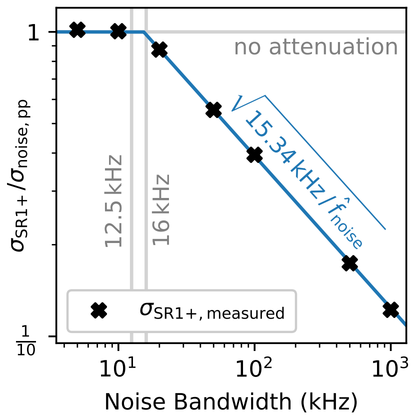

Figure 3.11: The SRS SR1+ contains a lowpass filter with a knee at $f_C \approx 16\,\mathrm{kHz}$, visible by the increased attenuation of input noise with bandwidths above f_C. Only bins at $f < 12.5\,\mathrm{kHz}$ are shown to users.

After recording the time domain signal, the SR1 calculates the linear spectrum (LS), on which the noise floor and signal peak can be seen. For the sinusoidal signal, the calculation is quite straightforward, with the only caveat that when starting with peak-to-peak voltages, as $P \propto U_{\mathrm{rms}}^2 = \frac{1}{2}U_{\mathrm{pk}}^2 = \frac{1}{8}U_{\mathrm{pp}}^2$, power will be scaled down by a factor of eight[10]. Using $U_{\mathrm{SR1,signal,pp}}$ as the peak-to-peak signal voltage in the SR1 time domain record,

$$\mathrm{PS}_{\mathrm{signal}} = \frac{1}{8}\,U_{\mathrm{SR1,signal,pp}}^2 \qquad \text{(power spectrum)}$$
$$\mathrm{LS}_{\mathrm{signal}} = \frac{1}{\sqrt{8}}\,U_{\mathrm{SR1,signal,pp}}. \qquad \text{(linear spectrum)}$$

For noise, the linear spectral density (LSD) is the more meaningful quantity, as it does not scale with the number of data points taken. The linear spectrum can then be obtained from the LSD and used to calculate the median LS value. The equations use $\sigma_{\mathrm{SR1,noise}}$ as the standard deviation of the noise voltage in the SR1 time domain record, f_S as its sampling frequency, and N as the total number of recorded points. The normalized equivalent noise bandwidth (NENBW) $\mathcal{N}$ of the FFT window used in the calculation of signal and noise spectra depends on the window choice.

[10] The SR1 confusingly uses oscillation-specific quantities like rms-voltage for general time domain data as well: $U_{\mathrm{pp}} \coloneqq 2U$, $U_{\mathrm{pk}} \coloneqq U$, $U_{\mathrm{rms}} \coloneqq U \,/\, \sqrt{2}$.

$$\langle \mathrm{PSD_{noise}} \rangle = \frac{2}{f_S}\,\sigma^2_{\mathrm{SR1,noise}} \qquad \text{[114], chapter 12} \qquad (3.13)$$

$$\langle \mathrm{LSD_{noise}} \rangle = \sqrt{\frac{\pi}{4}\,\langle \mathrm{PSD_{noise}} \rangle} = \sqrt{\frac{\pi}{2f_S}}\,\sigma_{\mathrm{SR1,noise}} \qquad \text{[115], part I} \qquad (3.14)$$

$$\langle \mathrm{LS_{noise}} \rangle = \sqrt{\mathcal{N}\frac{f_S}{N}}\,\langle \mathrm{LSD_{noise}} \rangle = \sqrt{\frac{\pi\mathcal{N}}{2N}}\,\sigma_{\mathrm{SR1,noise}} \qquad \text{[90], chapter 9} \qquad (3.15)$$

$$\mathrm{median}(\mathrm{LS_{noise}}) = 2\sqrt{\frac{\ln 2}{\pi}}\,\langle \mathrm{LS_{noise}} \rangle = \sqrt{\frac{2\mathcal{N}\ln 2}{N}}\,\sigma_{\mathrm{SR1,noise}}, \qquad \text{properties of the Rayleigh distribution}$$

The SR1 provides a proprietary Blackman-Harris+ window ($\mathcal{N}_{\mathrm{BH+}} = 2.632(8)$)[11] with a wider main lobe but better side-lobe suppression than the rectangular ($\mathcal{N}_{\sqcap} = 1$), Hann ($\mathcal{N}_{\mathrm{Hann}} = 1.5$) and Blackman-Harris ($\mathcal{N}_{\mathrm{BH}} \approx 2$) windows. It is used in the FFT spectra calculations for the synthetic data to minimize the power-bleeding effects between noise and signal to minimize errors in SNR. For the measurement of cyclotron frequencies, increased noise power will decrease the precision of the measured phase, so only the minimization of noise power $P_{\mathrm{noise,bin}}$ in the signal bin needs to be considered. In the limit of wideband noise respective to the main lobe width, $P_{\mathrm{noise,bin}} \to \mathcal{N}\,\mathrm{PSD_{noise}}$, and thus the rectangular window will be used as it minimizes the NENBW.

Combining all the above signal and noise attenuations from the instruments with the LS calculation from the time domain, scaling the signal values down because the signal is not perfectly on the FFT bin[12], and converting linear units to dB yields the calculated SNR in Fig. 3.10, which agrees well with the measured SNR for a wide range of $U_{\mathrm{signal,pp}} / U_{\mathrm{noise,pp}}$ ratios.

3.5 Characterizing the Frequency Estimation Algorithms

Running the three frequency estimation algorithms described in Section 3.2 on the phase data generated in Section 3.3 yields Fig. 3.12. In all cases a signal frequency of $f_{\mathrm{Signal}} = 2.1\,\mathrm{kHz}$ is chosen for the phase data generation, and a frequency of $f_{\mathrm{init}} = 2.12\,\mathrm{kHz}$ for the initial guess of f_{Signal} that the algorithms depend on for their estimation. The initial frequency inaccuracy of 20 Hz is shown as a reference ;ine in Fig. 3.12. Estimations with errors of this magnitude mean the algorithm has broken down.

At high SNRs, the accuracy of all algorithms is equal. Each measured phase can be mapped unambiguously to the corresponding phase increase In the rows in Fig. 3.12, the value and uncertainty of the estimated frequencies are the same for all algorithms, which hints at the fact that in this regime, the errors are a result of the intrinsic phase scatter from the noisy signal, and not of inadequacies of the estimation algorithms. At SNRs below 28(1) $\mathrm{dB_{Vrms}}$, the signal phase starts to get misdetected when using the maximum

[11] The Blackman-Harris+ NENBW is not specified in the manual [138], and was thus measured with generated white noise. Measurements for Hann and Blackman-Harris windows yield $\mathcal{N}_{\mathrm{Hann}} = 1.50(2)$ and $\mathcal{N}_{\mathrm{BH}} = 2.01(2)$.

[12] The effect is small for windows with large NENBWs. At $f_{\mathrm{Signal}} = 2100\,\mathrm{Hz}$ and $f_{\mathrm{Bin}} = 2101.5625\,\mathrm{Hz}$, the scaling factor is about 0.964.

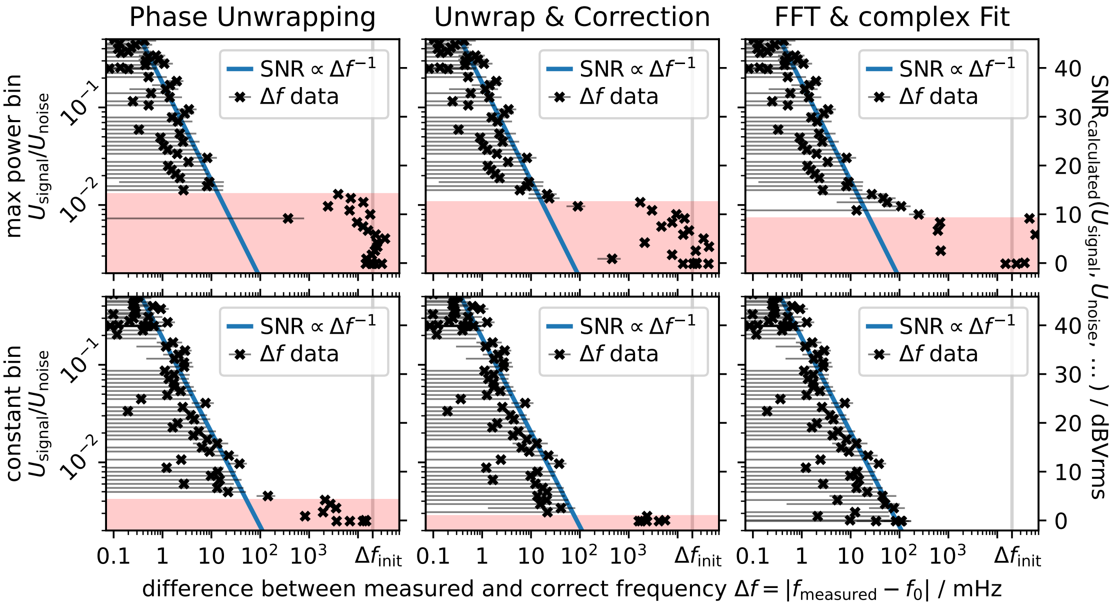

Figure 3.12: Frequency estimation errors for the three frequency estimation algorithms on the synthetic phase data ($f = 2.1\,\mathrm{kHz}$, $N_{\mathrm{phases}} = 200$). Using the phase data from the same maximum-power bin improves the estimation accuracy, and so does usage of a more sophisticated FFT based algorithm.

power bin, and increasingly more so down to $12.1(1)\,\mathrm{dB_{Vrms}}$, where more than half of the phases are random. Direct phase unwrapping is not very robust against random phases, even with misdetection correction, and breaks down at around $12\,\mathrm{dB_{Vrms}}$ to $15\,\mathrm{dB_{Vrms}}$. The FFT approach is more robust and yields usable values down to $10\,\mathrm{dB_{Vrms}}$, with only 20% correctly detected phases remaining. Acquiring the phase data by using the correct constant frequency bin improves the breakdown SNR for all algorithms by at least 10 dB, with no detection breakdown at all for the FFT-based estimation on the synthetic data!

For the synthetic phase data, the dependence of the estimated frequency accuracy on the length L and subsampling factor S of the phase sequence is investigated. The results are needed for the parameter determination of phase-sensitive measurements, specifically of the number L_D of different delays at which the phases are measured and the delay time increment $\Delta t_D = S\Delta t_{\mathrm{synthetic}}$ between the measured phases. As determined in Fig. 3.12, the frequency estimation accuracy scales inversely with $U_{\mathrm{signal,pp}}/U_{\mathrm{noise,pp}}$ down to the breakdown SNR, after which the algorithm fails. Thus, an SNR invariant normalized estimation error $\Delta f_{\mathrm{norm}} = U_{\mathrm{signal,pp}}/U_{\mathrm{noise,pp}}\,\Delta f$ can be defined. In Fig. 3.13, this normalized error is calculated for all phase sequences with a full-sequence error below 10 mHz to remove results with breakdown effects. As the normalized errors scatter around $\Delta f_{\mathrm{norm}} = 0$ with an L and S (but not SNR) dependent accuracy, their standard deviation is taken to quantify their accuracy and plotted with respect to L and S.

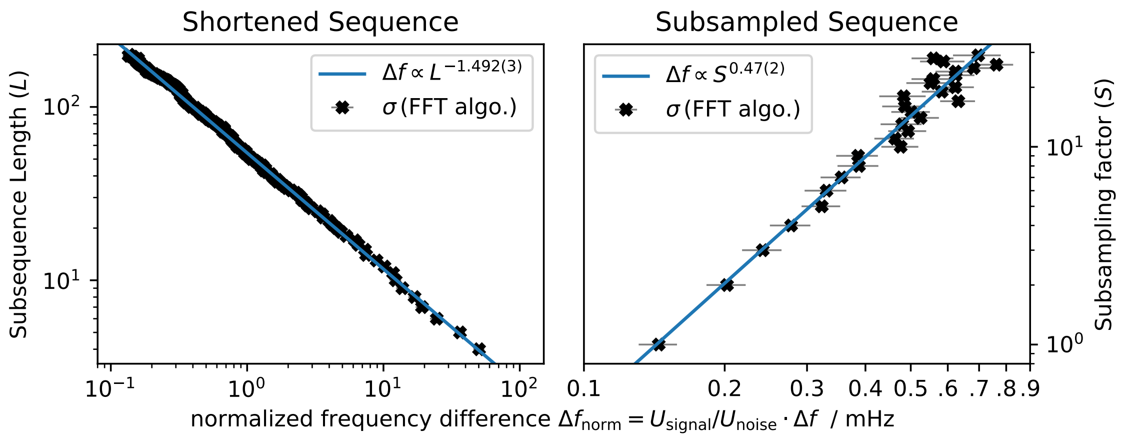

Figure 3.13: Normalized frequency estimation accuracies depend on the subsampling strength ($f_{\mathrm{init}} = 2102\,\mathrm{Hz}$) and subsequence length ($f_{\mathrm{init}} = 2120\,\mathrm{Hz}$). Increased subsampling or shortening both decrease the frequency precision, with different, but related scalings. All phase unwrapping algorithms yield very similar results, so the FFT estimation is used as a representative example.

The error scaling can be partially understood by examining the behaviour of the model phase-time sequence $(\varphi, t) = (k\Delta\varphi \pm \sigma, k\Delta t)_{k<N}$, where N is the length of the sequence, Δt and $\Delta\varphi$ are the underlying constant phase and time increments, and σ is a zero-mean random variable providing the phase scatter. Subsampling the sequence by S yields $\Phi_1 = (Sk\Delta\varphi \pm \sigma, Sk\Delta t)_{k<N/S}$, while shortening it to the first $L =: N\big/S$ points yields $\Phi_2 = (k\Delta\varphi \pm \sigma, k\Delta t)_{k<N/S}$. Scaling Φ_2 up by a factor of S does not change the estimation error and results in $(Sk\Delta\varphi \pm S\sigma, Sk\Delta t)_{k<N/S}$, which is equivalent to Φ_1 with the σ scaled up by S. The estimation error scales linearly with σ, and thus the frequency estimation error of the shortened sequence is S times larger than that of the subsampled sequence. Assuming that the subsampling frequency precision scales with S as a power law $\Delta f \propto S^{\xi}$ with exponent xi, this means the shortened subsequence scales with L as $\Delta f \propto S \cdot S^{\xi} = S^{1+\xi} = L^{-1-\xi}$. Approximating the initial sequence as groups of n phases with the same reference times, the standard deviation of their mean is $\sigma\big/\sqrt{n}$ and subsampling by S increases Δf by a factor of $S^{1/2}$, so $\xi \approx \frac{1}{2}$. With $\xi = 0.491(3) \approx \frac{1}{2}$, the fitted error scalings from Fig. 3.13 are obtained. Thus $\Delta f(L_D, \Delta t_D) \propto L_D^{-3/2} \Delta t_D^{-1}$. However, higher Δt_D need more precise initial frequency guesses as the frequency span between harmonics decreases.

4 Setup Implementation and Experimental Results

This chapter details how phase-sensitive modified cyclotron frequency measurements (phase methods, PM) were implemented in the BASE experiment during this thesis. The ordering of the sections is roughly chronological; starting with antiproton catching and the initial state of the experiment, followed by the conceptual and electrical implementation of the phase method setup, and concluding with the first results, the optimization of the measurement parameters, and a note on axial frequency phase methods and their use in spin state detection. Relevant emergent issues and their resolutions during the deployment of the experimental setup are outlined as a reference for future PM experiments. By the end of this thesis, the developed method achieved a PM frequency uncertainty lower than that of alternative methods under similar suboptimal conditions of an actively cycling decelerator (AD on), although still above the optimum values achieved by these methods under the ideal conditions (AD off) used in the published antiproton g-factor and charge-to-mass ratio measurements [5, 6, 54].

4.1 Antiproton Catching Inside the BASE Experiment

The European Organization for Nuclear Research (CERN) together with its users is currently the only entity able to produce, decelerate and subsequently trap baryonic antimatter on Earth. Any antimatter experiments working with trapped antiprotons are thus necessarily based inside the antiproton decelerator hall, namely AEgIS, ALPHA, ASACUSA, GBAR, and BASE [117, 118, 119], until purpose-built apparati allow for the transportation of stored antimatter, namely BASE-STEP and PUMA [56, 120]. Hydrogen anions are accelerated and converted to 10^{15} protons at energies of 26 GeV in the first part of the LHC accelerator chain before being diverted into an iridium target, creat-

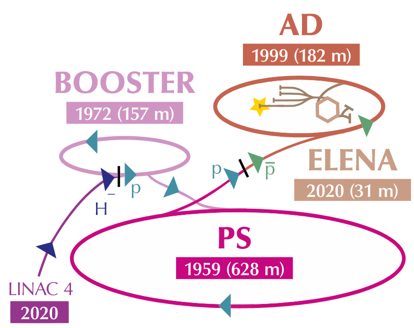

Figure 4.1: The acceleration and deceleration chain of the antiprotons and their precursors up to the BASE experiment [116].

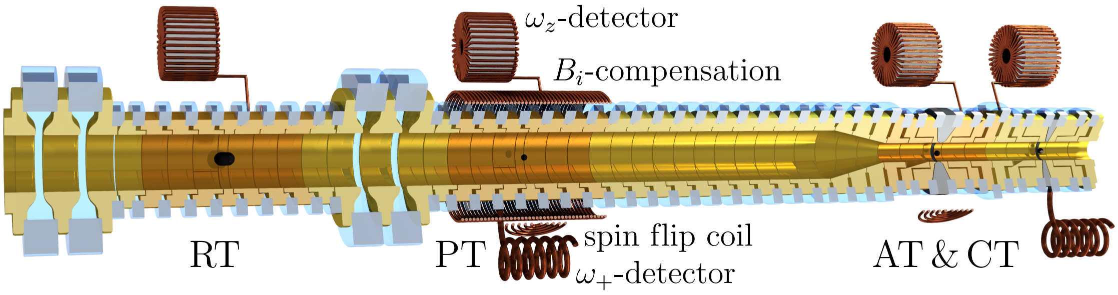

Figure 4.2: The BASE Penning trap assembly is created from a stack of 4 cylindrical Penning traps specialized for different purposes [54]. From left to right, they are designated as the reservoir trap (RT), precision trap (PT), analysis trap (AT) and cooling trap (CT). The RT is encased by two high-voltage electrodes with increased electrode spacing, used for catching hot antiprotons injected from the AD/ELENA facility.

ing about $5 \cdot 10^7$ catchable antiprotons amid a variety of energetic and exotic particles [27]. The antiprotons are subsequently slowed in the antiproton decelerator and ELENA until they reach an energy of about 100 keV, at which point they are transferred into the experiments listed above in four quasi-synchronous bunches of $7 \cdot 10^6$ particles [121]. An illustration of the taken path through the accelaerator complex is given in Fig. 4.1.

The BASE experiment slows the antiprotons down further by letting them penetrate an ultra-thin polymer foil, causing coulomb and nuclear scattering and broadening their velocity distribution while also separating the experiment vacuum from the beam vacuum [122]. The antiprotons then enter the trap stack in Fig. 4.2 from the left side, guided by the magnetic field lines of the superconducting Penning-trap magnet. After the low-energy tail reaches the RT, the two high-voltage electrodes are ramped up, trapping some of the low-energy particles inside an electrostatic potential well while the rest annihilates with ordinary matter on the trap surfaces [123]. BASE only requires about ten antiprotons per year to run, making the degrader's high loss rate and the uncatchable wide tails of the resulting antiproton velocity distribution acceptable. The RT already contains low-energy electrons when the antiprotons are caught, which thermalize the antiprotons by coulomb collisions while simultaneously dissipating their energy via cyclotron radiation $6.2 \cdot 10^9$ times faster than the antiprotons of the same energy would [124], since

$$P_{\mathrm{Rad}}(e, \bar{p}) = \frac{q^2 \gamma_{e,\bar{p}}^4}{6\pi\varepsilon_0 c^3} a_{e,\bar{p}}^2 \qquad \Longrightarrow \qquad \frac{P_{\mathrm{Rad}}(e)}{P_{\mathrm{Rad}}(\bar{p})} = \frac{a_e^2}{a_{\bar{p}}^2} = \frac{\omega_e^4 r_e^2}{\omega_{\bar{p}}^4 r_{\bar{p}}^2} = \frac{m_{\bar{p}}^3}{m_e^3} = 1836.15^3\,. \tag{4.1}$$

As the axial and radial energy of the antiproton-electron cloud is dissipated, the cooling rate decreases exponentially, since $\Delta E = P_{\mathrm{Rad}} \propto a^2 \propto r^2 \propto E$, converging into the energy region in which the energy-dependent frequency shifts and inter-particle interaction effects decrease $\Delta\omega_z$ to less than a few resonator widths. The axial resonator can then be swept slowly over the possible axial frequency range, cooling the axial and radial modes still energetically coupled by the electrons to $T_{\bar{p}}$ as described in Section 2.3.3. To find the converged ω_z of the cold particles, a parametric drive with $\tilde{\omega} = 2\omega_z$ [125, 126] is swept over the possible axial frequency range as well, exciting the axial mode over a wider range than direct excitation at $\tilde{\omega} = \omega_z$ would [86], but over a much thinner range than the initial span of possible ω_z.

Within the reduced range of possible ω_z, a manual V_R sweep to move the particles over the reasonator and detect the particle dip of the trapped cloud becomes feasible. However, the particle cloud is still a mixture of electrons, antiprotons, hydrogen anions and even heavier anions, interfering with the pick-up of the detection circuitry and potentially Debye-shielding the antiprotons. Removing the contaminants allows the dip spectrum to be detected. Depending on the properties of the specific contaminant, one of three removal schemes is required [54], after which the antiproton cloud in the RT is finally thermally cold, pure, and ready to be split for the extraction of a single antiproton into any of the other traps:

Heavy anions have a charge-to-mass ratio at least a factor of 2 smaller than the antiproton. Thus, in the same trap, their ω_z/ω_c ratio is increased by a factor of at least $\sqrt{2}$ closer to instability, as shown in Fig. 2.3. Intermittently increasing Φ_2 makes all radial motions of the heavy anions temporarily unstable, removing them from the trap.

Electrons are the only negatively charged stable particles with a greater charge-to-mass ratio than the antiproton[1]. They can be removed from the trap by driving their axial mode to a high-energy state $E_{z,e}$ in which the axial frequency shifts too far down for further excitation and simultaneously ramping down the ring voltage so the potential well becomes shallower than $E_{z,e}/q$. Not confined anymore by the potential well, they leave the trap.

Hydrogen Anions are too close in mass to the antiprotons to ramp them out of the trap without the risk of losing antiprotons as well. They are driven in their modified cyclotron mode ω_{+,H^-} instead. The H^- modified cyclotron frequency $\omega_{+,H^-} \approx 2\pi\, 29.613\,\mathrm{MHz}$ (PT) decreases at large energies, not crossing $\omega_{+,\bar{p}} \approx 2\pi\, 29.645\,\mathrm{MHz}$ (PT), so a downwards sweeping drive can excite ω_{+,H^-} out of the trap without heating $\omega_{+,\bar{p}}$.

4.1.1 The Four BASE Traps

The reservoir trap (RT) is used exclusively to capture and store the antiproton cloud [123]. If any measurement particle is lost, a new antiproton can be separated and shuttled into the measurement traps by asymmetrically subdividing the Penning potential well [54]. With a particle usage on the order of 10 particles per year and an RT storage capacity on the order of 100 particles, BASE can technically be run for years with one single loading cycle, which enables the investigation of exotic particles like antiprotons without continuous connection to an accelerator in the first place. The RT is operated on its own uninterruptible power supply and control code, safeguarding the stored particles against any outside influences. The inner high-voltage electrode triplet can also be used to temporarily park a particle upstream of all other traps during measurements.

[1]Exotic particles like muons and hydrogen dianions with intermediate charge-to-mass ratios exist but decay on microsecond timescales or less [127, 128]. For protons, besides antimuons, the required zero-neutron helium or lithium isotopes are even more unstable.

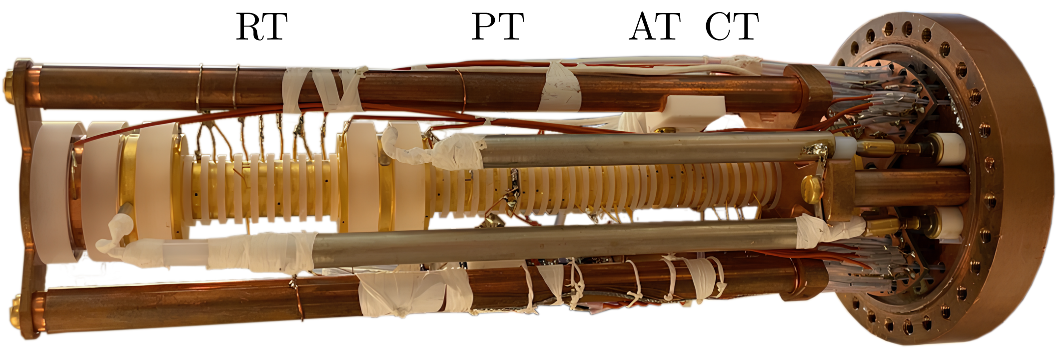

Figure 4.3: An image of the trap stack previously installed in the BASE experiment (taken from [87]). A schematic illustration of the trap stack cross-section is shown in Fig. 4.2.

The precision trap (PT) is used for the most precise and least systematically shifted frequency measurements of the antiproton. To this end, it is optimized to be orthogonal and compensated. Being the only large measurement trap, the optimization is able to be done more precisely. The PT is separated from the field inhomogeneities introduced by the CT and AT ring electrodes by a series of spacer electrodes used only for particle transport between the traps. It is surrounded by multiple superconducting coils to shield the trap centre from external magnetic field fluctuations and actively tune the B_0, B_1 and B_2 components of the axial magnetic field [68]. It is also connected to both axial and modified cyclotron detectors which can be used to measure ω_+ with the double dip and peak methods [6, 80]. The apparatus for phase-sensitive modified cyclotron frequency measurements is connected to the PT, and most results in this thesis refer to the PT.

The analysis trap (AT) is used mainly for the spin state initialization and detection of the antiproton during the BASE magnetic moment run. A "vacoflux 50" cobalt-iron alloy ring-electrode introduces a strong magnetic bottle, increasing the ω_z dependence on E_+ compared to the CT such that the continuous Stern-Gerlach-effect induced spin-state dependent energies can be resolved [5]. Like the PT, it allows thermal cooling of the particle's three modes, either via direct coupling to the detectors or via $\omega_z + \omega_-$ sideband coupling of the axial and magnetron modes.

The cooling trap (CT) is used to quickly subthermally cool the modified cyclotron mode of a trapped particle. A nickel ring-electrode introduces a moderate magnetic bottle and thus a ω_z dependence on E_+. E_+ is thermalized using the modified cyclotron detector before detuning it and measuring ω_z. The scheme is repeated to yield a shifted Boltzmann distribution in ω_z and is stopped when the measured ω_z is sufficiently close to the bottom edge of the distribution, corresponding to a modified cyclotron temperature of $0\,\mathrm{K}$ [54]. In the current experiment, problems with locating the particle's axial mode on the CT axial detector mean axial frequency measurements are done in the AT [129].

Beyond the CT, the trap stack is capped by the field emitter gun and its high-voltage biasing electrodes, used to introduce electrons for electron cooling and the creation of protons used during magnetic moment measurements [5, 130].

4.2 Phase Method Concept

To motivate the phase method concept, the current modified cyclotron frequency ω_+ measurement methods are quickly reviewed first.

Double-dip methods (Section 2.3.4) use the absence of the shorted resonator noise around the sidebands of ω_z to determine a double dip spectrum which can be fitted to obtain ω_+. Averaging N spectra decreases the spectrum's scatter by $1/\sqrt{N}$ with an equal effect on the uncertainty of ω_+. Since every spectrum takes the same time to acquire, the scaling of the frequency uncertainty with time is given by $\delta\omega_+ \propto 1/\sqrt{t}$. Increasing the acquisition time of one double-dip spectrum does not decrease the scatter of any bin in it. And averaging neighbouring bins causes the same scaling with time as averaging multiple spectra.

Direct Peak methods (Section 2.2.1) excite the modified cyclotron motion until it is visible as a peak in the spectrum of the detection signal. Fitting the shape of the peak using the correct window response yields ω_z to a higher precision than double dip methods but with systematic shifts due to the high particle energy. During detection, the particle's energy is dissipated and the signal strength decays, limiting the SNR of the acquired peak spectrum. As above, multiple peak spectra can be averaged, yielding the frequency uncertainty scaling of $\delta\omega_+ \propto 1/\sqrt{t}$.

If the modified cyclotron mode energy would not be dissipated during the acquisition of the detection signal, the peak spectrum could be acquired for an arbitrary amount of time, decreasing the peak width $\Delta\omega_+ \propto \omega_B \propto 1/t$ and thus frequency uncertainty with a scaling of $\delta\omega_+ \propto 1/t$ instead. Alternatively, the signal can be split into segments of constant length from which their initial phases are extracted. With correct unwrapping, the uncertainty scaling increases to $\delta\omega_+ \propto 1/t^{1.5}$ according to Fig. 3.13. For a constant amount of extracted phases, the scaling remains at $\delta\omega_+ \propto 1/t$. However, detection requires interaction, so such a signal is not possible. Instead, it can be stitched together by initializing the particle multiple times in the same state and waiting an increasing amount of evolution time until starting both the detection and acquisition of the particle signal. Three problems arise from this method:

First, repeating the initialization and detection sequence with an acquisition time T to acquire a total signal of length t requires t/T repetitions of increasing length, resulting in a total sequence duration proportional to t^2. The improved frequency uncertainty scaling of the full signal measurement with t is thus voided. By measuring only a constant number of segments, the total sequence time remains proportional to t and the uncertainty scaling of $\delta\omega_+ \propto 1/t$ persists. Since the time domain signal sections both still decay during the detection and do not connect anymore with only a constant amount taken, it also justifies the intermediate step of converting the signal to the initial segment phases before using those to estimate ω_+ via the algorithms described in Section 3.2.

Second, how does one initialize the particle in the same state multiple times? Revisiting Eq. (2.48), analogous to the axial mode, the modified cyclotron mode is excited by an external drive at ω_+, moving the motion away from the origin in the (x,y) phase space

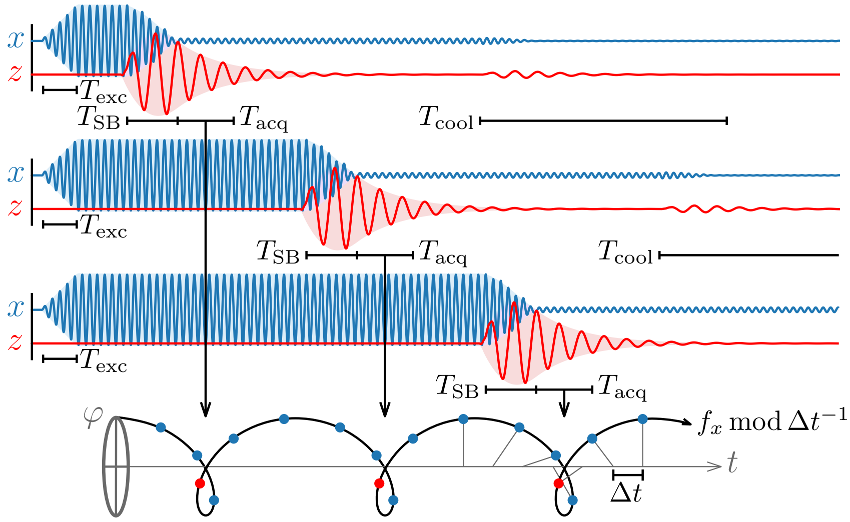

Figure 4.4: In a phase method frequency measurement, the (φ, t)-pairs used to estimate ω_+ are acquired according to the phase method sequence illustrated here and described in greater detail in the text. A cold particle gets initialized in a given state and is evolved for a varying amount of time before imprinting the modified cyclotron (x) phase onto the axial (z) phase and extracting it with a DFT of the detected signal. Unwrapping the acquired phases yields ω_z modulo ω_B.

while keeping its initial uncertainty constant. The resultant rice distribution with $\Lambda \propto t_{\text{exc}}$ and $\sigma \propto \sqrt{E_0}$ is thus maximally precise according to Eq. (3.7) for a long excitation time and a minimal initial energy of the modified cyclotron mode before excitation. Consequently, an excited state with a known phase can be recreated repeatedly by first cooling the particle down before reexciting it with the same drive at the same phase.

Third, how is the particle-detector interaction interrupted during the particle's evolution time? While not possible for the resonator as shown in Fig. 2.8, the actual implementation includes a varactor in the amplifier circuitry which can change the effective capacitance of the resonator, tuning its quality factor and resonance frequency $\tilde{\omega}$ [87, 131]. By detuning $\tilde{\omega}$ from ω_+, the particle-detector coupling is weakened depending on the detuning amount, easily allowing multiple seconds of evolution time without visible energy decay within the tuning limits of the varactor circuit. However, the varactor detuning is slow and the quality factor of the modified cyclotron resonator is quite low, necessitating an alternative detection method.

Exploiting the fact that any pulse of a sideband drive at $\tilde{\omega} = \omega_+ \pm \omega_z$ imprints phases between the axial and modified cyclotron modes, an axially cold particle can be used to transfer the modified cyclotron phase readout onto the axial mode so that the cyclotron detector can stay detuned. The timing sequence of such a scheme is shown in Fig. 4.4. Starting with a particle that is cold in both modes, the modified cyclotron mode is excited by an external drive, initializing the particle with a known initial energy and phase. After letting the modified cyclotron phase evolve for a time t, both modes are

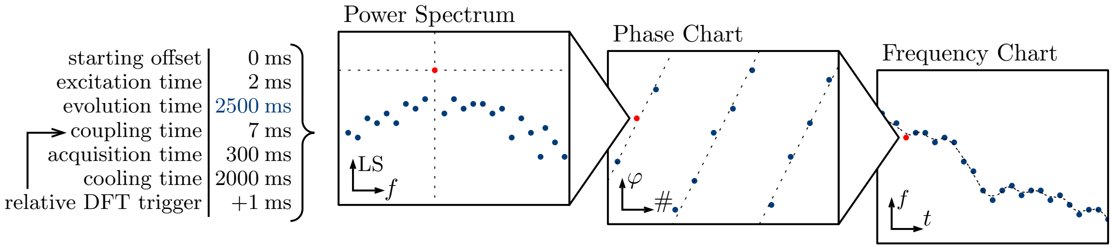

Figure 4.5: By iterating the PM sequence, the list of obtained power spectra yields a list of phases which in turn determine ω_+. Repetition of the whole estimation procedure provides a frequency history, from which ω_+ can be interpolated even at intermediate times.

coupled, transferring the energy and imprinting the phase from the modified cyclotron to the axial mode. Even during the energy transfer, the axial mode dissipates its energy and thus its phase information into the detection circuitry. To minimize artefacts from the detection of coupling drive sidebands, the DFT acquisition is started only after the coupling is finished and lasts until the optimal SNR is achieved (see Fig. 2.11). Measuring off-resonator or with active negative feedback cooling should improve the optimum SNR and has to be tested.

After the acquisition of the peak spectrum, the particle needs to be returned to its initial cool state. Depending on the coupling frequency used for imprinting the modified cyclotron phase, the modified cyclotron mode may contain residual energy after PnP coupling or is intentionally highly energetic after PnA coupling. The axial mode thermalizes quickly to $T_{\bar{p}}$, so the modified cyclotron mode is coupled on the lower sideband with a strongly attenuated drive for multiple Rabi periods such that it also thermalizes to $\frac{\omega_+}{\omega_z} T_{\bar{p}}$ according to Section 2.3.3. After sideband cooling, the particle can be reused for the next phase measurement.

Each iteration of the PM sequence yields a DFT spectrum, from which the signal bin phase can be obtained either by detecting the maximum power bin, or by prior knowledge of ω_z to a greater precision than one DFT bin width ω_B, so the signal bin can be unambiguously determined. Repeating the PM sequencer with varying evolution times gives a list of phases, which can be unwrapped to determine the current modified cyclotron frequency ω_+. Finally, as shown in Fig. 4.5, the repetition of the frequency estimation measurement provides a history of ω_+, which can be interpolated or modelled to determine ω_+ at any point in time, which is needed for the magnetic moment measurements, where modified cyclotron frequency data is only available when the spin-state resolved particle, for which ω_+ is to be determined, is not inside the trap.

4.2.1 Causes of Phase Uncertainty

Three sources of external influence will increase the variance of the PM particle's phase over one phase measurement. The cooled particle at the start of the sequence still has residual energy in the modified cyclotron mode, determined by the resonator temperature and the duration of sideband coupling. As the particle is initialized into its excited modified cyclotron state, the initial energy introduces uncertainty into both the excited energy and the excited initial phase according to Eq. (2.51) and Eq. (3.7). During the free oscillation in which the phase of the particle evolves as $\Delta\varphi \equiv \omega_+ t_{\mathrm{evo}} \pmod{2\pi}$, the drift of the magnetic field in turn causes a drift in ω_z and thus $\Delta\varphi$. Finally, the phase detection via a peak on top of the resonator and amplifier noise background introduces randomness into the acquired time domain signal, broadening the obtained phase distribution further.

The initialization and readout errors are similar in that an ideal system creates a state vector in $\mathbb{R}^2$ which is transformed into a distribution by a superimposed circular normal distribution from the source of uncertainty. For the initialization, the 2D space is (x, y) or $(\dot{x}, \dot{y})$ in which the normally distributed initial radial coordinate of the cyclotron state is shifted by the excitation drive, specified by Eq. (2.48). For the readout, it is the complex image of the acquired time domain signal DFT, where the noise background is normally distributed and the signal is a complex value proportional in amplitude to the modified cyclotron motion amplitude. In both cases, a Rice distribution with a respective phase uncertainty is created.

The phase error during evolution behaves differently. A changing magnetic field does not change the modified cyclotron amplitude. Instead, it slowly retards or advances the phase of the motion, azimuthally smearing the rice distribution. When using phase methods to determine ω_+, it is not even necessarily an error, since the introduced phase scatter represents the inherent scatter of ω_+. For example, when continuously monitoring ω_+ by a repeated block of averaged measurements in an otherwise ideal measurement without the error sources above, the phase scatter can be reduced by making any measurements inside a block shorter and repeating them more quickly so that only a small fraction of the time dedicated to each measurement block is used. But this is only the case because now $\omega_+(t)$ is only sampled from the first fraction of the block. Changes of ω_+ afterwards that cause the increase in scatter are simply not detected. Such a scheme is needed for the BASE magnetic moment measurements, and the optimizations for measuring $\langle\omega_+\rangle_{[i,i+1]}$ or $\omega_{+,i}$ differ.

In imperfect measurements of $\omega_+(t_{\mathrm{meas}})$, such schemes are required to average out the two other error contributions, and the variation of the magnetic field will present itself as another source of scatter in the determination of $B(t_{\mathrm{meas}})$. For increasing evolution times, $\langle\omega_+\rangle_{[0,t_{\mathrm{evo}}]} - \omega_+(0)$ and thus the detected frequency scatter both increase linearly due to the magnetic field drift. It is thus helpful during the PM optimization to consider first the time-independent scatter contributions by measuring at small t_{evo}, before extending the optimization to real measurement sequences.

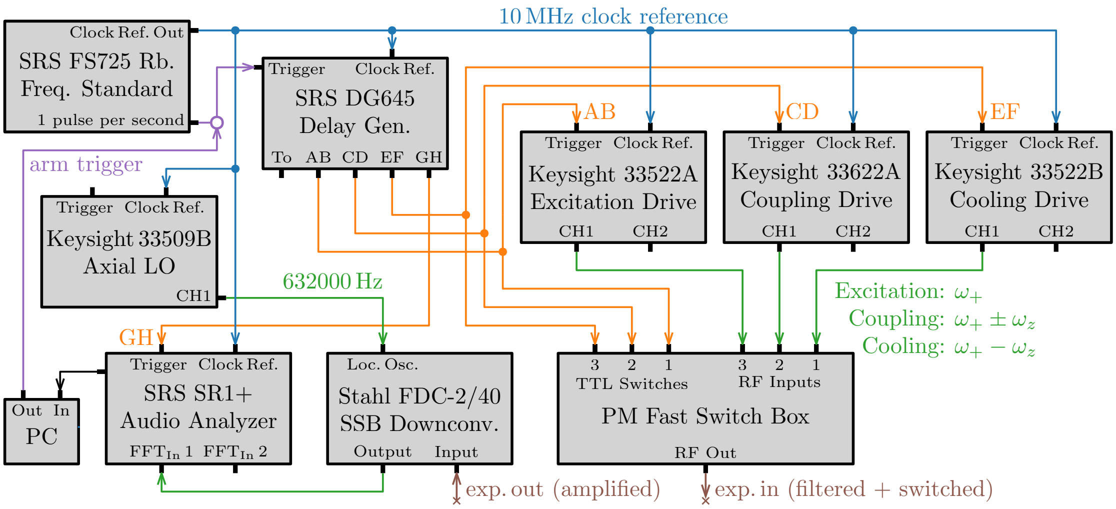

Figure 4.6: To obtain a PM measurement, the armed delay generator [142] is triggered by a 1 Hz pulse and initiates the excitation, coupling, and drive pulses by the respective drives [140]. After further signal attenuation and combination in the PM box [143], the merged output is switched into the general filtering stage and sent into the experiment (Fig. 4.7). Simultaneously, the output signal from Fig. 2.8 is downconverted [139] and forwarded to the triggered signal analyzer [138], returning the required power spectrum. All active components are synchronized through the blue line by a rubidium clock [141]. Logic signals travel through orange and purple lines, while analog signals do so through green and brown lines.

4.3 Phase Method Implementation

The BASE experiment has two electrical connections critical for PM measurements. First, the segmented PT correction electrode shown in Fig. 2.7 is accessible via a DC-decoupled radial excitation line labelled as PTER. By driving this line, the particle's motion and energy can be changed from the outside. The cold initialized particle can thus be both excited, sideband coupled, and cooled by successively driving the line at the required frequencies. Second, the PT axial detector signal freely is accessible, and using a power splitter [146], a fraction of the signal can be split off and used to acquire the necessary complex amplitude DFT spectra. However, when implementing the previously described PM sequence, some limitations of the used instruments illustrated in Fig. 4.6 need to be considered before measurements can begin.

The axial resonator signal at ω_z is of much higher frequency than the signal analyzer [138] is able to detect, and gets filtered by the built-in lowpass filters intended to avoid aliasing. Thus, the signal frequency needs to be reduced to be successfully analyzed. One option is exploiting the fact that a product of two sine waves is the sum of two sine waves at their sideband frequencies by multiplying the resonator signal with an external signal close to ω_z and filtering the upper sideband frequency with a lowpass filter to obtain a frequency reduced signal with half of the original SNR. This is called downmixing. Alternatively, the signal can be downconverted without any loss of SNR by self-interference of the phase-shifted mixed signal [139, 132], done so in the PM implementation. Somewhat problematically, the phase of the downconverted signal is dependent both on the detection signal phase and the reference drive (LO) phase. To guarantee the same phase relation in the output signal for multiple evolution times, the LO phase at the start of the signal acquisition needs to be constant. Bursting the reference drive relative to the DFT trigger is infeasible, as the burst transients affect the output signal of the downconverter for multiple seconds. Instead, the BASE PM implementation enforces that the evolution time of the particle is a multiple of the period corresponding to the reference frequency ω_{LO}. Since the PT axial frequency during the PM campaign was approximately 636 242 Hz, a value of $\omega_{\mathrm{LO}} = 2\pi\,632\,\mathrm{kHz}$ downconverts ω_z to less than 8 kHz while not downconverting the low-frequency tail to reflected negative frequencies. Furthermore, as 632 is a multiple of 8, all evolution time increments by multiples of $1/8000\,\mathrm{s} = 125\,\mu\mathrm{s}$ become permissible. The PM sequences as a whole are synchronized to the one-pulse-per-second rubidium clock pulse [141], so the use of integer frequencies for all drives makes them inherently phase-locked for equal PM sequences.

Another timing constraint is given by the SR1+ signal analyzer [138]. The FFT data acquisition runs on an internal 64 kHz clock, referenced to the 10 MHz reference signal of the rubidium clock. Triggering the SR1+ does not force the start of the data acquisition, instead only informing it that the next acquired data point at the next $1/64\,\mathrm{kHz} = 15.625\,\mu\mathrm{s}$ clock tick is to be used as the first point of the acquired spectrum. Thus, without knowledge of the internal clock state, the FFT triggering introduces 15.625 µs of timing uncertainty into the measurement. By timing the triggering to only change by multiples of 15.625 µs, the additional wait time after triggering stays constant, introducing only an irrelevant phase offset to the measurements. The 125 µs evolution time increment restriction synergizes with the 15.625 µs triggering time increment restriction, being chosen as its multiple. To simplify and standardize the PM sequencing, integer multiples of 125 µs are enforced for all sequence timings, visible in the figures contained in this chapter.

When originally implementing the signal combination using the PM fast switch box, it was assumed that the installed switching components [144] would attenuate the switched-off, 50 Ω terminated drive lines enough that the particle signal is not affected by them. However, the particle on the axial resonator is sensitive enough to be driven by the excitation-coupling sideband, regardless of its attenuation, even with an additional switch that should attenuate the already isolated sideband by another 70 dB. It is suspected that grounding issues limit the maximum achievable isolation to levels insufficient for phase methods, but the issue was not investigated further due to time constraints. Instead, the drives in the PM sequence are operated in a gated burst mode, triggered by the split TTL switching signal visible as the orange lines in Fig. 4.6.

Finally, care must be taken when updating the Agilent drives [140] in between PM sequences. If any parameter, even one without effect like the burst number in a gated drive is set to a different value, then the next time a variable with an effect on the drive

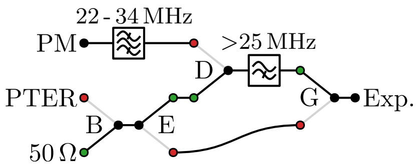

Figure 4.7: Using four of the RC-8SPDT-A18 switches [147] and further filters [148, 149], the PM and general PT radial excitation (PTER) lines are combined into the experiment's PT radial line. The PM input bandpass filter is characterized on the right.

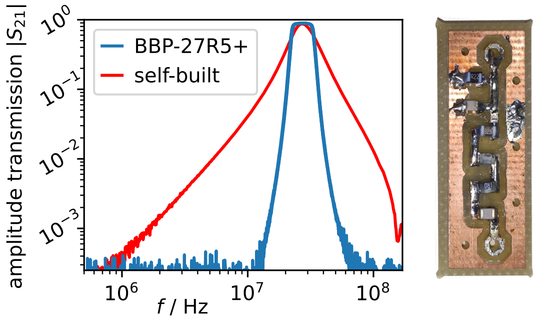

Figure 4.8: To transmit only a frequency band around ω_+, the PM input is filtered by a bandpass filter. Two types of filters were tested: A commercial MiniCircuits BBP-27R5+ [148] and a self-made bandpass at the same frequency, shown in the right image. The self-made bandpass has a worse falloff rate and is not used in the final PM setup.

output is set to any value, including the one it was already set to, the drive output after triggering will cut off for 1 to 2 ms before restarting with a different phase. Depending on the order of configuration commands, and if they are sent even for unchanged parameters, the drive can lag one PM sequence behind, introducing errors in the measurement data.

Having solved the above issues during implementation, the drive signal can be fed into the experiment. In the prior setup, the split PT radial excitation line is connected to a general-purpose radial drive via two different paths through a switch matrix, illustrated in Fig. 4.7. One of them, used for magnetron coupling, passes through the switch box unfiltered, while the other, used for cyclotron excitation and coupling, is additionally filtered by a highpass filter [149] to suppress any excitation of the axial and magnetron modes. Using an additional switch to splice the PM drive signal into the radial excitation line in front of the 25 MHz highpass filter, the PM drive signal can be used to drive the particle without changing the default behaviour of the PT radial drive circuitry while being filtered equally to the general purpose PT radial drive line. Specifically, the electrode remains connected to a 50 Ω termination in the default switch state.

The PM drive line is filtered further outside of its frequency range, since in contrast to the general-purpose drive line, its signal is expected to be switched quickly with significant transients, and any resultant power at the magnetron, axial, or Larmor frequencies should be suppressed. To this end, a third-order bandpass filter with approximately flat group delay is designed to attenuate anything outside the $[\omega_+ - \omega_z, \omega_+ + \omega_z]$ range without smearing the signal edges during switching. In parallel, a commercial higher-order bandpass filter [148] was also tested, with the transmission curves shown in Fig. 4.8. The additional smearing of the transmitted signal through the commercial bandpass filter is negligible even against the shortest 125 µs pulses, so it was chosen for installation into the PM switching setup due to its better falloff characteristics.

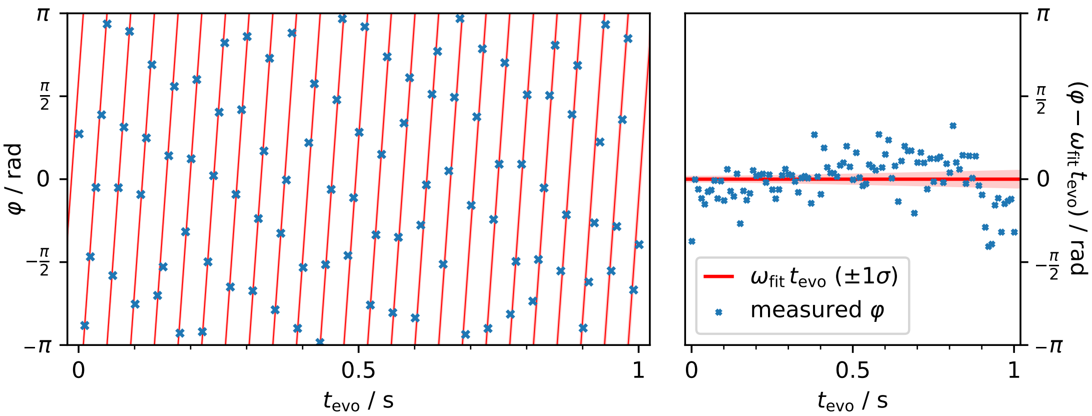

Figure 4.9: The first successful phase sensitive frequency estimation measurement, on the 25th of June, 2024, was done with 100 evolution time increments of 10 ms each, giving an estimated frequency $\omega_+/2\pi = 23.64(3)\,\mathrm{Hz}$ with a frequency aliasing width of 100 Hz. The precision of the unoptimized measurement comes at the cost of a long measurement time of approximately $100 \cdot 6\,\mathrm{s} \approx 10\,\mathrm{min}$. In the plot of the residuals shown on the right, a slow background drift of the modified cyclotron frequency caused by the magnetic field drift is already visible as a time-dependent systematic shift of the measured phases against the expected phase.

Returning finally to the general timing of the repeated PM sequence, all time-insensitive initialization and update steps of the sequence are done ahead of time by the experiment PC, after which it sends a trigger command arming the delay generator [142] to trigger on the next received 1 Hz clock pulse. The delay generator then coordinates all steps of the PM sequence, triggering the drive pulsed and the DFT acquisition, after which it signals a service request [133] to the PC, which receives the DFT spectrum and arms the delay generator for the next PM sequence.

Repeating the sequence with successive evolution time increments, unwrapping the measured phases, fitting the slope, and choosing the correct aliasing frequency yields the first working phase sensitive frequency estimation shown in Fig. 4.9. The fitted phase slope provides an aliased frequency estimate of $\omega_+ \equiv 23.64(3)\,\mathrm{Hz} \pmod{100\,\mathrm{Hz}}$. To be able to excite the particle's modified cyclotron mode, a prior estimation of $\omega_+ = 29\,645\,423(1)\,\mathrm{Hz}$ was obtained using double dip methods, giving a total frequency estimation of $\omega_+ = 29\,645\,423.64(3)\,\mathrm{Hz}$ with great confidence in the unaliased frequency choice when combining both estimations. As the PM measurements get optimized, this confidence will be reduced in favour of quicker and more precise measurements. The measurement was performed at a working point optimized for general measurements inside the PT. The challenge for the remaining chapters and months of the thesis past the 25th of June will be optimizing the measurement and trap parameters to achieve the highest frequency precision per total measurement time.

4.4 Phase Method Optimization

To quantify the conditions of the measurements, the magnetic field during the phase method campaign is characterized first, yielding the particle's energy scaling as well. Afterwards, the Rabi frequency of the coupling drive is determined, yielding the length and scaling of the required π-pulses. With the prerequisite measurements finished, the PnP measurement is optimized regarding TR, excitation energy, DFT acquisition parameters and resonator detuning before repeating the same optimization with PnA measurements. The results of the two separate optimizations are presented here in a combined form, sometimes using direct axial excitation as a proxy for axial mode excitation through coupling the modified cyclotron mode in measurements where the phase evolution and type of axial excitation is unimportant, e.g. axial decay durations.

4.4.1 B1 Determination

To first order, changes of the magnetic field along the z-axis are characterized by the linear relation $\Delta B_z = B_1\,\Delta z$. Since the cyclotron frequency $\omega_c = \frac{q}{m}B_z$ is proportional to B_z, changes to ω_c will be proportional to ΔB_z.

$$\Delta\omega_c = \omega_c(\Delta z) - \omega_{c,0} = \frac{q}{m}(B_0 + \Delta B_z) - \frac{q}{m}B_0 = \frac{q}{m}B_1\,\Delta z \tag{4.2}$$

The axial shift of the particle inside the trap is achieved by applying an offset voltage V_{P4} to the P4 electrode of the PT shown in Fig. 2.5, making the trap asymmetrical and moving the trap centre towards P4. With given trap parameters, the shift Δz of the trap centre depending on V_{P4} can be calculated analytically and specified to the first order by a constant $\eta \coloneqq \Delta z \big/ V_{\mathrm{P4}}$. The total modified cyclotron frequency scaling with Δz can then be determined by sweeping the particle over multiple V_{P4} and calculating ω_c via the invariance theorem (2.12) from the measured frequencies ω_+, ω_z, and ω_-. Fitting the slope $\xi \coloneqq \Delta\omega_c \big/ V_{\mathrm{P4}}$, then allows calculating B_1 as

$$B_1 = \frac{m}{q}\frac{\Delta\omega_c}{\Delta z} = \frac{m}{q}\frac{\Delta\omega_c}{V_{\mathrm{P4}}}\frac{V_{\mathrm{P4}}}{\Delta z} = \frac{m}{q}\frac{\eta}{\xi} = 11.2(3)\,\mathrm{mT/m}\,, \tag{4.3}$$

where $\xi = 658(6)\,\mathrm{Hz/V}$ is the result of fitting the measurements shown in Fig. 4.10 and $\eta = 612.4 \cdot 10^{-6}\,\mathrm{m/V}$ is numerically determined from the electrode potentials. Values for proton and antiproton $\frac{m}{q}$ are known to great precision by prior measurements [6].

4.4.2 B2 Determination

To second order, both B_1 and B_2 determine the frequency scaling described above, and ξ needs to be fitted by a quadratic equation. However, as can be seen in Fig. 4.10, the quadratic effect is small. It is roughly equal to the other uncertainties, increasing the uncertainty of B_1 from $0.1\,\mathrm{mT/m}$ to the stated $0.3\,\mathrm{mT/m}$.

To determine B_2, the particle is radially excited in the modified cyclotron mode to sample regions of the trap with an increased B_2 effect. Intuitively, if the axial source

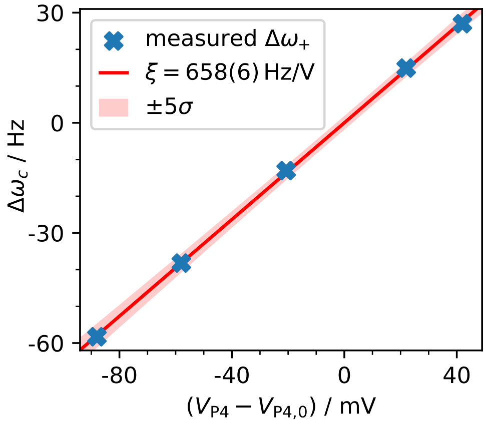

Figure 4.10: Determining B_1 requires fitting the slope of the modified cyclotron peak frequency shift $\Delta\omega_+$ against the offset voltage V_{P4}.

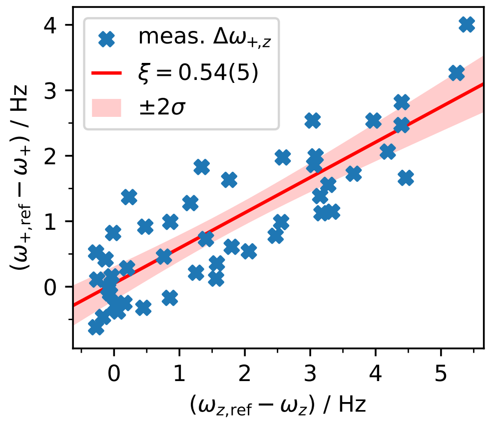

Figure 4.11: Determining B_2 requires fitting the slope of the modified cyclotron peak frequency shift $\Delta\omega_+$ against the axial dip frequency shift $\Delta\omega_z$.

free magnetic field increases quadratically with B_2 in the axial direction, it needs to quadratically decrease with $\frac{1}{2}B_2$ in the radial direction so that it fulfils the Laplace equation $\Delta \cdot \vec{B} = 0$. The superimposed axial oscillation on the scaled modified cyclotron motion then also samples other points in the electrostatic potential well, shifting its frequency, too. Equivalent to Section 5.3.1, the value of B_2 can then be determined by the shifts of the axial and modified cyclotron frequencies, acquired by dip and peak spectra, respectively. Ignoring higher-order contributions than B_2 and C_4 and assuming a symmetrical trap, they are given by the following equations taken from [6].

$$\Delta\omega_+ = \omega_+\left(-\frac{1}{mc^2} - \frac{1}{m\omega_z^2}\left(\frac{B_1}{B_0}\right)^2 - \frac{1}{m\omega_z^2}\frac{B_2}{B_0}\left(\frac{\omega_z}{\omega_+}\right)^2 + \frac{3}{4}\frac{C_2}{q\Phi_2}\frac{C_4}{C_2^2}\left(\frac{\omega_z}{\omega_+}\right)^4\right)E_+ \tag{4.4}$$

$$\Delta\omega_z = \omega_z\left(-\frac{1}{2mc^2} + \frac{1}{m\omega_z^2}\frac{B_2}{B_0} + \frac{3}{2}\frac{C_2}{q\Phi_2}\frac{C_4}{C_2^2}\left(\frac{\omega_z}{\omega_+}\right)^2\right)E_+ \tag{4.5}$$

Plotting $\Delta\omega_+$ against $\Delta\omega_z$, as done in Fig. 4.11, the slope $\xi := \frac{\Delta\omega_+}{\Delta\omega_z}$ or its inverse can be obtained by fitting a straight line to data. Dividing Eq. (4.5) by Eq. (4.4) allows rearranging the resulting equation into the form $B_2(\frac{\Delta\omega_+}{\Delta\omega_z}, B_0, B_1, \ldots)$ given below, such that B_2 can be calculated from a measured value of ξ. Given that the B_i determination measurements were done in a compensated working point, it is asserted that $C_4 = 0$, and the C_4 term is neglected.

$$B_2 = \frac{1}{c^2}\frac{\omega_+}{\omega_z}\frac{\frac{1}{2}\omega_z^3 - \frac{\omega_+}{\xi}\left(\frac{B_1^2}{B_0^2}c^2 + \omega_z^2\right)}{\omega_+ + \frac{\omega_z}{\xi}}B_0 = -34.1(3.0)\,\mathrm{mT/m^2}\,, \tag{4.6}$$

where $\xi = 0.54(5)\,\mathrm{Hz/Hz}$, $\omega_z = 2\pi \cdot 636.2\,\mathrm{kHz}$, $\omega_+ = 2\pi \cdot 29.65\,\mathrm{MHz}$, $B_0 = 1.945\,\mathrm{T}$, and the value for B_1 is taken from Eq. (4.3).

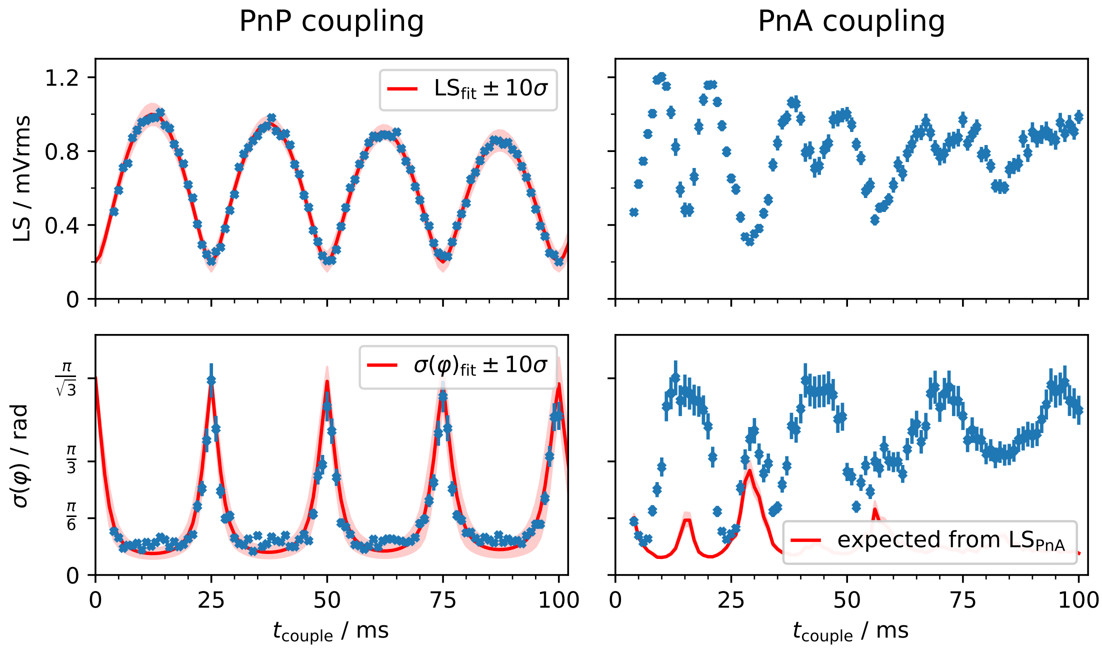

Figure 4.12: The Rabi resonances on the lower sideband are well-behaved and can be described by the mode coupling theory. From the Rabi frequency of $\Omega = 40.05(3)\,\mathrm{Hz}$ at $P_{exc} = 7.5\,\mathrm{dB_m}$, the optimal working point at $t_{couple} = 12.48(1)\,\mathrm{ms}$ can be determined. On the contrary, upper-sideband Rabi resonances are not understood. Amplitude and phase scatter measurements are periodic with one Rabi period with increased noise contributions, maximizing LS after 10 ms, whereas the mode coupling model would predict a single LS peak before a loss of signal due to the high-energy frequency shifts. Calculating the expected phase scatter from the amplitude signal assuming equivalent LS noise as when coupling on the lower sideband shows that the amplitude is only dominated by the true signal when $t_{couple} \leqslant 6\,\mathrm{ms}$ or one Rabi period later. The PnA working point at $t_{couple} = 6\,\mathrm{ms}$ is thus much more sensitive than the PnP working point. Both methods reach comparable optimum phase scatters of $\pi/12$ over a wide range of P_{exc}.

4.4.3 Rabi Oscillations

Next, the Rabi resonance needs to be characterized so that optimal working points for the PnP and PnA measurements can be found. For PnP measurements, it can be determined directly from a measurement of the linear Rabi frequency $2\pi f_\Omega := \Omega$ at given drive parameters, with a π-pulse achieved at a coupling time of $\pi/\Omega = 2/f_\Omega$. A Rabi frequency measurement using the inter-dip spacing in a double-dip spectra with a coupling drive power of $0\,\mathrm{dB_m}$ yields $f_\Omega \approx 12.9(3)\,\mathrm{Hz}$. As the Rabi frequency scales as the square root of the coupling drive power according to Eq. (2.59), this corresponds to a Rabi frequency of $40.8(1.0)\,\mathrm{Hz}$ at the chosen drive power of $10\,\mathrm{dB_m}$, without any change in optimum phase scatter. For PnA measurements, the scaling is not clear. Qualitatively, the phase scatter will decrease with increasing coupling times and peak powers until the frequency shifts increase enough for the peak to drift during the acquisition time, increasing phase scatter due to the increased energy-dependence (Section 2.2.1).

Taking the expected 40 Hz Rabi frequency as a reference, coupling times up to 100 ms are tested to include multiple Rabi periods in the acquired evaluation dataset shown in Fig. 4.12. In the PnP dataset, 4 periods are clearly visible. Surprisingly, they are visible even in the PnA dataset, which also includes amplitude minima at half-Rabi periods. Modelling the PnP amplitude as an exponentially decaying absolute sine wave

$$\mathrm{LS}(t_{\mathrm{couple}}) = \sqrt{\left(\mathrm{LS}_0 \left|\sin\left(\pi \frac{t_{\mathrm{couple}}}{\tau_\Omega}\right)\right| e^{-\frac{t_{\mathrm{couple}}}{\tau_A}}\right)^2 + \frac{\pi}{2}\,\mathrm{LS}_{\mathrm{N}}^2} \tag{4.7}$$

with Rabi period $\tau_\Omega = 24.97(2)$ ms ($f_\Omega = 40.05(3)$ Hz), initial envelope linear spectrum $\mathrm{LS}_0 = 1.006(8)\,\mathrm{mV_{rms}}$, amplitude decay time $\tau_A = 470(30)$ ms and an RMS additive noise floor $\mathrm{LS_N} = 0.159(4)\,\mathrm{mV_{rms}}$ provides the optimum agreement with the peak data under the chosen model of a mode coupled on the lower sideband with simultaneous slow cooling on the resonator and measured by noise-contaminated detection circuitry. The two measured Rabi frequencies agree, while τ_A is increased significantly from its reference value of $2 \cdot 90$ ms given in Section 2.2.1 due to the partial energy storage in the non-decaying modified cyclotron mode during coupling. The reduced amplitude value with its noise floor removed can now be used to calculate the phase scatter using Eq. (3.7) with a Rice distribution mean of $\Lambda = \mathrm{LS}(t_{\mathrm{couple}})$ and a fitted standard deviation $\sigma = 0.189(4)\,\mathrm{mV_{rms}}$. Neither σ nor $\mathrm{LS_N}$ change between the PnA and PnP measurements. Thus, the reduced PnA amplitude value can be used to predict the measured PnA phase scatter under the assumption that the signal is not otherwise contaminated, yielding the red line in the bottom right plot of Fig. 4.12. The prediction only agrees in the first 6 ms and again after about one Rabi period. The optimum working point is included in the range, at the last measured coupling time before the assumptions break down and increase the phase scatter significantly. The cause of the Rabi periodicity in amplitude and the second-order peak minima was not investigated further due to time constraints and remains unknown.

To gain further understanding of the PnA behaviour, it was also tested if its apparent Rabi periodicity scales with the square root of the coupling drive power according to Eq. (2.59); something already known for lower sideband Pnp coupling and expected for PnA coupling as well. The results of the coupling time scans at different coupling powers between 6 and 20 $\mathrm{dB_m}$ are illustrated in Fig. 4.13 and normalized relative to the expected Rabi period at the respective coupling power. Around 18 $\mathrm{dB_m}$, f_Ω increases more slowly than expected by the $f_\Omega \propto \sqrt{P_{\mathrm{couple}}}$ scaling, hinting at nonlinearities in the PM PTER line connecting the radial drive with the PT P4 electrode. At an absolute Rabi period of around $T_\Omega(20\,\mathrm{dB_m}) = 8\,\mathrm{ms} \approx 250000$ bursts, effects of the rotating wave approximation are still negligible. Below 18 $\mathrm{dB_m}$, f_Ω scales as expected and can thus be driven by a wide range of coupling powers.

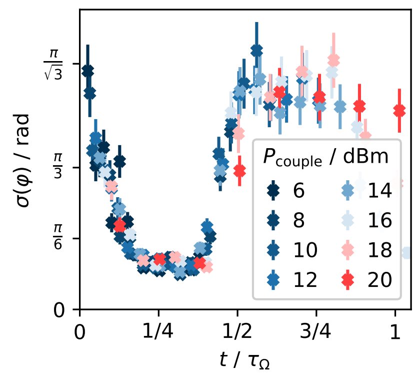

Figure 4.13: For high coupling powers, f_Ω is smaller than expected.

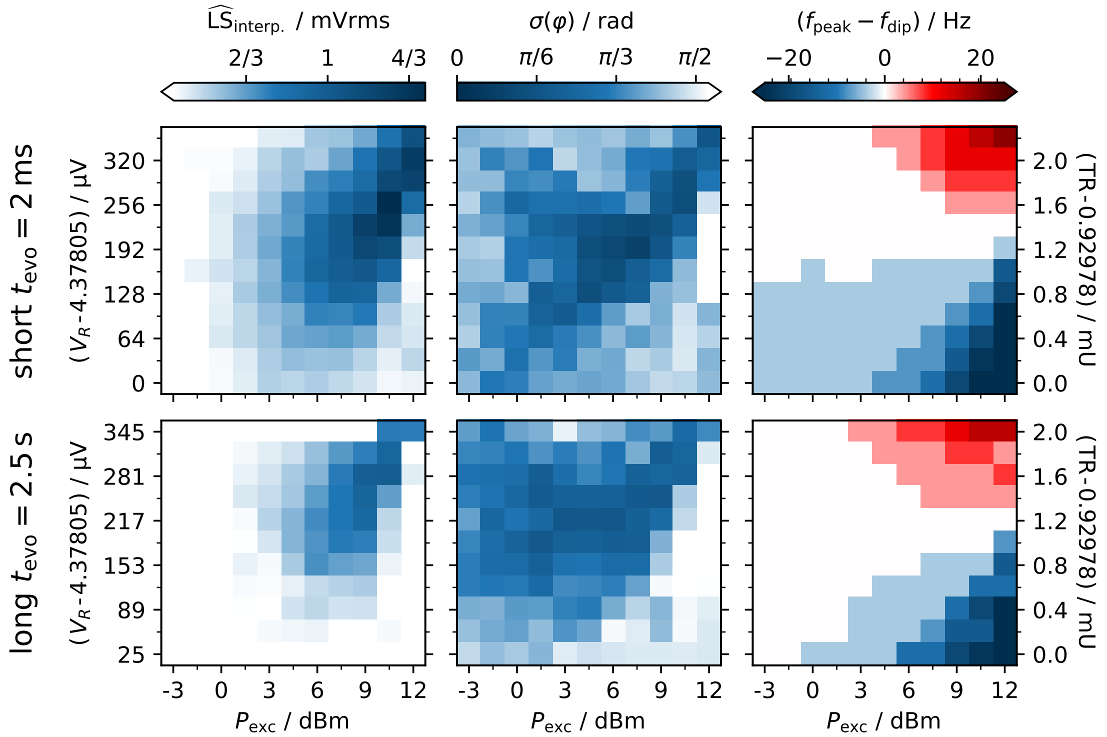

Figure 4.14: The initial optimization of the t_{evo} and P_{exc} working point provides an island of phase-stability for the PnP measurement scheme, where phase scatters $\sigma(\varphi)$ of less than $\pi/5$ can be achieved, even at long evolution times of multiple seconds. A diminishing peak SNR limits the island on one side, and stronger peak frequency drifts on the other.

4.4.4 Tuning Ratio and Excitation Power Optimization

The first trap parameters to be actively optimized are the excitation drive power P_{exc} and the evolution time t_{evo}. Regardless of the sideband coupling type of the measurements, the resultant measurement characteristics of the axially excited particle should be similar, so the optimization measurements were only performed using the PnP scheme. Referencing Fig. 4.14, the parameter region in which the peak SNR is optimized was found inside the 2D scan at around $V_R = 4.3783\,\mathrm{V}$, $\mathrm{TR} = 0.9314$, and $P_{\mathrm{exc}} = 10\,\mathrm{dB_m}$, where the excitation time is kept fixed at 2 ms. Low excitation drive powers decrease the height of the peak in the linear spectrum, decreasing the SNR, whereas great excitation powers excite the particle until its frequency shift is large enough to smear the peak signal over multiple bins. In unoptimized (V_R, TR) points, the higher-order electrostatic potential coefficients are large enough to cause frequency shifts even at low modified cyclotron energies. Moving on to the phase scatter, the optimum is shifted towards lower excitation energies. Even if the signal remains mostly in one bin, the shift inside the bin can already be large enough to decrease phase stability. Furthermore, higher excitation energies have a greater energy scatter, and thus also a greater phase scatter. Especially in the short evolution time case, an indent of phase instability at $P_{\mathrm{exc}} \approx -1\,\mathrm{dB_m}$ is

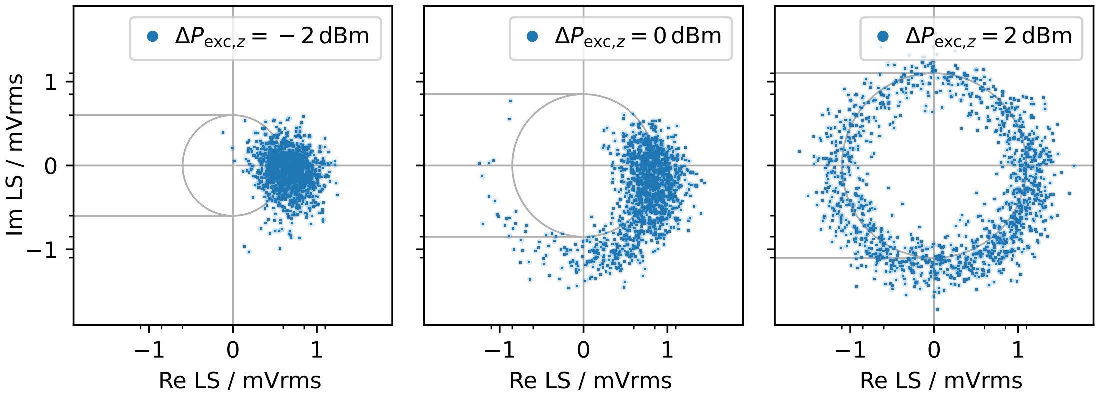

Figure 4.15: Small variations in the initial axial particle energy can have large effects on the resulting phase scatter. Optimizing the PT TR should minimise the phase scatter at a constant initial axial energy, shortening the high-energy phase tails. The particle was excited for $t_{\mathrm{exc}} = 0.5\,\mathrm{ms}$ with a reference drive power of $P_{\mathrm{exc},z,0} = -36\,\mathrm{dB_m}$.

visible in the top middle plot of Fig. 4.14. This is an artefact of the DFT bins. At those parameters, the peak is in between two bins, of which only one is used, artificially increasing the phase scatter. For the peak LS plot, a sinc is fitted to the 2 maximum power bins and the top value of the fitted sinc is illustrated, removing the indent. By tuning the peak signal to always lie centred on a bin, it is assumed that the indent in the phase scatter plot would also disappear.

4.4.5 Axial Phase Distributions

An alternative approach for tuning ratio optimizations can be given by minimizing the phase scatter from an axially initialized particle. After the particle is excited in its axial mode, an unoptimized TR introduces anharmonicity like C8 (Section 2.2.1) into the electrostatic potential, making ω_z frequency dependent and thus increasing the phase scatter for repeated measurements with a particle at different excited energies (Section 2.2.1). By initializing the particle in an excited axial state, the additional phase scatter from modified cyclotron initialization, phase evolution and mode coupling can be removed, and the scope of the investigation can be reduced to only axial TR effects.

Figure 4.15 shows how the phase distributions change for increasing axial energies at a constant TR. In the critical region of increasing phase scatter, where the distribution morphs from Rician to uniformly distributed in phase, the distribution develops a one-sided tail whose length depends on the initial axial energy and the value of the inhomogeneous terms (C_4 and up) of the electrostatic potential. Equivalent to Eq. (2.38), these terms introduce a power-law scaling of the frequency shift with the axial energy. With the particle's energy approximately symmetrically distributed around its expected axial energy $E_{z,*}$, the high-energy tail of the frequency-shift distribution, and thus phase distribution is generally scaled more due to the greater derivative of the power-law scaling at greater energies. The greater the value of $E_{z,*}$ and the width of the energy distribution, the stronger the effect will be. Tuning TR to minimize the tail phase distribution in turn also minimizes trap inhomogeneities at the relevant axial energy range. Since direct axial excitation was implemented only after the PM optimization run, it has not been used to optimize the TR in this thesis, and is provided here as a reference for future measurement campaigns. Furthermore, the axial optimization effects need to be assessed together with the effects on modified cyclotron initialization scatter, as changes to the electrostatic inhomogeneities also effect the particle's radial mode behaviour. And with neither of the motions constrained only to the trap centre, a perfectly harmonic motion can never be achieved. This is also the reason why the optimized TR working point for PM measurements differs from the corresponding working point for dip methods.

4.4.6 Off-Resonator and Feedback Measurements

As briefly discussed in Section 2.2.1, the relative strengths of the peak signal and the noise background are expected to stay constant when detuning the resonator, with both of them proportional to $|Z_p|$. With the weaker coupling of the particle to the detuned resonator, its amplitude decay time τ_A increases together with the optimum acquisition time $1.25\tau_A$, increasing the optimum SNR of the peak spectrum. Since phase scatter is strongly dependent on the peak spectrum SNR, it should increase as well when detuning the resonator. The above reasoning ignores the amplifier noise, which is frequency-independent in the axial frequency range and has no effect on the axial signal strength. It limits the validity of the argument for large detunings, where the resonator's Johnson-Nyquist noise becomes comparable to the amplifier noise, and the peak SNR decreases, even for increased acquisition times. An optimum is thus to be found at some intermediate value of the detuning frequency. Alternatively, the particle-resonator coupling can be weakened by radiating the feedback signal described in Section 2.2.2 into the detection circuitry such that it destructively interferes with the noise and reduces its effect on the particle [95, 96]. Feedback switching is fast compared to resonator tuning and is thus preferred in direct axial phase methods.

Again, the measurements are done using direct axial excitation after the finished PM optimization, with the main problem that in equal PM sequences, weakly coupled particles are excited to lower energies. Still, improvements for both detuned and feedbacked resonators can be seen even with the less energetic particles. The measurement in Fig. 4.16 has problems with axial overexcitation on the tuned resonator increasing the centred phase scatter, and the particle not being centred on a bin, especially at $\Delta f_{\mathrm{Res}} = -108\,\mathrm{Hz}$. Nonetheless, it can be seen that off-resonator measurements increase the Peak SNR for long acquisition times. With $256\,\mathrm{ms} \approx 1.25 \cdot 2 \cdot 90\,\mathrm{ms}$ being approximately optimal for on-

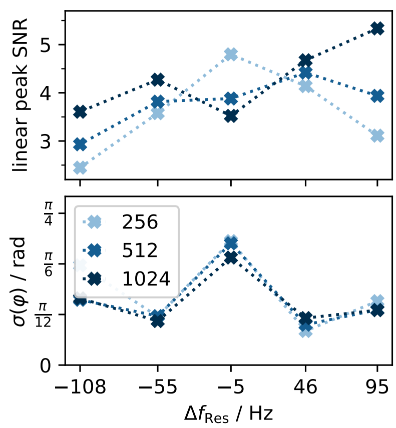

Figure 4.16: Detuning and long acquisition times improve SNR and potentially phase scatter.

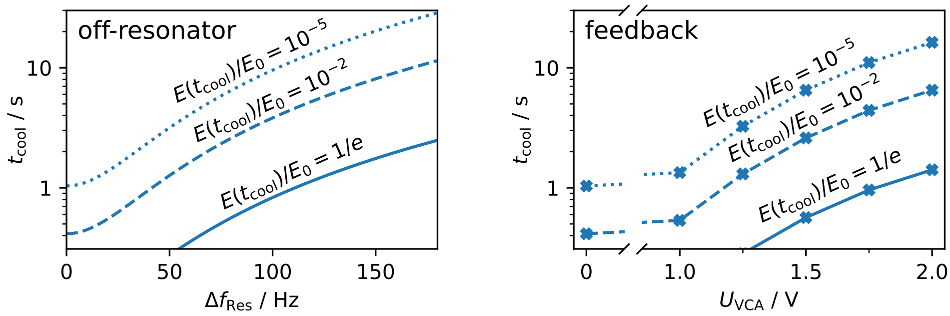

Figure 4.17: Necessary sideband cooling times quickly increase for off-resonator measurements (left) and measurements with active negative feedback (right). With particle energies on the order of 1 eV when excited, and $10\,\mathrm{K} \approx 10^{-3}\,\mathrm{eV}$ when thermalized, remaining energy ratios of 10^{-3} or below are needed. Removing feedback and retuning the resonator during the cooling process reduces sufficient wait times to about one second until the cooled particle energy converges back to T_{Bg}.

resonator measurements, the off-resonator SNR
increase is visible for the 512 and 1024 ms acquisition times in which the particle is centred on a bin. For axial excitations to equal energy, the optimum point is expected to shift even further off-resonator.

When weakly coupling the particle to the resonator for PM measurements, care needs to be taken to cool the particle sufficiently, so the phase scatter for subsequent measurements remains low. In the used sideband cooling scheme, both the modified cyclotron and axial mode depend on the axial coupling for the particle to dissipate its excess energy above the thermal background. If the coupling is weakened, the cooling times increase proportionally to the inverse particle bin power in the resonator's power spectrum. The increase in necessary sideband cooling time depending on resonator detuning is illustrated in the left plot of Fig. 4.17, showing that even for moderate detunings, the cooling time dominates the total time taken by the PM sequence. To keep cooling times low, it is thus necessary to retune the resonator after a measurement sequence, so the coupling is only weakened during the acquisition time.

Alternatively, feedback can easily scale the power spectrum by at least a magnitude as shown in the right plot of Fig. 4.17, and can be turned off during cooling, circumventing the cooling time increase from the decreased coupling. After the particle is sufficiently cold, negative feedback can also be turned back on. The cooling time constant increases, but since negative feedback decreases the resonator temperature T_{Bg} felt by the particle, it is able to cool below the prior energy equilibrium, decreasing the initialization energy scatter.

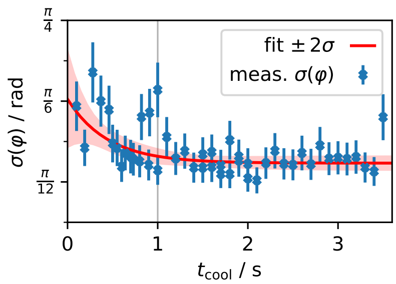

Figure 4.18: PnA cooling converges for cooling times $t_{\mathrm{cool}} \gtrsim 1\,\mathrm{s}$.

For the non-detuned and non-feedbacked measurements during the PM run, the neces-

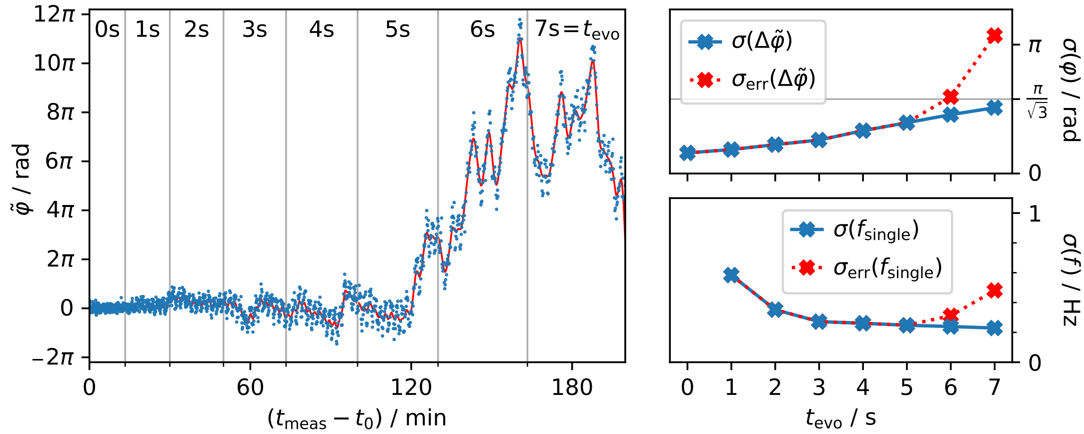

Figure 4.19: PM measurements are more sensitive to magnetic field fluctuations when using long evolution times. The increased sensitivity is visible in the phase difference scatter $\sigma(\Delta\tilde{\varphi})$ of the illustrated PnA evolution time sweep measurement, which converges to the random phase scatter limit around $t_{evo} \gtrsim 7\,\mathrm{s}$. By converting the naive phase scatter $\sigma(\Delta\tilde{\varphi})$ to the effective scatter $\sigma_{err}(\Delta\tilde{\varphi})$, the expected single phase frequency scatter $\sigma(f_{single})$ can be roughly estimated while also including the uncertainty increase due to a wrapping phase distribution. The total frequency error plateaus between 3 to 5 s. With the antiproton decelerator turned on, 3 s is thus the optimum evolution time due to the improved statistics compared to higher values of t_{evo}.

sary cooling time is estimated at 1 s using an otherwise optimized PnA measurement at varying cooling times. As can be seen in Fig. 4.18, no visible scatter improvements occur above $t_{cool} = 1\,\mathrm{s}$. Subsequent measurements use a conservative cooling time of 2 s.

4.4.7 Evolution Time Sequencing

Increasing the evolution time t_{evo} of a PM measurement will at most linearly increase the corresponding phase scatter contribution due to magnetic field drifts. Since the constant initialisation and readout scatter are independent of the evolution time, the resulting frequency scatter $\sigma(f_{single})$ from two phase measurements at $t = 0$ and t_{evo} decreases with increasing evolution time so long as the phase distribution can still be resolved without wrapping on itself.

$$2\pi\sigma(f_{single}) \sim (\sqrt{2}\sigma_{\varphi,const} + t\sigma_{\varphi,evo})\,/\,t = \sigma_{\varphi,evo} + \sqrt{2}\,/\,t \cdot \sigma_{\varphi,const}$$

The results of a phase distribution measurement with evolution times between 0 and 7 s are illustrated in Fig. 4.19. For each evolution time, 200 phases are acquired. They vary due to fluctuations in the magnetic field produced by random walks of the superconducting magnet and external sources described in the following subsection. The increased sensitivity of high t_{evo} measurements to these fluctuations can be seen clearly in the phase history chart. A phase measurement will acquire its phases quickly, so slow drifts are not relevant for the frequency scatter estimation and can be suppressed by looking only at the phase difference scatter $\sigma(\Delta\tilde{\varphi})$ of the unwrapped phases $\tilde{\varphi}$. It has its minimal value at $t_{evo} = 0\,\mathrm{s}$ and slowly converges to $\frac{\pi}{\sqrt{3}}$ as t_{evo} increases.

Above $t_{\mathrm{evo}} = 7\,\mathrm{s}$, the phase is effectively random and no information can be extracted from it, invalidating the naive frequency approximation described above. Some predictive quality can be recovered by converting $\sigma(\Delta\tilde{\varphi})$ to an effective single measurement phase error $\sigma_{\mathrm{err}}(\Delta\tilde{\varphi})$. As described in the note on Eq. (3.6), $\sigma(\Delta\tilde{\varphi})$ will not decrease with increased statistics with the expected $1/\sqrt{N}$ scaling. Instead, it initially remains somewhat constant, finally converging to $\sigma(\Delta\tilde{\varphi}) \approx \sigma_{\mathrm{err}}(\Delta\tilde{\varphi})/\sqrt{N}$ which would be expected of a quantity with a standard deviation of $\sigma_{\mathrm{err}}(\Delta\tilde{\varphi})$. Using this quantity to calculate the expected frequency scatter $\sigma_{\mathrm{err}}(f_{\mathrm{single}}) = \sigma_{\mathrm{err}}(\Delta\tilde{\varphi})/2\pi t_{\mathrm{evo}}$ takes the information loss from the phase distribution wrapping into account to yield an optimum evolution time of 3 to 5 s for minimum frequency scatter from a fixed number of PM measurements at t_{evo}. For a constant total measurement time, lower evolution times allow the acquisition of more phases, reducing the frequency uncertainty. With the additional constant peripheral time of 2 s used for instrument setup, DFT acquisition and cooling, the optimum evolution time is reduced to 2 to 4 s.

A PM measurement does not need to only measure phases for a single nonzero t_{evo}. Instead, iterating over a list of evolution times has some advantages, especially since small evolution times do not add much time to the total measurement sequence. If the evolution times are equally spaced, the FFT-based complex-space phase fitting algorithm described in Section 3.2.3 can be used, increasing the aliasing range from $\Delta f = 2\pi/\max t_{\mathrm{evo}}$ to $2\pi/\Delta t_{\mathrm{evo}}$ and making the measurement more robust against sudden shifts in frequency which would otherwise not be detected. Even for non-equally spaced evolution times, the unwrapping can be performed on low t_{evo} subsets first, to rule out neighbouring frequency aliases of the full frequency estimation. Such short t_{evo} measurements are especially necessary in calm magnetic field conditions such as the ones intended for the magnetic moment and charge-to-mass ratio measurements, where evolution times on the order of 100 s with aliasing ranges of 10 mHz are expected.

Furthermore, the amount of averaging does not need to stay constant between the values of t_{evo}. Intermediate phase values only used for aliasing range enlargements can be less precise than the phase determined from the maximum and minimum evolution time. Phase scatter increases with t_{evo}, so more measurements at greater evolution times need to be done for comparable phase scatters. By the above argument, most distinct evolution times are low, so phase scatters at $t_{\mathrm{evo}} = 0\,\mathrm{s}$ can be comparatively well known compared to the maximum evolution time phase scatter for even fewer 0 s measurements, especially since their phases should stay constant between two PM measurement sequences, allowing them to be reused, and thus reduced in a single measurement. The order of measurements matters as well. By the argument in Section 4.2.1, grouping the $t_{\mathrm{evo}} = 0\,\mathrm{s}$ at the beginning and end of the evolution time sequence reduces the time and resulting scatter of the nonzero evolution time measurements by ignoring the field fluctuations during the 0 s measurements. As a result, designing PM t_{evo} sequences allows a lot of freedom. In general, equally spaced sequences are the most robust, and exponentially increasing sequences the most precise for a given aliasing range.

For the precision-optimized measurement performed under the most stable magnetic field conditions during this thesis, described in Section 4.4.9, $t_{\mathrm{evo}} \in [0, 2, 8, 4, 8, 4, 8, 4, 8, 2, 0]\,\mathrm{s}$

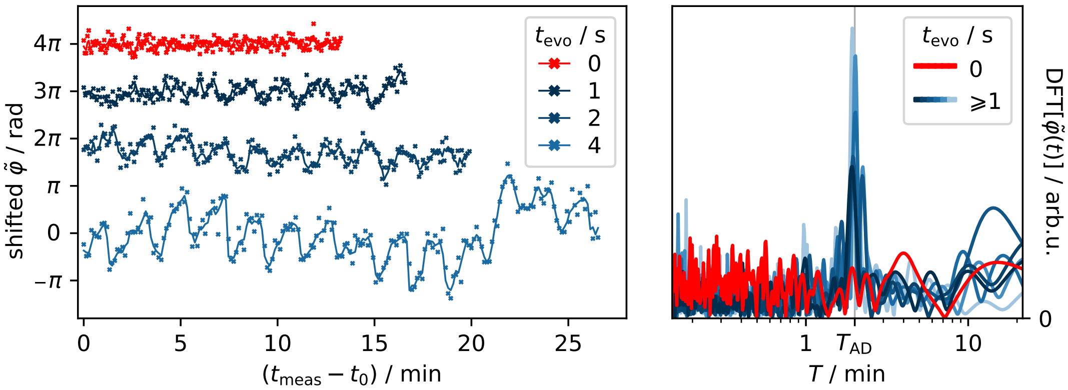

Figure 4.20: Phase fluctuations from the Antiproton Decelerator limit the maximum achievable evolution time to at most $t_{evo} = 4\,$s before the phase distribution begins to wrap. Without influence of the AD, much higher evolution times are achievable. With a period of 2 min, the AD cycle is the only periodic fluctuation visible in the phase history. In the linear spectrum shown on the right, the periodicity with the AD cycle is visible as a distinctive singular peak at a period length $T = 2\,$min for all evolution times $t_{evo} > 0$. The fluctuation is not felt by the $t_{evo} = 0\,$s reference measurement, validating it as a magnetic field effect.

is chosen as the evolution time sequence to use. It oversamples 0 s measurements so that all evolution times have similar densities and can be compared afterwards. The values are all powers of 2, so [0,2,4] and [0,4,8] can be extracted as robust measurement subsets to be fitted using the FFT-based complex-space phase fitting algorithm.

4.4.8 Antiproton Decelerator Cycling Effects

Magnifying the phase chart in Fig. 4.19 at evolution times below $t_{evo} = 5\,$s shows periodic phase fluctuations consistent with the antiproton decelerator period $T_{AD} \approx 120\,$s, illustrated in Fig. 4.20. Charting the movement of constant t_{evo} phases over time yields a periodic fluctuation superimposed on slow background drifts. During one cycle, the AD quickly ramps up its steering magnets to confine the injected highly energetic antiprotons. As the antiprotons get cooled, the magnets slowly ramp down to their initial value in three steps before the antiprotons get injected into ELENA and the cycle is restarted. As a result, a sawtooth-like wave is superimposed on the magnetic field everywhere inside the antimatter factory [27, 46], clearly visible in the phase history in Fig. 4.20. Because of this, the BASE STEP experiment has been designed with the intent of transporting antiprotons outside of CERN to conduct measurements without the AD fluctuations [56]. Until then, important measurements continue to be done during CERN's Christmas break, during which the AD is shut off. All measurements in this thesis were done outside the Christmas break.

As a magnetic field fluctuation, the amplitude of the induced phase fluctuations increases with t_{evo}, reaching a 2π wide span at about $t_{evo} = 5\,$s, corresponding to an axial magnetic field decrease of about 13 nT. In the reference measurement with an evolution time of 0 s, the magnetic field effect on the particle motion is small, and no phase fluctuations

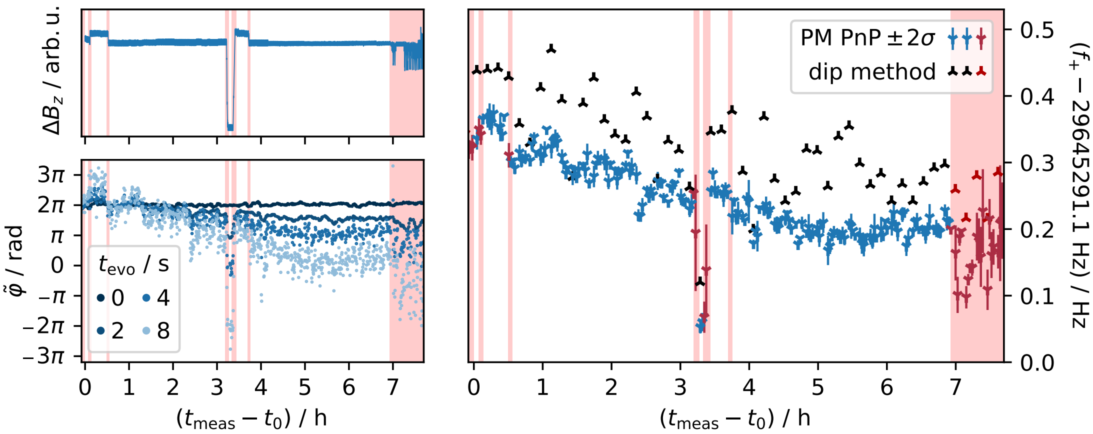

Figure 4.21: The only successful AD-off measurement, on the 2nd of September, 2024, was done to compare the optimized PnP and dip measurement. Removing times during which the magnetic field changes abruptly, phase scatters and drifts behave as expected, with the $t_{\text{evo}} = 8\,\text{s}$ phase scatter still significantly below $\pi/\sqrt{3}$. The estimated PnA frequency is much smaller, but the estimated $f_{+,\text{PnP}}$ is systematically shifted compared to $f_{+,\text{dip}}$.

are visible. Calculating a DTFT spectrum for each phase history marks the AD cycle at $T_{\text{AD}} = 2\,\text{min}$, and potentially its first harmonic as the only clear source of periodic phase oscillations detectable by repeated PM phase measurements.

By synchronizing the PM frequency estimation measurements to the AD cycle, the extra inter-measurement variability can be reduced, but the fluctuations remain as an increased frequency estimation uncertainty for each measurement. Still, if measurements must be performed with an active AD, synchronizing is advisable.

4.4.9 Measurements with an Idling Antiproton Decelerator

Due to an unexpected power cut and subsequent reinstatement problems in LINAC 4, antiproton production was interrupted for about 21 h, preventing the AD from fully restarting. During this time, and after ensuring the integrity of the BASE experiment, the mostly stable magnetic field conditions provided a prime opportunity for testing the optimized PM frequency estimation under improved conditions. After about 7 h of calm magnetic field conditions interspersed with some frequency jumps due to crane movements, the antiproton production was reestablished and the AD resumed its operation.

Using the evolution time sequence described above together with a constant total measurement setup and cooling time of 5 s results in a PM PnP measurement time of 103 s. With a single unaveraged default BASE spectrum at a 25 Hz span with 800 bins taking 32 s to acquire, the dip and double dip spectra are both averaged for 65 s to include 2 full spectra in the time average, totalling 134 s for the full sideband (SB) measurement. In magnetic moment measurements, an averaging time of 90 s is normally chosen, but the time was reduced here to be more comparable with the PM measurements.

In Fig. 4.21, the result of the measurements is illustrated. First, the magnetometer [150, 151] data was used to define regions of high magnetic field drifts caused by crane movements, during which any measurements will be discarded for calculations of frequency scatter. The field changes are visible in the unwrapped phase data, where the upscaled history of any t_{evo} measurements was iteratively used as a reference for phase unwrapping of the next greater evolution time measurements. This allows correct unwrapping even of the phase jumps caused by the abrupt field changes. Outside of those, the 8 s evolution time phase scatters remain at $\sigma(\Delta\tilde{\varphi}) \approx 1\,\mathrm{rad}$, comparable to a 3 s evolution time with an active AD cycle.

Moving to the estimated frequencies, the trends of both estimation methods agree, with SB results being sampled at a lower frequency, greater scatter, and systematically shifted from the PM frequencies by a constant amount. During the times of high magnetic field fluctuations, the PM frequency scatter increases as expected, while the SB frequency scatter does not. Figure 4.22 shows the phase distribution of both methods, from which the frequency estimation scatter can be obtained. The effect of the interspersed SB measurements on the PM frequency scatter is small, but it will be improved slightly without them. Likewise, the increased time between SB measurements due to the PM measurements increases the SB frequency scatter. However, going back to Fig. 4.21, the magnetic field variations between two SB measurements are small compared to the scatter between SB frequency, as can be seen by referencing the PM frequency history. Reducing the inter-SB duration will thus have a small effect on the SB frequency scatter as well, keeping the two comparable.

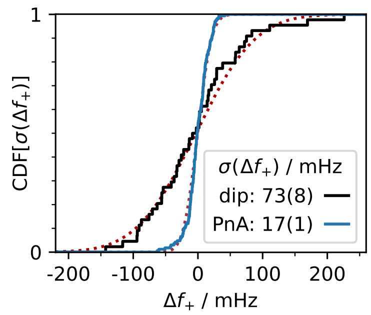

Figure 4.22: The PM PnP measurements strongly reduce the estimated frequency scatter in comparison to dip measurements using the data of Fig. 4.21.

Bringing everything together, an Allan deviation is used to compare dedicated overnight measurements of the modified cyclotron frequency acquired by three methods. The first dataset uses a conventional sideband double-dip detection scheme with an idling antiproton decelerator and was acquired during the 2024/25 magnetic-moment measurement campaing. The second dataset is the phase method dataset from Fig. 4.21 taken during a one-off temporary shutdown of the AD during 2024. A final dataset with an active AD and a cycle-triggered PM acquisition is included to compare it against the results with calm magnetic field conditions. The data is shown in Fig. 4.23. The PM Allan deviation frequency scatters agree with the 17(1) mHz from Fig. 4.22, while the dedicated sideband measurement under optimal conditions reaches scatters as low as 30 mHz. The scatters from the triggered PM measurement are worse than those for the PM measurement with an idling AD, but remain comparable to the optimal double-dip scatters. It is of note that the magnetic field drifted more slowly during the idling AD PM measurement, synthetically improving its scatter relaticve to the other methods.

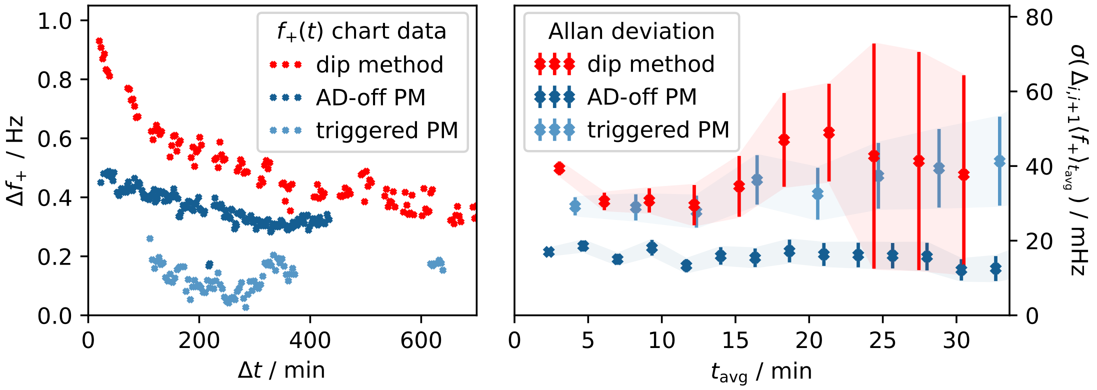

Figure 4.23: Phase methods improve the achievable frequency scatters dependent on averaging time t_{avg} compared to the conventional sideband double-dip measurements. A section of the frequency history is shown on the left, with the resulting Allan deviation for the full data set on the right. Due to the long regular absences of data in the dip method history, stemming from the particle spin initialisation and readout in the magnetic moment measurement routine, no usable data is available for averaging times $t_{avg} > 30$ min.

In summary, the implemented phase methods in their current state reach modified cyclotron frequency resolutions of 17(1) mHz, or 570 p.p.t. in relative units applicable to the magnetic moment. Sideband measurements only reach about 30 mHz, or 1.0 p.p.b. Everything else equal, this means a direct improvement of the magnetic moment precision, comparable to the multi-layer SSC upgrade in Fig. 1.1.

4.4.10 A Note on Systematics

The systematic shift visible in Fig. 4.21 and other prior comparison measurements stems from electromagnetic field inhomogeneities $(C_4, B_2, \dots)$ as touched upon in Ketter et al. [84], Borchert [80] and Section 2.2.1. Due to the limited time and high scatters with a cycling AD, characterization efforts have been unsuccessful. Some measurements show indications of the frequency shift scaling with varied parameters and particle energies, but existing data is too sparse to conclude much. For example, Fig. 4.24 was acquired over 5 days and compares systematic frequency shifts depending on the particle energy and B_2. The shifts increase with greater excitation energy as expected, but the B_2 scaling is not understood. Comparisons of frequency and phase scatter are also inconclusive. More characterization measurements of PM and peak measurements in general need to be done with an inactive antiproton decelerator gain quantitative understanding of the systematic shifts.

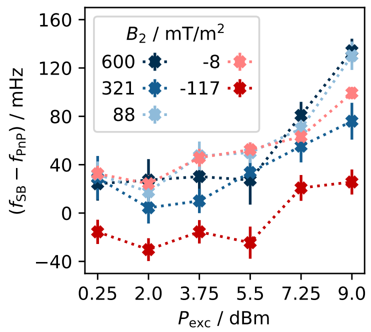

Figure 4.24: The systematic frequency shift increases for greater particle energies and behaves unexpectedly with variations in B_2.

5 $\bar{p}$ g-Factor Systematics

During the year of the writing of this thesis, measurements have been made for the next improved value of the magnetic moment of the antiproton. The author's contributions to the magnetic moment evaluation are three small systematics investigations used by the BASE group to guide evaluation decisions and to set bounds on systematic shifts. In order, they are the minimization of cyclotron frequency interpolation error during the measurement campaign, the investigation of the DFT dip frequency dependence on shifts of the resonator frequency, and the determination of the magnetic field inhomogeneities in the precision trap, from which the particle energy can be calculated.

5.1 Cyclotron Frequency Interpolation

The cyclotron frequency is continuously affected by power supply noise, magnetic field drifts and random walks, and external magnetic field changes, to name a few. Furthermore, the upkeep of the experiment includes mechanically opening the experiment to refill the connected cryostats with liquid nitrogen and liquid helium, commonly shifting the cyclotron frequency f_c by multiple Hz in the process. The BASE 2023/24 magnetic moment measurement campaign consists of 17 f_c histories, separated by events such as experiment refilling that inhibit continued frequency acquisition and remove any temporal correlations, and thus interpolated independently. As explained in Chapter 1, the cyclotron particle's acquired cyclotron frequency is interpolated to produce a best estimate of $\tilde{f}_c$ at the time of the Larmor particle's induced spin-flip, to calculate the g-factor from the ratio of the successful spin-flip drive and the interpolated cyclotron frequency [5]. The total measurement history is shown in Fig. 5.1, with a zoom on a representative single f_c history used to highlight the relevant considerations for the cyclotron frequency interpolation.

Each Larmor particle spin-flip is preceded by five cyclotron particle f_c measurements and followed by one. After the subsequent spin readout and reinitialization, the measurements repeat. Due to residual electrode and amplifier circuit equilibration effects after the transport of the Larmor particle back to the AT, and of the cyclotron particle back into the PT, the sixth f_c measurements, drawn as darker points, are systematically shifted from the other five converged measurements. They can either be ignored during the interpolation, or preprocessed to remove their assumed constant shift relative to

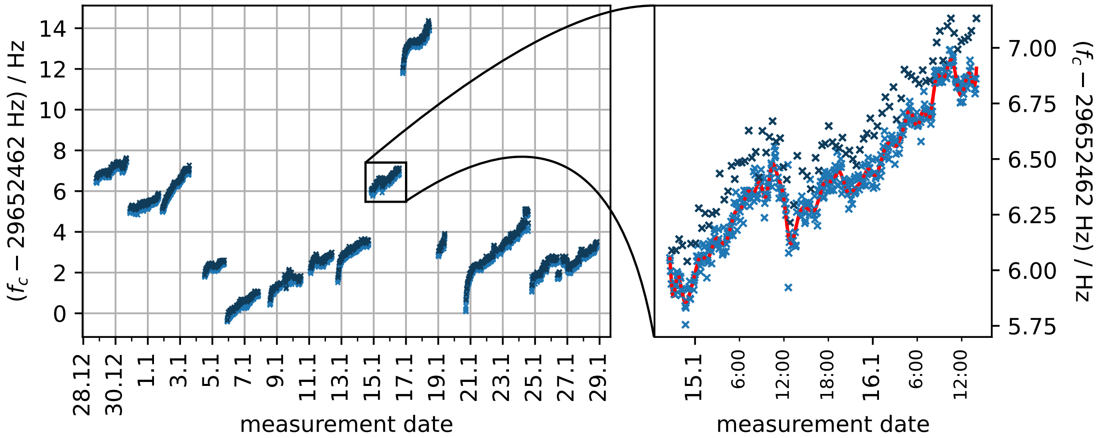

Figure 5.1: The magnetic moment measurement campaign contains two central quantities: The Larmor drive frequency and the cyclotron frequency shown here and calculated from the measured axial and modified cyclotron frequencies via the invariance theorem. The f_c measurement history is interrupted by refills of the experiment, which shift the cyclotron frequency. Even during one f_c history, the frequency drifts and some measurements are systematically shifted, complicating the creation of the interpolation function shown in red.

the other measurements. Multiple approaches for the interpolation type itself have been tested using leave-one-out cross-validation to compare their interpolation quality. Somewhat independently of the interpolation approach, compensating the sixth measurement point slightly improves the RMS frequency error by 0 to 8 %, although the improvement must be weighed against the introduction of another free fit parameter.

In the past, $\tilde{f}_c$ has been estimated as the average of the preceding group of k f_c measurements, so it is investigated here together with the k-nearest neighbour mean. Both approaches reach their minimum error at $k = 3$, with a slow increase in error at greater values of k. The nearest neighbour mean is an improvement over averaging the preceding measurements, improving the optimum RMS frequency error by about 15 %.

Using a random walk model for the cyclotron frequency, whose measurements are contaminated by detection errors, a full description inside the framework of Kalman filters reduces down to an exponentially weighted mean of the preceding measurements [134]. Furthermore, the k-nearest neighbour mean with equally spaced samples is effectively a cross-correlation of the f_c history with a rectangular kernel. Both arguments motivate the investigation of different kernels with greater weight on data points closer to the interpolation time. Here, the best interpolation is achieved by symmetric kernels similar to $\exp(-|\Delta t|/6\,\mathrm{min})$, being slightly better than the $k = 3$ nearest neighbour average.

Polynomial fits to the f_c histories, as done in prior experiments [80], are not sufficient anymore, mainly due to the length of the continuous f_c histories. If the amount of oscillations in the history doubles, the polynomial order needs to double as well to provide a comparable fit quality. Polynomial fitting also becomes extremely fragile at high orders, complicating the search for a sufficiently good fit.

The scaling problem can be circumvented by splitting the total history into segments of equal size instead, and fitting polynomials to those segments, with their orders determined by the lengths of the segments. Furthermore, the polynomials can be constrained to connect smoothly to minimize the effect of the separator positions on the frequency interpolation. The result is a least-squares polynomial spline fit with two free parameters, the order of the spline and the number of points per polynomial segment. The fit quality inside this parameter space is shown in Fig. 5.2. For high polynomial degrees and low numbers of cyclotron frequencies per segment, the spline overfits and the prediction becomes poor. Otherwise, the fit is very robust, only slowly decreasing in quality with increasing numbers of frequencies as the spline starts to only capture large scale trends in the f_c history. The valley of low interpolation error reflects the known scaling for polynomial fits. The greater the order of the spline, the higher the number of frequencies able to be sufficiently well interpolated. The optimal parameter set is reached at about seven frequencies per spline, slightly more than the number of measurements per spin flip, and for a wide range of spline orders. At these parameters, the interpolation error is comparable to the two-sided exponentially weighted mean.

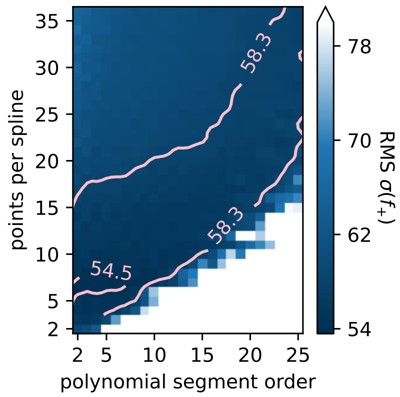

Figure 5.2: Spline interpolation works best at 7 points per spline and low spline orders, reaching RMS frequency errors of 54 mHz

The exponentially weighted mean with systematically shifted frequencies removed is the most physically sound approach. To minimize frequency errors further, the systematically shifted frequencies can be corrected, spline fits can be used, and the interpolation can be optimized for the specific measurement sequence.

The last point is relevant in that the frequency errors obtained in this investigation are larger than the corresponding errors in the magnetic moment evaluation, since the leave-one-out cross-validation used here as a proxy for interpolation quality weighs all frequency data points equally. In the magnetic moment measurement, only $\tilde{f}_c$, reached directly after five cyclotron frequency measurements, must be estimated. Still, a robust codebase remains; able to be used to test all further quality measured and interpolation approaches.

5.2 Resonator & Dip Shift over PT Axial Varactor Voltage

Over the $\bar{p}$ measurement campaign, the central resonator frequency f_R varies slowly over a frequency span on the order of 1 Hz. If this movement changes the measured $\bar{p}$ central dip frequency f_D, it will cause a systematic shift in the measured PT axial frequency, propagating into the measured g-factor. Thus, the change of f_D against f_R needs to be investigated to estimate its error contribution to the final g-factor value.

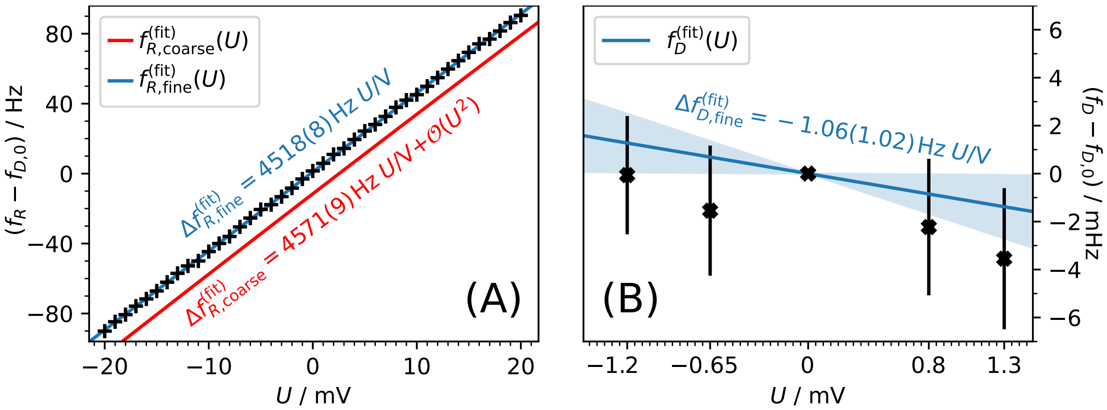

Figure 5.3: Both f_R (A) and f_D (B) scale linearly with the varactor voltage U.

To that end, a PT axial varactor circuit [152, 135] is used to intentionally vary the capacitance of the parallel RCL circuit acting as the PT axial resonator. Linearizing the frequency dependence on the varactor voltage U yields the frequency scaling.

$$f_R = \frac{1}{2\pi\sqrt{LC}} \qquad \Longrightarrow \qquad \Delta f_R \approx -\frac{f_R}{2}\frac{\partial C}{\partial U}\frac{\Delta U}{C}$$

From the measurements after the initial implementation of the varactor into the PT axial detection setup, the scaling seems to be sufficiently linear around $U = 0\,\text{V}$, with $\Delta f_R = 4.6(1)\,\text{kHz/V} \cdot \Delta U$ for $-0.3\,\text{V} < U < 0.3\,\text{V}$ [135].

First, a manual scan of f_R against $U \in [-0.5\,\text{V}, 0.5\,\text{V}]$ with 800 time domain samples, a 1600 Hz span and a 35 s averaging time is done to reestablish a rough frequency scaling so that the FFT can be automatically centred on $f_R(U)$. Oscillations in the amplifier circuit occur at $U = 0.5\,\text{V}$, so two automatic scans with the same parameters, a range of $U_1 \in [-0.5\,\text{V}, 0.3\,\text{V}]$, $U_2 \in [-20\,\text{mV}, 20\,\text{mV}]$, and steps of $\Delta U_1 = 50\,\text{mV}$, $\Delta U_2 = 1\,\text{mV}$ are repeated thrice to yield the spectra used for the resonator scaling calibration in Fig. 5.3 (A). Afterwards, the FFT span is decreased to 25 Hz and f_D is repeatedly measured for $U \in \{0,\ 1.3,\ 0.8,\ 0,\ -0.65, -1.2\}\,\text{mV}$ in this order. The $f_D\big|_{U=0}$ measurements are used to interpolate a reference dip frequency against which the shifted frequencies can be compared. This imposes a value of $\Delta f_D\big|_{U=0} = 0(0)$ and f_D distributions at the other four values of U, from which the f_D scaling can be fitted. Assuming the measured f_D are sampled from a normal distribution caused by noise, the distributions can be simplified after fitting to mean values with their uncertainties, shown in Fig. 5.3 (B).

The resonator and dip spectra are refitted for all scans by standardized routines from K. Franke. Both resonator scans suffer from noise peaks on top of the resonator spectra. For the fine scan, the FFT span stays the same and the noise peaks are mostly localized to $f < 636.4\,\text{kHz}$. So this frequency range is cut before fitting to reduce the noise peak impact. For the coarse scan, all spectra where a noise peak is responsible for the maximum (max PSD $> -72\,\text{dBVrms}$) are not fitted at all, while the others are fitted as is. The spectra will be fitted less precisely, and the wider span of U causes noticeable second-order terms in $f_R(U)$, but the coarse scan scaling will not be used further and is calculated only to compare the scaling for larger variations in U with the fine scan result in Fig. 5.3 (A).

For the dip scan, no noise peaks occur in the smaller FFT span used for the dip fits. Furthermore, as the $-3\,\mathrm{dB}$ resonator width is 73(2) Hz and the measured power spectrum scatters over a range of about 15 dB, the resonator shape is not visible at the 25 Hz dip FFT span. Thus, the resonator dip shape is fitted against a fixed resonator background with a width of 73 Hz and a center given by the scaling in Fig. 5.3 (A), giving Fig. 5.3 (B).

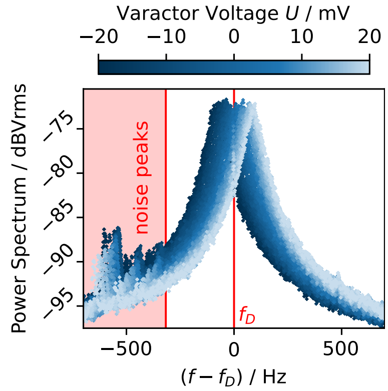

Figure 5.4: Resonator spectrum noise peaks for $-20\,\mathrm{mV} < U < 20\,\mathrm{mV}$.

Referencing both scan shifts against each other removes the dependence on the externally changed varactor voltage U and allows estimating the systematic g-factor error contribution from the dip-shifting effect.

$$\left.\frac{\partial f_D}{\partial f_R}\right|_{U=0} = -0.24(23) \cdot 10^{-3} \tag{5.1}$$

As $\Delta f_R \sim 1\,\mathrm{Hz}$, an axial dip shift of $\Delta f_D \sim 0.24(23)\,\mathrm{mHz}$ is obtained. Using the sideband method to indirectly measure the cyclotron frequency f_c depends on $f_D \equiv f_z$ in two ways, directly in the formula for f_c, and via the propagation through the magnetron and modified cyclotron frequencies f_-, f_+.

The modified cyclotron frequency is measured using the sideband method, where the radiated RF drive frequency f_{RF} is known precisely. Because the magnetron frequency is small, it is approximated by its formula for a perfect penning trap.

$$f_+ = f_{z,\mathrm{l}} + f_{z,\mathrm{u}} - f_z + f_{\mathrm{RF}} \qquad f_- \approx \frac{f_z^2}{2f_+} \qquad f_c = \sqrt{f_+^2 + f_z^2 + f_-^2} \tag{5.2}$$

Because the axial and sideband measurements yielding f_z and the lower and upper sideband $f_{z,\mathrm{l}}, f_{z,\mathrm{u}}$ are fast ($\sim 5\,\mathrm{min}$) compared to the resonator drift ($\sim 24\,\mathrm{h}$), all three axial shifts used in the calculation of f_+ reference the same resonator shift. From theoretical investigations of Hann-windowed resonator dip and double dip spectra, it is known that $\Delta f_{z,\mathrm{l}} = \Delta f_{z,\mathrm{u}} = 2\Delta f_D$ are shifted twice as much as the measured central dip frequency $\Delta f_z = \Delta f_D$. In the calculation of the modified cyclotron frequency, these shifts partially cancel such that $\Delta f_+ = 3\Delta f_D$. Both axial and magnetron error contributions $\Delta f_z = \Delta f_D$ and $\Delta f_- \approx \frac{f_z}{f_+}\Delta f_D$ are insignificant in their propagation into f_c.

$$\frac{\Delta f_c}{f_c} \approx \frac{1}{f_c}\sqrt{\left(3\,\frac{f_+}{f_c}\right)^2 + \left(\frac{f_z}{f_c}\right)^2}\,\Delta f_D \approx 3\,\frac{f_+}{f_c^2}\Delta f_D \approx \frac{3\Delta f_D}{f_c} \tag{5.3}$$

With $f_c \approx 29.645\,\mathrm{MHz}$, the relative cyclotron error becomes $\Delta f_c / f_c = -24 \pm 23$ p.p.t.

5.3 Axial Temperature & Burst Excitation Energy Scaling

Using the PT radial excitation line and applying a drive at the modified cyclotron frequency will excite the modified cyclotron mode to an amplitude r_+ proportional to the drive time. For improved timing control, the function generator [140] is not driving the particle for a fixed time, but for a fixed number N of periods of the drive frequency. At high modified cyclotron mode energies $E_+ \propto r_+^2 \propto N^2$, axial dip frequency and modified cyclotron peak frequency noticeably shift proportionally to E_+ [80, 84].

$$\frac{\Delta f_z}{f_z} = \left(-\frac{1}{2mc^2} - \frac{3}{2}\frac{1}{qV_R}\frac{C_4}{C_2^2}\frac{f_z^2}{f_+^2} + \frac{1}{4\pi^2 f_z^2 m}\frac{B_2}{B_0}\right)E_+ + \mathcal{O}\big(B_4, E_+^2, \dots\big) \tag{5.4}$$

$$\frac{\Delta f_+}{f_+} = \left(-\frac{1}{mc^2} + \frac{3}{4}\frac{1}{qV_R}\frac{C_4}{C_2^2}\frac{f_z^4}{f_+^4} - \frac{1}{4\pi^2 f_+^2 m}\frac{B_2}{B_0} - \frac{1}{4\pi^2 f_z^2 m}\frac{B_1^2}{B_0^2}\right)E_+ + \mathcal{O}(\dots) \tag{5.5}$$

Knowing the ring voltage V_R and coefficients C_2, C_4, B_0, B_2 of the optimized trap, reference axial and modified cyclotron frequencies f_z, f_+, and the fundamental constants $c, q_{\bar{p}}, m_{\bar{p}}$ allows calculation of E_+ and thereby also axial temperature T_z from measurements of Δf_z or Δf_+. $C_4 = 0$ is assumed. During the measurement, the resonator was partially feedback-cooled, resulting in two datasets with equal B_2, but different T_z.

5.3.1 B_1 and B_2 Evaluation

While most of the mentioned values stay relatively constant, B_1 and B_2 vary over time from intentional changes to the setup and must be reevaluated before the energy scaling can be determined. The equations from which to calculate B_1 and B_2 are given in Section 4.4.1 and Section 4.4.2.

The relative error of a B_1 measurement is much smaller than the corresponding relative error of a B_2 measurement when acquired over comparable measurement durations. B_1 is also less relevant than B_2 for the determination of the energy scaling, having no first-order effect on the axial frequency shift used to determine the scaling behaviour. As such, B_1 has been measured quickly and without much concern for the study of e.g. initial fit parameter choices. The measurement has no changes compared to the one in Section 4.4.1, and results in a cyclotron frequency shift depending on the P4 offset voltage of $\xi = 2\pi \cdot 94.7(6)\,\mathrm{Hz/V}$. The same value for η is chosen. Reusing Eq. (4.3) yields $B_1 = 10.15(6)\,\mathrm{mT}$

To determine B_2 using Eq. (4.6), the slope ξ of f_+ against f_z obtained by varying E_+ is needed again. This can be combined in a shared B_2 and energy scaling sequence, where the measurement of both dip and peak frequency, while unnecessary for the energy scaling, also allows determining B_2 with the same dataset. For both loaded B_2, an initial axial spectrum is taken, and the particle is excited by $1000k$ bursts for $k \in \{6, 8, 10, 12, 13\}$. Afterwards, a simultaneous cyclotron and axial spectrum is acquired, with the particle still in its excited state. Subsequently, the particle is sideband-cooled to thermalize the modified cyclotron mode. Finally, the next k is chosen and the sequence repeats. The axial frequency dip spectra were set to a span of 50 Hz, averaged for 34 s, and are all well resolved. Analogous to Section 5.2, even at a 50 Hz span the resonator is not sufficiently visible to fit a resonator dip shape without large scattering in the fitted resonator parameters. However, the resonator is tuned to constant parameters during the whole measurement, and the initial dip spectra should all share the same shape with only minor dip frequency movement. All initial axial spectra were thus averaged to obtain a smooth reference against which a resonator dip shape can be fitted to obtain fixed initial resonator parameters for all spectra. They are shown in Fig. 5.6 (A).

Due to the noise in the resonator spectrum, even the fit of the average of the initial spectra may be slightly off from the correct values. Judging from Fig. 5.6 (A), both resonator width $\delta f_{\mathrm{R},0}$ and center $f_{\mathrm{R},0}$ are clearly detectable with possible ranges $\frac{3}{4}\delta f_{\mathrm{R,fit},0} \lesssim \delta f_{\mathrm{R},0} \lesssim 2\delta f_{\mathrm{R,fit},0}$ and $-1\,\mathrm{Hz} \lesssim f_{\mathrm{R},0} - f_{\mathrm{R,fit},0} \lesssim 1\,\mathrm{Hz}$. Furthermore, the resonator is potentially drifting in frequency on the order of 1 Hz. For this reason, the effect of varying the initial fit parameters $\delta f_{\mathrm{R},0}$ and $f_{\mathrm{R},0}$ on the fitted excited axial dip frequencies f_D is investigated in Fig. 5.6 (B). Either effect shifts f_D by less than 25 mHz while excitation leads to axial frequency shifts on the order of Hz. Minimizing the excited dip fit residuals over $\delta f_{\mathrm{R},0}$ and $f_{\mathrm{R},0}$ leads to values within the above ranges as well, with the results $\delta f_{\mathrm{R,min}} = 0.9\,\delta f_{\mathrm{R},0}$ and $f_{\mathrm{R,min}} = f_{\mathrm{R},0} + 0.7\,\mathrm{Hz}$, causing a dip frequency shift of 4.5(4) mHz. As neither resonator width nor resonator centre frequencies are changing with different E_+, the systematic shifts in f_D are comparable, as can be seen from the 1σ mean deviation region in Fig. 5.6 (B). thus, shifts in slope of $f_D(N^2)$ are diminished to 1%, less than the uncertainty.

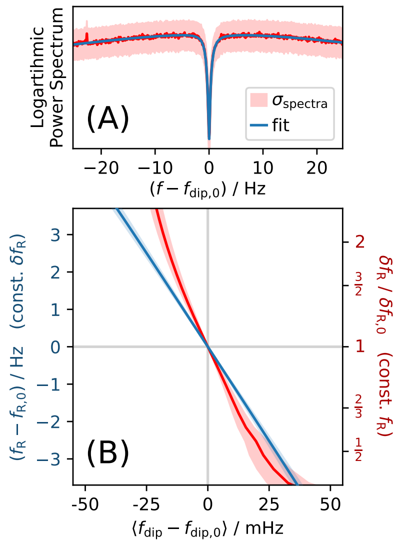

Figure 5.5: Determination of the resonator shape from the reference dip averages (A), and dip frequency dependence on varying resonator center frequency and dip width (B).

The axial peak spectra were set to a 25 Hz span and averaged for 34 s as well. At lower energies, specifically at 6000 Bursts, a noise bin sometimes accumulates more energy than the signal frequency bin. For these spectra, the peak frequency is incorrectly fitted, and can not easily be corrected, because the signal frequency bin is ambiguous. The spectra are therefore filtered by the probability that a bin with the power of the largest bin in the spectrum arises purely from the rayleigh distribution of the spectrum noise background; their p-value. In Fig. 5.6, the standard deviation σ_{sample} of the peak frequency distribution for all burst numbers against the maximum p cutoff. For small p, σ_{sample} behaves erratically, as most low burst number spectra are filtered out. Increasing p lets σ_{sample} to converge until $p = p_{\mathrm{crit.}}$, after which incorrect fits of spectra with $N = 6000$ cause σ_{sample} to increase sharply. For the dataset, $p_{\mathrm{crit.}}$ is reached for $p = 8 \cdot 10^{-3}$ and used as filter, retaining all spectra for $N \geqslant 10000$. A singular remaining outlier is manually removed.

The fitted peak and dip spectra now allow estimating B_2 via Eq. (4.6) by fitting a linear function onto the (f_+, f_z) dataset. However, f_+ drifts considerably over the time of the measurements. This drift has to be corrected for higher accuracy of the slope fitting approach, which can be done by subtracting a lowpass filtered version of the data from itself. The exact type of filter is however hard to justify and will affect the obtained slope. $\partial_{N^2} f_+$ and $\partial_{N^2} f_z$ can be fitted separately to obtain $\frac{\partial f_+}{\partial f_z} = \partial_{N^2} f_+ \big/ \partial_{N^2} f_z$, but this also requires drift correction for $\partial_{N^2} f_+$. An improved drift shape independent approach is outlined below.

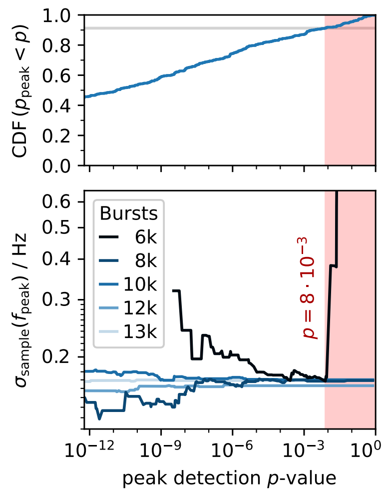

Figure 5.6: Dependence of the peak frequency distribution σ_{sample} on the data filtering cutoff. Above, the fraction of remaining data depending on the cutoff is shown. 8.8% is discarded at the optimum cutoff.

f_+ should scale linearly with f_z. Thus assuming a scaling $f_{+,i} = f_{+,\mathrm{ref}} + \xi(f_{z,i} - f_{z,\mathrm{ref}})$, all f_+ can be mapped to their reference values $f_{+,\mathrm{ref},i} = f_{+,i} + \xi f_{z,\mathrm{ref}} - \xi f_{z,i}$. Here, $\xi f_{z,\mathrm{ref}}$ is irrelevant, as it is constant for a non-drifting axial reference frequency. The corrected $f_{+,\mathrm{ref},i}$ should now show only the drift background, with all excitation scatter removed. Assuming the drift to be a slow random walk, $\Delta f_{+,\mathrm{ref},i} := \frac{f_{+,\mathrm{ref},i+1}}{2} + \frac{f_{+,\mathrm{ref},i-1}}{2} - f_{+,\mathrm{ref},i}$ should be small, and dominated by the scatter if ξ is chosen incorrectly. Thus, the optimal scaling can be found by least-squares optimizing the residuals over ξ, yielding the frequency slope $\frac{\partial f_+}{\partial f_z} = \xi = 50.7(5)\,\mathrm{mHz/Hz}$ required in Eq. (4.6).

The value is in agreement with the other methods, but with a smaller error capped by the frequency dip uncertainty. The evaluation is robust even if the drift is biased, e.g. moving downwards over time. Using the average axial and peak frequency $\langle f_+ \rangle = 29\,645\,636.6(2)\,\mathrm{Hz}$, $\langle f_z \rangle = 636\,722.0(2.2)\,\mathrm{Hz}$ for Eq. (4.6) is sufficient as the error is dominated by the frequency slope, and results in $B_2 = 637(9)\,\mathrm{mT/m^2}$.

5.3.2 Energy Scaling

The estimation of B_2 finally allows converting from the dip spectra measurements $f_z(N) = f_{z,0} + N^2\,\partial_{N^2} f_z$ to $E_+(N)$ via Eq. (5.4):

$$
\begin{aligned}
E_+(N) &= \left(\frac{1}{4\pi^2 f_z^2 m} \frac{B_2}{B_0} - \frac{1}{2mc^2} \right)^{-1} \frac{\partial_{N^2} f_z}{f_z} N^2 \\
&= 35.88(52)\,\mathrm{neV} \cdot N^2 \quad \text{(feedback, Fig. 5.7)} \\
&= 35.87(62)\,\mathrm{neV} \cdot N^2, \quad \text{(no fb. cooling)}
\end{aligned}
$$

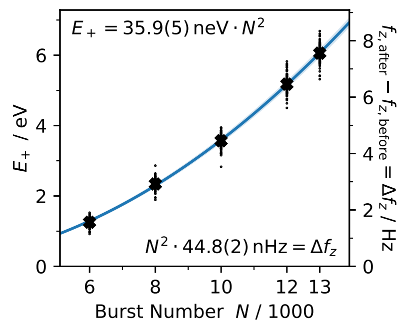

Figure 5.7: E_+ and Δf_z dependence on N of the feedback-cooled data.

where the uncertainty in $E_+ \big/ N^2$ stems mostly from B_2. Values with and without feedback cool-

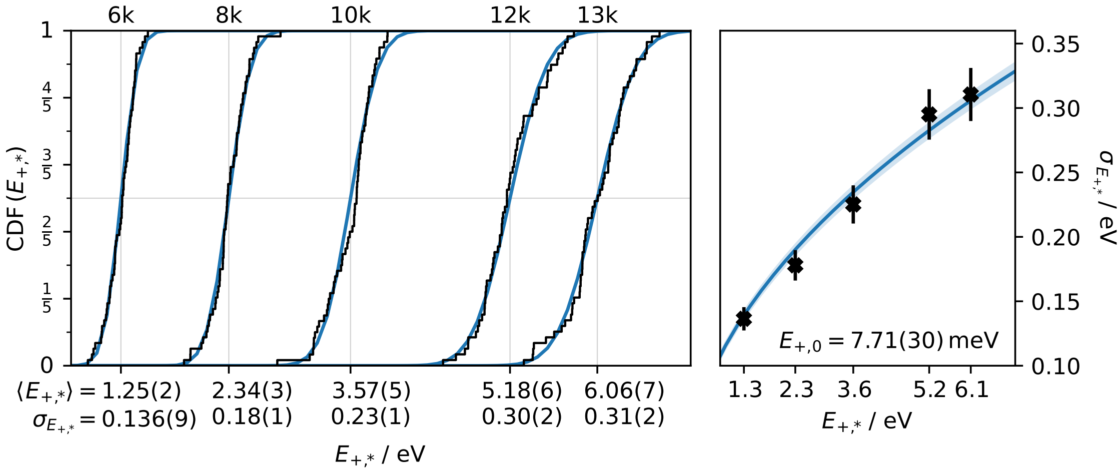

Figure 5.8: Axial temperature evaluation for the feedback-cooled measurement dataset. The cumulative density functions of the measured axial frequency converted to modified cyclotron energy (left) yield the energy scatter $\sigma_{E_{+,*},N}$ for all N. Equation (5.6) can then be fitted against $\sigma_{E_{+,*},N}$ to obtain $E_{+,0}$ (right).

ing are consistent Using Δf_z instead of Δf_+ for recovery of $E_+(N)$ circumvents drift correction.

5.3.3 Axial Temperature

Before each of the measurements, the particles modified cyclotron mode is sideband-cooled and in constant interaction with the axial resonator heat bath via the sideband-coupling to the axial mode. It is thus staying thermalized with an average energy $\langle E_{+,0}\rangle = f_+ / f_z \cdot \langle E_{z,0}\rangle = f_+ / f_z \cdot k_B T_z$ until the sideband coupling stops, after which the final modified cyclotron energy $E_{+,0}$ is selected from the Boltzmann distribution $P(E_{+,0}) = \exp\left(-f_z E_{+,0} / f_+ k_B T_z\right)$. Afterwards, the particle is excited up to an expected energy $E_{+,*}$, where the peak and dip spectra are measured before the cycle repeats. From Eq. (2.51), the standard deviation σ_{E_+} in cyclotron energy of an excited particle is known to be

$$\sigma_{E_{+,*}} = \sqrt{2E_{+,0}E_{+,*}}\sqrt{1 - \frac{1}{2}\frac{E_{+,0}}{E_{+,*}}} \tag{5.6}$$

which can be fitted against the energy calibration data in Fig. 5.7 to recover the initial thermal energy of the particle. Via the evaluation shown in Fig. 5.8 for the feedback cooled dataset, $\sigma_{E_{+,*}}$ is obtained from the $E_{+,*}$ scatter so that $E_{+,0}$ can be obtained by fitting Eq. (5.6). For both datasets, $E_{+,0}$, $E_{z,0} = f_z / f_+ \cdot E_{+,0}$ and $T_z = E_{z,0} / k_B$ are estimated to the following values:

	$E_{+,0}$ / meV	$E_{z,0}$ / µeV	T_z / K
feedback cooled	7.7(3)	165.6(6.4)	1.921(74)
not feedback cooled	34.9(2.4)	749(52)	8.69(60)

6 | Conclusion

This thesis has given a comprehensive introduction to the topic of phase-sensitive modified cyclotron frequency measurements in the BASE-CERN experiment, covering in a broadly chronological way the theoretical and experimental steps towards a successful implementation. Similar in kind to Chapter 5 of Schneider [81] and Chapter 9 of Borchert [80], it reiterates the working principle of phase-sensitive modified cyclotron frequency measurements via axial mode excitations and the necessary experimental parameter optimizations, while also elaborating on evaluation methods of the acquired phase data and extending the experimental section to include the acquisition test setup and implementation details of the 2024 phase method iteration.

After the prerequisite non-destructive particle detection theory, the thesis covers the preparation of the particle into a state of phase-encoded frequency information, and how to acquire this information by timed mode-coupling and DFT-readout. A test setup had been assembled (Fig. 3.8), correctly validating the readout SNRs and phase-estimation uncertainties. Afterwards, it has been extended and repurposed as an experiment-facing setup (Fig. 4.6), able to manipulate and phase-sensitively detect antiprotons, providing a successful proof-of-concept of such detection schemes at BASE.

Two algorithms are developed to extract the particle frequency from the phase data, and are compared against a naive unwrapping approach. They are shown to improve limiting SNR contrains under synthetic test conditions by up to a factor of two (Fig. 3.12) by avoiding the discontinuities introduced by mapping phases into the reals.

After the successful demonstration of the first modified cyclotron measurement using the phase-sensitive measurement setup (Fig. 4.9), the measurement scheme has been further optimised during Section 4.4 under suboptimal conditions, achieving a two-fold improvement in frequency precision compared to conventional dip-methods (Section 2.2.2) in its first measurement run in conditions comparable to the measurements of [5, 6], and with further improvements expected after optimization in such conditions. In the antiproton magnetic-moment measurements, the cyclotron scatter is the dominant error, and any improvement in the modified cyclotron frequency will translate directly into improvements of the magnetic moment as soon as the systematic phase-method frequency shifts mentioned in Section 4.4.10 are fully understood. Future charge-to-mass ratio measurements are impacted in the same manner, spending their error budget on the axial and modified cyclotron frequency scatter of the two measured species [6].

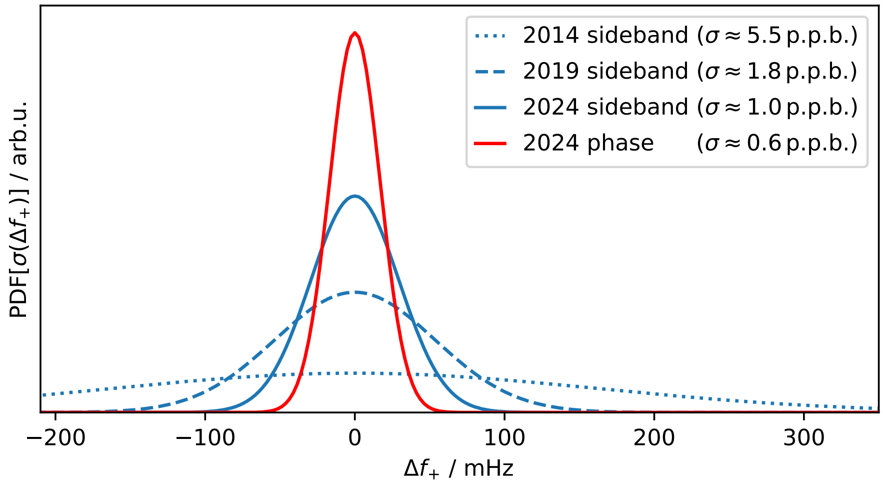

Figure 6.1: The improvements to the BASE experiment [65], already shown in Fig. 1.1 for peak-methods, have continually decreased the width of the modified cyclotron scatter distribution. For the current phase method implementation without further optimizations, the resulting distribution is compared with historical dip-method results. additional phase method optimizations will improve the distribution width further.

The implemented modified-cyclotron phase method paves the way for the development of axial phase methods on the same hardware, with external coordination of increased and decreased detection resonator interaction, currently worked on by S. Erlewein and B. Arndt [55]. In magnetic moment measurements [5], with spin initialization and readout dependent on the AT axial frequency measurement time and precision, axial AT phase methods will reduce the total sequence measurement time or increase the certainty of the (non-)measured spin flip, improving statistics and thus precision. In charge-to-mass ratio comparisons, the improved axial precision translates into reduced measurement times for comparable axial errors, and thus improved statistics by a factor up to two.

Chapter 5 presents the author's contribution to the 2024 magnetic moment measurement campaign. The work is disconnected from the bulk of the thesis, but time intensive and relevant to the purpose of BASE; and thus included for completeness. It covers the calculation of a selection of experimental parameters and systematic errors, and a general investigation into the possible recovery of intermediate frequency information from averaged discrete noisy samples.

As phase-sensitive frequency measurements remain the only option with precision scaling linearly with time, they are desirable for all Penning-trap precision measurements of sufficient frequency stability, and have also been implemented in other experiments [136]. The developments of this thesis will thus remain useful for BASE in the years to come.

A | Appendix

A.1 Analytic DFT of a Windowed Sinusoidal Signal

The forward-normalized DFT [90] $(y_p)_p$ of a sequence $(x_q)_{q\in 0,\dots,N-1}$ with length N is defined as

$$y_p = \frac{1}{N}\sum_{q=0}^{N-1} x_q\, e^{-2\pi i \frac{pq}{N}}. \tag{A.1}$$

Given corresponding times $t = (t_0 + q\Delta t)_{q\in 0\dots,N-1}$ at which x was sampled, y_p specifies the amplitude of the frequency component with angular frequency $\omega = p \big/ N\Delta t$. The statement only truly holds if x is periodic in time with a period of $N\Delta t$ and y is evaluated only for $p \in \{-\lfloor N/2\rfloor, \dots, \lfloor (N-1)/2\rfloor\} \big/ N\Delta t$. But even for imperfectly $N\Delta t$-periodic signals and noise, the DFT values can interpreted in a useful way.

For the subsequent derivations, the following variables are defined: $\omega_S \coloneqq 1 \big/ \Delta t$ is the angular sampling frequency of the sequence and $\omega_B \coloneqq 1 \big/ N\Delta t$ its angular frequency bin-width. If the signal x oscillates, it does so with angular frequency ω_0, and $\Delta\omega = \omega - \omega_0$ is the difference of ω from ω_0. Converting Eq. (A.1) into a frequency-dependent form, sampling a function $x(t)$, yields

$$y(\omega) = \frac{\omega_B}{\omega_S}\sum_{q=0}^{N-1} W\!\left(\frac{q}{N}\right) x\!\left(\frac{2\pi q}{\omega_S}\right) e^{-i\frac{2\pi q}{\omega_S}\omega}, \tag{A.2}$$

which is more useful for determining signal frequencies than Eq. (A.1). Here, a window function $W\colon [0,1] \to \mathbb{R}$ is included, which is used in DFT calculations because suitable windows can improve the DFT characteristics. For example, the Hann window, defined below, decreases the DFT values of a sinusoidal signal for all frequencies further than $\sqrt{2}\omega_B$ away from ω_0 respective to an unwindowed DFT. It is thus useful for resolving small frequency components around another, much larger one.

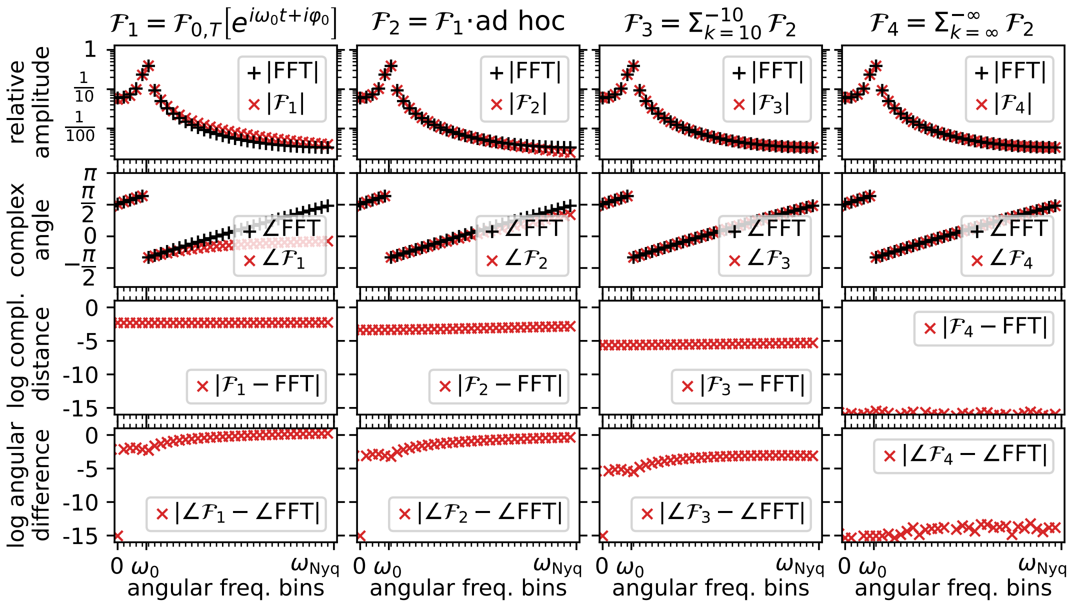

Figure A.1: Comparison of different DFT approximation approaches with the calculated DFT for a sinusoidal signal with $\omega_0 = 29.2/T$ and $\varphi_0 = 1.6$. Left to right, the columns show Eq. (A.5), Eq. (A.5) with ad hoc terms, the superposition of 21 harmonics, and Eq. (A.6).

A.1.1 Rectangular Window

Let $x(t) = e^{i\omega_0 t}$ and $W \equiv 1$. The DFT is a linear operator, so different functions can be scaled and added either before, or after applying the DFT without affecting the result. As $A\cos(\omega_0 t + \varphi_0) = \frac{A}{2}\left(e^{i(\omega_0 t+\varphi_0)} + e^{-i(\omega_0 t+\varphi_0)}\right)$ and $e^{-i(\omega_0 t+\varphi_0)} = e^{i\varphi_0} e^{i(-\omega_0)t}$, calculating the DFT of $e^{i\omega_0 t}$ also yields the DFT of an arbitrary sinusoidal signal.

$$
\begin{aligned}
y(\omega) &= \frac{\omega_B}{\omega_S} \sum_{q=0}^{N-1} e^{i\frac{2\pi q}{\omega_S}\omega_0}\, e^{-i\frac{2\pi q}{\omega_S}\omega} = \frac{\omega_B}{\omega_S} \sum_{q=0}^{N-1} e^{i\frac{2\pi q}{\omega_S}(\omega_0-\omega)} \\
y(\Delta\omega) &= \frac{\omega_B}{\omega_S} \sum_{q=0}^{N-1} e^{-i\frac{2\pi q}{\omega_S}\Delta\omega} \\
&= \frac{\omega_B}{\omega_S} \frac{e^{-iN\frac{2\pi}{\omega_S}\Delta\omega}-1}{e^{-i\frac{2\pi}{\omega_S}\Delta\omega}-1} = \frac{\omega_B}{\omega_S} \frac{e^{-i\frac{2\pi}{\omega_B}\Delta\omega}-1}{e^{-i\frac{2\pi}{\omega_S}\Delta\omega}-1} = \frac{\omega_B}{\omega_S} \frac{e^{-i\frac{\pi}{\omega_B}\Delta\omega}-e^{i\frac{\pi}{\omega_B}\Delta\omega}}{e^{-i\frac{\pi}{\omega_S}\Delta\omega}-e^{i\frac{\pi}{\omega_S}\Delta\omega}}\, e^{i\pi\left(\frac{1}{\omega_S}-\frac{1}{\omega_B}\right)\Delta\omega} \\
&= \frac{\omega_B}{\omega_S} \frac{\sin\left(\pi\frac{\Delta\omega}{\omega_B}\right)}{\sin\left(\pi\frac{\Delta\omega}{\omega_S}\right)}\, e^{i\pi\left(\frac{1}{\omega_S}-\frac{1}{\omega_B}\right)\Delta\omega} \qquad \text{(A.3)}
\end{aligned}
$$

The exponential term in Eq. (A.3) contains all the complex angle information. It oscillates in $\Delta\omega$-space with period $2\omega_B\omega_S/(\omega_B - \omega_S) = \mathrm{HarmonicMean}(\omega_S, -\omega_B)$, and can be removed for the amplitude of the DFT (ignoring sign), since the amplitude of an imaginary exponential is 1.

From the viewpoint of DFTs as approximations of Fourier transforms $\mathcal{F}$, the naive expectation of the sinusoidal signal DFT would be a dirac delta function.

$$\mathcal{F}\left[e^{i(\omega_0 t+\varphi_0)}\right](\Delta\omega) = e^{i\varphi_0}\delta(\Delta\omega) \tag{A.4}$$

Considering that the DFT only uses data at times $t \in [0, N\Delta t]$ and masking the function outside of that region improves the Fourier transform DFT approximation.

$$\mathcal{F}_{t\in[0,T]}\left[e^{i(\omega_0 t+\varphi_0)}\right](\Delta\omega) = e^{i\varphi_0} e^{-i\pi\frac{\Delta\omega}{\omega_B}} \operatorname{sinc}\left(\pi\frac{\Delta\omega}{\omega_B}\right) \tag{A.5}$$

Finally, taking into account aliasing means that two sampled signals with angular frequencies $\omega_0 + k\omega_S$, $k \in \mathbb{Z}$ are indistinguishable from each other. Thus, one signal contributes multiple times to each DFT value, analogous to a Fourier transform of the superposition of all signals with frequencies $\omega_0 + \mathbb{Z}\omega_S$.

$$\begin{aligned}
\mathcal{F}_{t\in\mathbb{R}/T\mathbb{Z}}\left[e^{i(\omega_0 t+\varphi_0)}\right](\Delta\omega) &\mathrel{\hat{=}} e^{i\varphi_0} \sum_{k\in\mathbb{Z}} \overbrace{(-1)^k e^{i\pi\frac{\Delta\omega}{\omega_S}}}^{\text{ad hoc terms}} e^{-i\pi\frac{\Delta\omega+k\omega_S}{\omega_B}} \operatorname{sinc}\left(\pi\frac{\Delta\omega+k\omega_S}{\omega_B}\right) \\
&= e^{i\varphi_0} \frac{\omega_B}{\omega_S} \frac{\sin\left(\pi\frac{\Delta\omega}{\omega_B}\right)}{\sin\left(\pi\frac{\Delta\omega}{\omega_S}\right)} e^{i\pi\left(\frac{1}{\omega_S}-\frac{1}{\omega_B}\right)\Delta\omega}
\end{aligned} \tag{A.6}$$

Calculating this Fourier transform yields the correct term from equation (A.3). However, ad-hoc phase terms without immediately obvious mathematical reasons need to be introduced in the signal sum to achieve the desired output.

A.1.2 Hann Window

Let $x(t) = e^{i\omega_0 t}$ and $W(x) = \sin^2(\pi x) = \frac{1}{2}\big(1-\cos(2\pi x)\big)$. For the Hann window, obtaining a closed expression via evaluation of the DFT sum is harder. Fortunately, it turns out that the second approach, summing the contributions of each harmonic of the masked function does result in the correct DFT description:

$$\mathcal{F}\left[W(t)e^{i\omega_0 t}\right](\Delta\omega) = \left(\tfrac{1}{2}\delta(\Delta\omega) - \tfrac{1}{4}\delta(\Delta\omega-\omega_B) - \tfrac{1}{4}\delta(\Delta\omega+\omega_B)\right) \tag{A.7}$$

$$\mathcal{F}_{t\in[0,T]}\left[W(t)e^{i\omega_0 t}\right](\Delta\omega) = e^{-i\pi\frac{\Delta\omega}{\omega_B}}\left(\tfrac{1}{2}\operatorname{sinc}\left(\pi\tfrac{\Delta\omega}{\omega_B}\right) - \tfrac{1}{4}\operatorname{sinc}\left(\pi\tfrac{\Delta\omega}{\omega_B}-\pi\right) - \tfrac{1}{4}\operatorname{sinc}\left(\pi\tfrac{\Delta\omega}{\omega_B}+\pi\right)\right)$$

$$\begin{aligned}
&\mathcal{F}_{t\in\mathbb{R}/T\mathbb{Z}}\left[W(t)e^{i\omega_0 t}\right](\Delta\omega) \\
&= \sum_{k\in\mathbb{Z}} e^{-i\pi\frac{\Delta\omega+k\omega_S}{\omega_B}} \left(\tfrac{1}{2}\operatorname{sinc}\left(\pi\tfrac{\Delta\omega+k\omega_S}{\omega_B}\right) - \tfrac{1}{4}\operatorname{sinc}\left(\pi\tfrac{\Delta\omega+k\omega_S}{\omega_B}-\pi\right) - \tfrac{1}{4}\operatorname{sinc}\left(\pi\tfrac{\Delta\omega+k\omega_S}{\omega_B}+\pi\right)\right) \\
&= e^{-i\pi\frac{\Delta\omega}{\omega_B}} \cdot \frac{1}{2}\frac{\omega_B}{\omega_S} \sum_{k=-1}^{1} \left(\cos\left(\pi\left(\tfrac{\Delta\omega}{\omega_B}+k\right)\right) + \frac{\sin\left(\pi\left(\frac{\Delta\omega}{\omega_B}+k\right)\left(1-\frac{\omega_B}{\omega_S}\right)\right)}{\sin\left(\pi\left(\frac{\Delta\omega}{\omega_B}+k\right)\right)}\right)
\end{aligned} \tag{A.8}$$

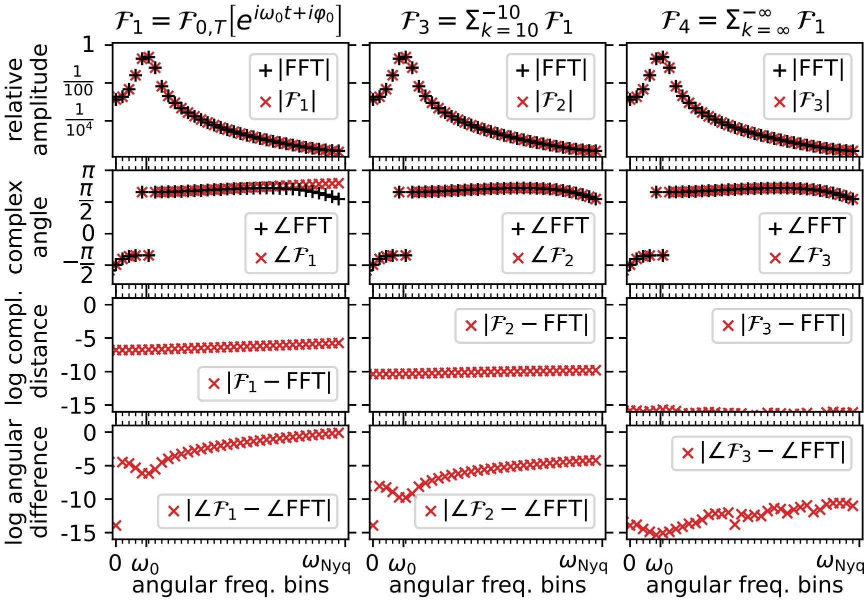

Figure A.2: Comparison of different DFT approximation approaches with the calculated DFT for the same sinusoidal signal as in Fig. A.1. As no ad hoc terms are needed, only the masked FT, and the superposition of 21 and ∞ harmonics (Eq. (A.8)) are shown from left to right. For both the rectangular and Hann window, each step increases the precision of the approximation, with the infinite sum theoretically being perfectly accurate, and numerically equal down to machine precision.

Similar to the rectangular window DFT, equation (A.8) contains only one complex oscillating term, whose constant magnitude is 1, and which can be removed for the calculation of the DFT magnitude. As the spectral response of the repeating Hann window is the sum of 3 dirac delta functions as shown in equation (A.7), the Hann window response can roughly be treated as a superposition of three rectangular window responses[1]. The infinite sum over all three components then leads to a three-term sum in Eq. (A.8).

A.2 Flat-Phase Windowing

As shown in Fig. 3.1, the phase readout of the signal frequency is strongly dependent on the signal detuning from the bin centre. The resulting phase variation is negligible if the signal frequency variation is small against the frequency-bin width ω_B. For the PT axial detector with a phase detection DFT length of 256 ms, the frequency widths are $\omega_B = 8\pi\,\mathrm{Hz}$ and $\sigma(\omega_z) \approx 0.1\,\mathrm{Hz}$, so the approximation holds well. In general,

[1] The oscillating $(-1)^k$ term in Eq. (A.6) when calculating the rectangular window DFT causes the resulting trigonometric terms to differ between the rectangular (A.6) and Hann window (A.8). DFTs of odd length N both change the spacing $\pi k \omega_S / \omega_B = \pi k N$ between the added sinc functions and the oscillation behaviour of the exponential terms, as $e^{i\pi k N_{\mathrm{even}}} = 1$, but $e^{i\pi k N_{\mathrm{odd}}} = (-1)^k$. Together, those effects cancel, whereas only one change would cause the trigonometric terms to trade places for even and odd length rectangular and Hann windows. See also `desmos.com/calculator/s527rcjg4f`.

however, one may wish to design a flat-phase window with small or no phase dependence on the signal detuning, analogous to the flat-top windows minimizing the amplitude dependence on the signal detuning. Yet, while flat-top windows are heavily optimized and widely used [90, 137], the same can not be said for flat-phase windows. This section will investigate how to potentially design such windows and the problems with their application.

Equation (A.3) states the dirichlet kernel-like rectangular window response $y(\Delta\omega)$ to any pure oscillation $e^{i\omega_0 t}$ purely in terms of the frequency difference $\Delta\omega = \omega - \omega_0$. Conversely, all possible sampled pure oscillations can be created by an inverse Fourier transform of $y(\omega)$, shifted by ω_0. The inverse Fourier transform of an arbitrary function will generally not create a periodic window of the correct length, so frequency space window design needs to consider time domain constraints. Since any finite and continuous function on a sampling domain can be realized as a sum of its Fourier components, with DFTs of $y(\Delta\omega)$ by the above argument, the inverse Fourier transform of the sum of shifted and scaled $y(\omega)$ allows the creation of any viable window function, yielding $c_k y(\omega - r_k)$ as a basis for the window design in frequency-space.

$$w(\omega) \coloneqq \mathcal{F}_t\big[W(t)\big](\omega) = \sum_{k\in K} c_k y(\omega - r_k) = \int_{-\infty}^{\infty} \underbrace{\left(\sum_{k\in K} \delta(\hat{\omega} - r_k)\right)}_{c(\hat{\omega})} y(\omega - \hat{\omega})\,\mathrm{d}\hat{\omega} \tag{A.1}$$

Here, $c_k \in \mathbb{C}$ and $r_k \in \mathbb{R}$, but the frequency shifts can be constrained further to $r_k \in \{0, \omega_B, \ldots, \omega_S/2 - \omega_B\}$ to enforce bijectivity between the window and the response coefficients. The rightmost term in Eq. (A.1) is the result of embedding the discrete choices for $\{r_k\}_{k\in K}$ into the whole of $\mathbb{R}$ by defining $c(\hat{\omega})$ as a sum of delta distributions. Using this formulation, the whole equation reduces to a convolution $w(\omega) = (c * y)(\omega)$. The rectangular window response $y(\omega)$ is given by Eq. (A.3), while $w(\omega)$ is the response of the to-be-optimized flat-phase window and is constrained by its requirements. Thus, $c(\omega)$ needs to be determined. Usage of the convolution theorem allows rearranging Eq. (A.1) into an explicit form to calculate $c(\omega)$.

$$\mathcal{F}_\omega^{-1}\big[w(\omega)\big](t) = \mathcal{F}_\omega^{-1}\big[(c * y)(\omega)\big](t) = \mathcal{F}_\omega^{-1}\big[c(\omega)\big](t) \cdot \mathcal{F}_\omega^{-1}\big[y(\omega)\big](t) \tag{A.2}$$

$$c(\omega) = \mathcal{F}_t\Big[\mathcal{F}_\omega^{-1}\big[w(\omega)\big](t) \,/\, \mathcal{F}_\omega^{-1}\big[y(\omega)\big](t)\Big](\omega) \tag{A.3}$$

With $c(\omega)$, $W(t)$ can then be calculated as $\mathcal{F}_\omega^{-1}\big[(c * y)(\omega)\big](t)$. However, already the calculation of $\mathcal{F}_\omega^{-1}\big[y(\omega)\big](t)$ is not feasible, as the inverse Fourier transform of the discrete Fourier transform of a signal is not the signal itself. Furthermore, $y(\omega)$ is dependent on $N = \omega_S / \omega_B$, and its inverse Fourier transform will be as well, making the window function dependent on the window length. Nevertheless, with $N \gg 1$, the dependence of $y(\omega)$ on increasing ω_S is small and leads to using $\omega_S \to \infty$ as a simplifying approximation, yielding Eq. (A.4),

$$\overline{y}(\omega) = \operatorname{sinc}\left(\pi \frac{\omega}{\omega_B}\right) e^{-i\pi \frac{\omega}{\omega_B}} \tag{A.4}$$

which is shown in Fig. A.3. It shows why optimising a window for a flat amplitude response is rather straightforward, with $\partial_\omega |\overline{y}(\omega)| = 0$ at $\omega = 0$ and varying only slowly inside the $\pm\omega_B/2$ range such that the sum of less than ten $c_k y(\omega - k\omega_B)$ yields sufficiently constant amplitudes. Conversely, $\angle\overline{y}(\omega)$ changes the fastest inside $\pm\omega_B/2$. Calculation of the inverse Fourier transform of Eq. (A.4) yields

$$\mathcal{F}_\omega^{-1}\left[\overline{y}(\omega)\right](t) = \frac{\omega_B}{\sqrt{2\pi}}\,\Pi^0_{-\frac{2\pi}{\omega_B}}(t) \tag{A.5}$$

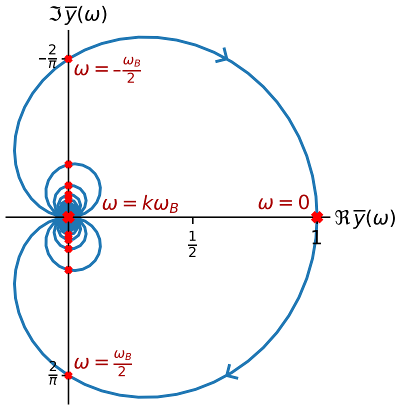

Figure A.3: The complex trace of $\overline{y}(\omega)$. Values of $\overline{y}(\omega)$ at half and integer detunings of ω_B are highlighted.

where $\Pi_A^B(x) \equiv 1$ on its support $x \in [A, B]$, and zero otherwise. Continuing to $w(\omega)$, a flat phase response requires that the phase variation $\partial_\omega \angle c(\omega)$ with respect to frequency detuning ω is zero at $\omega = 0$, and approximately zero over the central bin $\omega \in [-\omega_B/2, \omega_B/2]$. Furthermore, the amplitude $|w(\omega)|$ should be close to maximized in the central bin, as small amplitudes lead to low SNRs. Finally, the value of $w(\omega)$ should behave equivalently for positive and negative detuning with respect to amplitude and phase. Due to the inherent rotation of $w(\omega)$ by π in the central bin and 0 in all others used to possibly compensate, the design should aim for $w(-\omega) = w(\omega)^*$. The last constraint requires the support of w to be symmetrical around 0, while it must also be a subset of $[-\frac{2\pi}{\omega_B}, 0]$ for Eq. (A.3) to hold, making design via the convolution theorem impossible.

Returning to discrete sums of $\overline{y}(\omega)$, the phase sweep at $\omega = 0$ can be compensated by adding a scaled and frequency detuned $cy(\omega - r)$ such that the derivative of the sum vanishes at zero. Making use of $\partial_\omega\, cy(0-\omega) = \left(\partial_\omega\, cy(0+\omega)\right)^*$ allows enforcing symmetry by using

$$w_r(\omega) := \overline{y}(\omega) - \frac{c(r)}{2}\overline{y}(\omega - r) + \frac{c(r)^*}{2}\overline{y}(\omega + r),$$

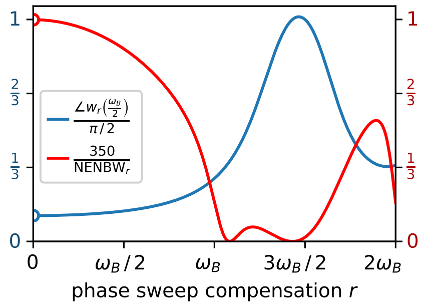

Figure A.4: Phase span in the central bin of $w_r(\omega)$ and time domain NENBW[2] of $W_r(t)$ depending on r.

shown in Fig. A.4, which also causes $W_r(t)$ to be real-valued. For $r \gtrsim 1.1$, the maximum power sidelobes move out of the central bin, while for $r \to 0$, both NENBW and central bin phase span are optimized, with additional compensation terms only worsening the window properties.

For $r \to 0$, $W_r(t) \rightsquigarrow C \cdot \left(2.57070t^2 - 3.42876t + 1\right)$, which is the best window achieved here, with a phase span of only 20° at the cost of an NENBW of more than 350.

[2] $\mathrm{NENBW} = \langle W_r^2\rangle / \langle W_r\rangle^2$, where $|w_r(0)| \propto \int_0^{2\pi/\omega_B} W_r(t)\,\mathrm{d}t \propto \langle W_r\rangle$.

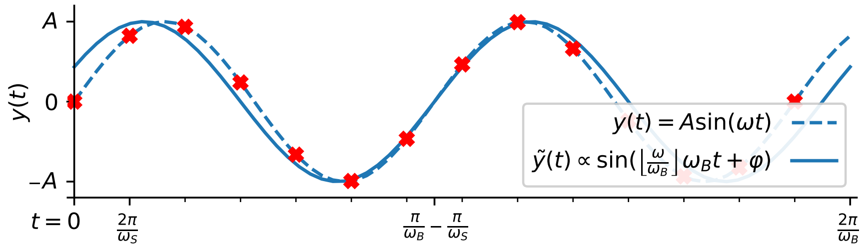

Figure A.5: The main frequency component $\tilde{y}(t)$ of a sinusoidal signal $y(t) \propto \sin(\omega t)$ incurs an initial phase shift φ dependent on the bin frequency detuning of ω.

A.2.1 Phase Compensation without Windowing

With flat-phase windowing being ineffective due to the loss in SNR, other ways must be found to include or compensate the frequency dependence of the measured phase into phase-sensitive measurements to fully understand the observed phase shifts.

Figure A.5 shows a function $y(t_k) = A\sin(\omega t_k)$ sampled at $t_k \in \frac{2\pi}{\omega_S}\{0, \ldots, N-1\}$. Its frequency ω is detuned upwards from one of the DFT bins $(2\omega_B)$, so a singular DFT frequency component is not enough to describe it. Still, the main frequency component $\tilde{y}(t) \propto \sin\big(\lfloor \omega/\omega_B \rfloor \omega_B t + \varphi\big)$ is used for the amplitude and phase determination. Since it minimizes the total phase error over the whole acquisition set $t \in 2k\pi/\omega_B$, the angles $\angle\, y(t_c)$ and $\angle\, \tilde{y}(t_c)$ are equal around $t_c = \pi/\omega_B - \pi/\omega_S$, while $\varphi := \angle\, \tilde{y}(0)$ is systematically shifted from $\angle\, y(0)$. The exact point of phase equality varies within $\pm\omega_B$ if ω is not close to the frequency space boundaries, which can be neglected for $N \gg 1$. This phase-error minimization effect is the cause of the frequency-dependent phase shifting by $180° \big/ \omega_B$ described in Fig. 3.1, and the $\exp\big(i\pi\big(\omega_S^{-1} - \omega_B^{-1}\big)\Delta\omega\big) = e^{it_c\Delta\omega}$ term in Eq. (A.3). If $y(t)$ is modulated, the phase optimization will be weighted with the signal envelope and thus biased towards times of high signal amplitude. For a decaying signal, phase equality occurs before t_c. While the shift cannot be compensated without prior knowledge of the bin detuning, the additional t_c until phase equality potentially can be.

As an example, for the detection of axial frequency ω_z shifts due to spin flips, the phase of the particle is evolved for t_{evo} until the spin-state dependent frequency splitting $\Delta\omega_z$ is reflected in the maximum possible phase difference π of the spin-up and spin-down measurements. As long as both $\omega_{z\uparrow\downarrow} = \omega_z \pm \frac{1}{2}\Delta\omega_z$ stay in the same bin, their phase at $t_{\mathrm{evo}} + t_c$ is given by φ up to a fixed constant c independently of bin detuning. Consequently, their phase difference is also bin detuning independent and can be used to determine $\Delta\omega_z$.

$$\Delta\varphi = \big(\varphi(\omega_{z\uparrow}) + c\big) - \big(\varphi(\omega_{z\downarrow}) + c\big) = \big(t_{\mathrm{evo}} + t_c\big)\big(\omega_{z\uparrow} - \omega_{z\downarrow}\big) = (t_{\mathrm{evo}} + t_c)\Delta\omega_z \qquad \text{(A.6)}$$

Since t_c is approximately half the DFT acquisition time, including the effects of a frequency-dependent DFT phase leads to an evolution time correction term most relevant for differential frequency measurements like state change detection, where the DFT acquisition is a significant part of the particle evolution time, and where the frequency is not determined from evolution time changes.

A.3 Frequency Estimation Python Implementation

```
import numpy as np
from uncertainties import correlated_values

# Φs/rad, ts/s, freq_guess/Hz, Approach 1 (False) or 2 (True)
def estimate_frequency_unwrapping(ts, Φs, freq_guess, phase_correction=True):
    # Use turns Υ = Φ/2  as the quantity to unwrap
    expected_Υ_increase = np.diff(ts).mean() * freq_guess
    Υs_unwrap = Φs.copy() / (2*np.pi)

    # How much does the measured increase dΥ in Υ deviate from the expected value?
    # increment dΥ until it deviates the min. possible amount from the expected dΥ
    for i, curr_phase in enumerate(Υs_unwrap[1:]):
        expected_Υ = Υs_unwrap[i] + expected_Υ_increase
        difference_from_expected = Υs_unwrap[i+1] - expected_Υ
        extra_Υs = int(round(difference_from_expected))
        Υs_unwrap[i+1:] -= extra_Υs

    # Find outlier pairs of dΥ as explained in the text, and remove them
    # while also correcting the potential effect on incorrect unwrapping
    if phase_correction:
        ΔΥs = np.diff(Υs_unwrap)
        ΔΥs -= np.median(ΔΥs)  # normalize as proxy for deviation from expected
        # detect the two relevant errors: [...,-1,1,...] and [...,1,1,...]
        conv_mask_shift, conv_mask_blip = [ 1/2, 1/2], [-1/2, 1/2]
        c = 1/4  # consider changes > pi/2 from median as potential errors
        cshift = np.convolve(ΔΥs, conv_mask_shift, mode="valid")
        cblip  = np.convolve(ΔΥs, conv_mask_blip,  mode="valid")
        total = np.where(np.abs(cshift) > np.abs(cblip), cshift, cblip)
        # select possible outliers and filter them depending on their neighbours
        abstot, contenders = np.abs(total), np.abs(total)>c
        for i,v in enumerate( abstot ):
            if   i==0            and v<abstot[i+1]: contenders[i] = False
            elif i==len(total)-1 and v<abstot[i-1]: contenders[i] = False
            elif v<abstot[i+1]     or v<abstot[i-1]: contenders[i] = False
        # blip: delete next datapoint; shift: also shift following +2pi
        filter_mask  = np.ones_like( ts, dtype=bool)
        filter_shift = np.zeros_like(ts, dtype=int)
        for i in np.arange(len(contenders))[contenders]:
            filter_mask[i+1] = False
            if np.abs(cshift[i]) > np.abs(cblip[i]):
                filter_shift[i+2:] += (-1 if cshift[i]>0 else 1)
        ts, Υs_unwrap = ts[filter_mask], (Υs_unwrap+filter_shift)[filter_mask]

    # linearly fit the the unwrapped turns, giving the frequency as the slope
    f, Υ0 = correlated_values(*np.polyfit(ts, Υs_unwrap, deg=1, cov=True))
    return f
```

Listing 1: Python implementation of the (misdetection corrected) phase unwrap algorithm.

```python
import numpy as np
from uncertainties import correlated_values
from scipy.optimize import least_squares

# Φs/rad, ts/s, freq_guess/Hz
def estimate_frequency_fft_fit(ts, Φs, freq_guess):
    # general optimization code with uncertainty/variance estimation
    # better than scipy.leastsq, but variance needs to be calculated manually
    def lsq_optimize(errorfunc, ddof, p0):
        opt = least_squares(errorfunc, x0=p0, xtol=1e-14)
        opt_popt, opt_pcov = opt["x"], np.linalg.inv(opt.jac.T.dot(opt.jac))
        opt_var = (errorfunc(opt_popt)**2).sum() / ddof # normally N-1 or so
        return correlated_values(opt_popt, opt_pcov * opt_var)

    # applies a DFT to the phase data, selecting the freq. bin with the highest power
    # that bin normally contains the correct frequency -> freq_guess improvement
    def calc_freq_fft(ts, C_Φs, freq_guess):
        freqs = np.fft.fftfreq(ts.shape[-1], d=np.diff(ts).mean())
        f_s, f_bw = 1/np.diff(ts).mean(), freqs[1]-freqs[0]
        dft_C_Φs = np.fft.fft(C_Φs)
        dftAs, dftΦs = np.abs(dft_C_Φs), np.angle(dft_C_Φs)
        max_dftAs_i = np.argmax(dftAs)
        f_wrapped, dftΦ_wrapped = freqs[max_dftAs_i], dftΦs[max_dftAs_i]
        # map aliased DFT frequency to unaliased value closest to freq_guess
        f_result = np.round((freq_guess - f_wrapped)/f_s)*f_s + f_wrapped
        return f_result, f_s, f_bw

    # fits a complex phase helix with phase & freq_guess to the measured complex phases
    # If |f_correct-freq_guess|<f_bw, and the phase guess is good, it correctly fits
    def calc_freq_fit(ts, C_Φs, freq_guess):
        norm_ts = ts - ts.mean()
        # euclidean distance between the guesses and data in the complex plane
        def gen_C_Φs(f, p): return np.exp(1j * (2*np.pi*f * norm_ts + p))
        def gen_C_ds(args): return np.abs(gen_C_Φs(*args) - C_Φs)
        # phase distance on the circle R/(2 pi Z)
        def gen_Φ_ds(args): return 2 * np.arcsin(gen_C_ds(args)/2)
        # Test 12 initial phases, guaranteeing up to three good guesses & choose best
        Φ_guesses = np.linspace(-np.pi, np.pi, 12, endpoint=False)
        errors = [sum(gen_Φ_ds((freq_guess, Φ_guess))**2) for Φ_guess in Φ_guesses]
        Φ_guess = Φ_guesses[np.argmin(errors)]
        # the phase fit is still normalized and doesn't correspond to the true phase!
        f_fit, norm_Φ_fit = lsq_optimize(gen_Φ_ds, len(C_Φs)-2, [freq_guess, Φ_guess])
        return f_fit

    ts, C_Φs_measured = ts, np.exp(1j * Φs)
    # improved initial frequency guess from DFT bin power maximum
    f_fft, f_sample, f_binwidth = calc_freq_fft(ts, C_Φs_measured, freq_guess)
    # best frequency estimate using improved DFT frequency guess as initial guess
    f_fit = calc_freq_fit(ts, C_Φs_measured, f_fft)
    return f_fit
```

Listing 2: Python implementation of the FFT-based direct complex fit algorithm.

Acknowledgements

Bela, you were more influential in the day-to-day progression of my thesis than anyone else. Your drive and optimism during the months we spent together, assembling, testing, programming, and repeatedly fixing things for *the final time*, were critical in implementing and optimizing phase methods at BASE. Good luck in optimizing the phase method sequence during the next shutdown. I could not have done it without you.

The same goes for the remainder of the 2024 BASE team, some ordered here by their increasing contribution to the totality of BASE (and thus my thesis) and the maximum stupidity of questions I was comfortable asking.

Julia, I've come to know you as a good friend over the years. You always had an open ear for any of my problems, both in and outside of work, and I hope that I may be able to offer you the same kindness and support in return. Being in the position of wroting one's thesis yourself, I hope you will prevail without too many issues.

Stefan Erlewein, you've been a great colleague as well. You chose to embrace all of my questions, even though you caught the brunt of them, some even work-related, always engaging in innumerable discussions. I will miss them, tangential as they may be, for sparking joy and interest throughout the year. I wish you good luck in whatever endeavors may await you after your time at BASE.

Christian and Barbara, you were my go-to for anything relevant, be it physics, electronics, or theory. Never really having any time to answer questions, you always made some anyway. And Barbara, even though they were sometimes meant half-jokingly, your constant expressions of conviction in my abilities gives me confidence in what I do.

Lastly, I want to specifically highlight Stefan Ulmer, the driving force behind the construction and continued development of the BASE experiment. Through you, I was able to work on a project that, besides being a critical improvement to the BASE apparatus, was also scoped to include manufacturing and assembly besides theory and simulations, happily allowing me to "touch stuff". Working on such an impressive experiment is an opportunity extended to only a few people, and I am thankful for being given the chance.

This thesis has been made possible by the financial support of RIKEN, the Erasmus+ traineeship program, and my parents. Without the support of Prof. Lutz Schweikhard, I would not have been able to participate in BASE as a student of the University of Greifswald, nor would I have correctly registered the project with the university.

List of Abbreviations

Acronym	Explanation
AC	Alternating Current
AD	Antiproton Decelerator
ADC	Analog Digital Converter
AEgIS	Antihydrogen Experiment: Gravity, Interferometry, Spectroscopy
ALPHA	Antihydrogen Laser PHysics Apparatus
ALPHA-g	ALPHA - g [Earth's gravitational acceleration]
ASACUSA	Atomic Spectroscopy And Collisions Using Slow Antiprotons
AT	Analysis Trap [BASE Penning Traps]
BASE	Baryon Antibaryon Symmetry Experiment
BASE-STEP	BASE - Symmetry Tests in Experiments with Portable antiprotons
BG	BackGround
CERN	Organisation Européenne pour la Recherche Nucléaire[3]
CPT	Charge Parity and Time symmetry
CT	Cooling Trap [BASE Penning Traps]
DC	Direct Current
DFT	Discrete Fourier Transform
DTFT	Discrete Time Fourier Transform
ELENA	Extra Low ENergy Antiproton ring
FFT	Fast Fourier Transform
GBAR	Gravitational Behaviour of Antimatter at Rest
ISOLDE	Isotope Separator On-Line DEvice
ISOLTrap	ISOLDE - Trap
JYFLTrap	Jyväskylän Yliopiston Fysiikan Laitos - Trap[4]
LINAC	LINear ACcelerator
LO	Local Oscillator signal
LS	Linear Spectrum [Signal Processing]
LSD	Linear Spectral Density [Signal Processing]
MIT	Massachusetts Institute of Technology

[4]European Organization for Nuclear Research (The Acronym CERN was kept after the original description of "Conseil Européen pour la Recherche Nucléaire" was retired.)

[4]University of Jyväskylä Department of Physics - Trap

Acronym	Explanation
NENBW	Normalized Equivalent Noise BandWidth
ODE	Ordinary Differential Equation
PC	Personal Computer
PDE	Partial Differential Equation
PM	Phase Methods
PnA	Pulse aNd Amplify
PnP	Pulse aNd Phase
p.p.b	Parts Per Billion [10^{-9}]
p.p.t	Parts Per Trillion [10^{-12}]
PS	Power Spectrum [Signal Processing]
PSD	Power Spectral Density [Signal Processing]
PT	Precision Trap [BASE Penning Traps]
PTER	Precision Trap Excitation Radial line
PUMA	antiProton Unstable Matter Annihilation
RF	Radio Frequency
RMS	Root Mean Square
RT	Reservoir Trap [BASE Penning Traps]
SB	SideBand
SHIPTrap	Separator for Heavy Ion reaction Products - Trap
SMILETrap	Stockholm-Mainz Ion LEvitation - Trap
SNR	Signal to Noise Ratio
TITAN	TRIUMFs Ion Trap for Atomic and Nuclear science
TR	Tuning Ratio
TRIUMF	TRI-University Meson Facility
TTL	Transistor-Transistor Logic
QED	Quantum ElectroDynamics

List of Mathematical Symbols

Subscript	Explanation (Category and Types)	
$0, 1, 2, 3, \ldots$	running index of Taylor coefficients and sequences	$[i]$
x, y, z, ρ, r	coordinate axis: x, y, z (axial), ρ (in-plane radial), r (total radial)	$[u]$
$c, +, -, z$	Penning trap mode: cyclotron, modified cyc., magnetron, axial	$[\mu]$
$p, \overline{p}, e, H^-$	particle type: proton, antiproton, electron, hydrogen ion	$[p]$
$t, p, \overline{p}$	electrical subcircuit: total, parallel RCL, particle	$[Z]$
S, N	electrical voltage trace: signal, noise	
S, B	DFT reference frequency: sampling, bin width	
δ, Δ	change of quantity: perturbative, macroscopic	
$0, *$	system or particle state: initial, excited	

Symbol	Explanation
a	acceleration
A_μ	oscillation amplitude
B	magnetic flux density in the Penning trap
B_i	Taylor coefficients of Penning trap $B(z)$
c	speed of light
c_i	arbitrary free coefficients
C_Z	capacitance
C_i	Taylor coefficients of Penning trap $E(z)$ from ring electrode
d	Penning trap electrode separation distance
D_Z	effective electrode distance of coupled Penning trap RCL resonator
D_i	Taylor coefficients of Penning trap $E(z)$ from correction electrodes
e	elementary charge
$\hat{e}_u$	unit coordinate vector
$E, \mathcal{E}$	electric field in the Penning trap
E_μ	Penning trap mode energies
E_i	Taylor coefficients of total Penning trap $E(z)$ from all electrodes

Symbol	Explanation
f	general frequency
f_C	cutoff frequency
$f_{D,R}$	dip frequency, RCL resonator frequency
f_Ω	linear Rabi frequency
g	g-factor, Earth's gravitational acceleration
$\hbar$	reduced Planck constant
i	imaginary unit
I_Z	current
k_B	Boltzmann constant
L	phase sequence length
L_Z	inductance
$L_{R,C}$	lengths of the central ring electrode, correction electrode
m_p	particle mass [normally $1m_p$]
n, N	natural number amount or quantum number
$\mathcal{N}$	NENBW
P_exc	excitation power
$\mathcal{P}$	probability density function
Q_Z	RCL resonator quality factor
R	Penning trap electrode radius
R_Z	resistance
S	phase sequence subsampling factor
t	time
$t_\mathrm{evo,exc,couple}$	PM evolutiom, excitation and coupling time
T	oscillation period, measurement/acquisition time
$T_{\mu,\mathrm{Bg}}$	mode temperature, electrical background temperature
TR	tuning ratio
$u_\mathrm{th,n}$	thermal noise, total noise random variables
v_D	magnetron drift velocity due to $E \times B$
$V_{R,C}$	Penning trap voltage of the central ring electrode, correction electrode
W, Z	Boson types
q_p	particle charge [normally $+1e$]
Z_Z	impedance
$Z, \hat{z}$	maximum axial amplitude
γ	Euler–Mascheroni constant
γ_μ	damping coefficient
δ	frequency detuning, width of following quantity, modifier
ϵ	perturbative scaling term
ε_{xz}	RF mode coupling strength
η, ξ	temporary placeholder variable
η_μ	mode coupling normalization factor
κ	Penning trap RCL resonator tap fraction
Λ	absolute amplitude in phase space
μ_p	particle magnetic dipole moment

Symbol	Explanation
μ_B	Bohr magneton
μ_N	nuclear magneton
σ	standard deviation or spread
$\tau_{A,E}$	exponential decay time of the amplitude, energy
φ	real phase in $[0, 2\pi)$
$\tilde{\varphi}$	unwrapped real phase in $\mathbb{R}^+$
ϕ	complex phase in $\exp(i \cdot [0, 2\pi))$
Φ	electric potential in the Penning trap
Φ_R	electric potential in the Penning trap with active RF drive
Φ_i	Taylor coefficients of Penning trap $\Phi(z)$
ω	general angular frequency
$\tilde{\omega}, \omega_\mathrm{Res}$	Penning trap RCL resonator resonance frequency
$\omega_{\mu,p}$	angular frequency of mode, signal, or system
ω_L	Larmor Frequency of spin precession
Ω	mode coupling Rabi frequency (resonant and tuned)
$\Omega', \Omega'', \Omega'''$	general tuned mode coupling Rabi frequency
ϖ	general detuned mode coupling Rabi frequency
$\angle$	angle of the following quantity

Bibliography

[1] Particle Data Group et al. "Review of particle physics". In: *Progress of theoretical and experimental physics* 2022.8 (2022).

[2] Steven Weinberg. "A model of leptons". In: *Physical review letters* 19.21 (1967), p. 1264.

[3] Tatsumi Aoyama et al. "Tenth-Order QED Contribution to the Electron $g-2$ and an Improved Value of the Fine Structure Constant". In: *Phys. Rev. Lett.* 109 (11 Sept. 2012). URL: https://link.aps.org/doi/10.1103/PhysRevLett.109.111807.

[4] Tatsumi Aoyama et al. "Complete Tenth-Order QED Contribution to the Muon $g-2$". In: *Phys. Rev. Lett.* 109 (11 Sept. 2012). URL: https://link.aps.org/doi/10.1103/PhysRevLett.109.111808.

[5] C Smorra et al. "A parts-per-billion measurement of the antiproton magnetic moment". In: *Nature* 550.7676 (2017), pp. 371–374.

[6] MJ Borchert et al. "A 16-parts-per-trillion measurement of the antiproton-to-proton charge–mass ratio". In: *Nature* 601.7891 (2022), pp. 53–57.

[7] X. Fan et al. "Measurement of the Electron Magnetic Moment". In: *Phys. Rev. Lett.* 130 (7 Feb. 2023). URL: https://link.aps.org/doi/10.1103/PhysRevLett.130.071801.

[8] M Ahmadi et al. "Characterization of the 1S–2S transition in antihydrogen". In: *Nature* 557.7703 (2018), pp. 71–75.

[9] G Graff et al. "Method for measuring the cyclotron and spin resonance of free electrons". In: *Physical Review Letters* 21.6 (1968), p. 340.

[10] John R. Ellis. *Limits of the Standard Model*. Tech. rep. Geneva: CERN, 2002. URL: https://cds.cern.ch/record/591472.

[11] Takehiko Asaka and Mikhail Shaposhnikov. "The νMSM, dark matter and baryon asymmetry of the universe". In: *Physics Letters B* 620.1-2 (2005), pp. 17–26.

[12] Hitoshi Murayama. "Physics beyond the standard model and dark matter". In: *Les Houches*. Vol. 86. Elsevier, 2007, pp. 287–347.

[13] CH Storry. "ATRAP antihydrogen experiments and update". In: *TCP 2006: Proceedings of the 4th International Conference on Trapped Charged Particles and Fundamental Physics (TCP 2006) held in Parksville, Canada, 3–8 September, 2006*. Springer. 2007, pp. 91–96.

[14] E Widmann and ASACUSA Collaboration. "Testing CPT symmetry with antiprotonic helium and antihydrogen". In: *AIP Conference Proceedings*. Vol. 1441. 1. American Institute of Physics. 2012, pp. 546–548.

[15] J Morgner et al. "Stringent test of QED with hydrogen-like tin". In: *Nature* 622.7981 (2023), pp. 53–57.

[16] MEA Amoretti et al. "Production and detection of cold antihydrogen atoms". In: *Nature* 419.6906 (2002), pp. 456–459.

[17] D Wineland, Phil Ekstrom, and Hans Dehmelt. "Monoelectron oscillator". In: *Physical review letters* 31.21 (1973), p. 1279.

[18] Robert S Van Dyck, Paul B Schwinberg, and Hans G Dehmelt. "Electron magnetic moment from geonium spectra". In: *New Frontiers in High-Energy Physics* (1978), pp. 159–181.

[19] G Gräff, H Kalinowsky, and J Traut. "A direct determination of the proton electron mass ratio". In: *Zeitschrift für Physik A Atoms and Nuclei* 297 (1980), pp. 35–39.

[20] Wayne M. Itano and D. J. Wineland. "Precision measurement of the ground-state hyperfine constant of $^{25}\mathrm{Mg}^{+}$". In: *Phys. Rev. A* 24 (3 Sept. 1981), pp. 1364–1373. DOI: 10.1103/PhysRevA.24.1364. URL: https://link.aps.org/doi/10.1103/PhysRevA.24.1364.

[21] W. Neuhauser et al. "Localized visible Ba^{+} mono-ion oscillator". In: *Phys. Rev. A* 22 (3 Sept. 1980), pp. 1137–1140. DOI: 10.1103/PhysRevA.22.1137. URL: https://link.aps.org/doi/10.1103/PhysRevA.22.1137.

[22] Masaki Hori et al. "Two-photon laser spectroscopy of antiprotonic helium and the antiproton-to-electron mass ratio". In: *Nature* 475.7357 (2011), pp. 484–488.

[23] EK Anderson et al. "Observation of the effect of gravity on the motion of antimatter". In: *Nature* 621.7980 (2023), pp. 716–722.

[24] J Biesheuvel et al. "Probing QED and fundamental constants through laser spectroscopy of vibrational transitions in HD+". In: *Nature communications* 7.1 (2016), p. 10385.

[25] Gerald Gabrielse et al. "Precision mass spectroscopy of the antiproton and proton using simultaneously trapped particles". In: *Physical Review Letters* 82.16 (1999), p. 3198.

[26] A Mooser et al. "Direct high-precision measurement of the magnetic moment of the proton". In: *Nature* 509.7502 (2014), pp. 596–599.

[27] S A Baird et al. *Design study of the antiproton decelerator: AD*. Tech. rep. CERN, 1996. DOI: 10.17181/CERN.KNXM.AYKR. URL: https://cds.cern.ch/record/317704.

[28] Stefan Ulmer. "First observation of spin flips with a single proton stored in a cryogenic Penning trap". Dissertation. Ruprecht-Karls-Universität Heidelberg, Germany, 2011. URL: https://hdl.handle.net/11858/00-001M-0000-000F-3E10-4.

[29] Sven Sturm et al. "The ALPHATRAP experiment". In: *The European Physical Journal Special Topics* 227 (2019), pp. 1425–1491.

[30] Antonia Schneider et al. "A Novel Penning-Trap Design for the High-Precision Measurement of the 3He2+ Nuclear Magnetic Moment". In: *Annalen der Physik* 531.5 (2019), p. 1800485.

[31] Antonia Schneider et al. "Direct measurement of the 3He+ magnetic moments". In: *Nature* 606.7916 (2022), pp. 878–883.

[32] Julia Repp et al. "PENTATRAP: a novel cryogenic multi-Penning-trap experiment for high-precision mass measurements on highly charged ions". In: *Applied Physics B* 107 (2012), pp. 983–996.

[33] Rima Xenia Schüssler et al. "Detection of metastable electronic states by Penning trap mass spectrometry". In: *Nature* 581.7806 (2020), pp. 42–46.

[34] Moisés Medina Restrepo and Edmund G Myers. "Mass difference of tritium and helium-3". In: *Physical Review Letters* 131.24 (2023), p. 243002.

[35] Edmund G Myers. "CPT tests with the antihydrogen molecular ion". In: *Physical Review A* 98.1 (2018), p. 010101.

[36] Michael P. Bradley et al. "Penning Trap Measurements of the Masses of ^{133}Cs, $^{87,85}Rb$, and ^{23}Na with Uncertainties ≤ 0.2 ppb". In: *Phys. Rev. Lett.* 83 (22 Nov. 1999), pp. 4510–4513. URL: https://link.aps.org/doi/10.1103/PhysRevLett.83.4510.

[37] E Minaya Ramirez et al. "Recent developments for high-precision mass measurements of the heaviest elements at SHIPTRAP". In: *Nucl. Instrum. Methods Phys. Res. B* 317 (2013), pp. 501–505.

[38] Tommi Eronen et al. "JYFLTRAP: a Penning trap for precision mass spectroscopy and isobaric purification". In: *Three decades of research using IGISOL technique at the University of Jyväskylä* (2014), pp. 61–81.

[39] I. Bergström et al. "SMILETRAP—A Penning trap facility for precision mass measurements using highly charged ions". In: *Nucl. Instrum. Methods Phys. Res. A* 487.3 (2002), pp. 618–651. ISSN: 0168-9002. URL: https://www.sciencedirect.com/science/article/pii/S0168900201021787.

[40] Sz Nagy et al. "High-precision mass measurements for fundamental applications using highly-charged ions with SMILETRAP". In: *Journal of Physics: Conference Series*. Vol. 58. 1. IOP Publishing. 2007, p. 109.

[41] J Dilling et al. "The proposed TITAN facility at ISAC for very precise mass measurements on highly charged short-lived isotopes". In: *Nucl. Instrum. Methods Phys. Res. B* 204 (2003), pp. 492–496.

[42] AT Gallant et al. "Mass determination near N= 20 for Al and Na isotopes". In: *Physical Review C* 96.2 (2017), p. 024325.

[43] M Mukherjee et al. "ISOLTRAP: An on-line Penning trap for mass spectrometry on short-lived nuclides". In: *The European Physical Journal A* 35 (2008), pp. 1–29.

[44] N. A. Althubiti et al. "Spectroscopy of the long-lived excited state in the neutron-deficient nuclides Po 195,197,199 by precision mass measurements". In: *Physical Review C* 96.4 (Oct. 2017), p. 044325.

[45] R Catherall et al. "The ISOLDE facility". In: *Journal of Physics G: Nuclear and Particle Physics* 44.9 (2017), p. 094002.

[46] M. Hori and J. Walz. "Physics at CERN's Antiproton Decelerator". In: *Progress in Particle and Nuclear Physics* 72 (2013), pp. 206–253. ISSN: 0146-6410. DOI: https://doi.org/10.1016/j.ppnp.2013.02.004. URL: https://www.sciencedirect.com/science/article/pii/S0146641013000069.

[47] Patrice Perez et al. "The GBAR antimatter gravity experiment". In: *Hyperfine Interactions* 233 (2015), pp. 21–27.

[48] G Yu Drobychev et al. *Proposal for the AEGIS experiment at the CERN antiproton decelerator (Antimatter Experiment: Gravity, Interferometry, Spectroscopy)*. Tech. rep. Geneva: CERN, 2007. URL: https://cds.cern.ch/record/1037532.

[49] R. Akbari et al. "The ALPHA-2 apparatus - facilitating experimentation with trapped antihydrogen". In: *Nucl. Instrum. Methods Phys. Res. A* 1072 (2025), p. 170194. ISSN: 0168-9002. URL: www.sciencedirect.com/science/article/pii/S0168900224011203.

[50] TA Tanaka et al. "Design of a microwave spectrometer for high-precision lamb shift spectroscopy of antihydrogen atoms". In: *Interactions* 245.1 (2024), p. 30.

[51] E Widmann et al. "Hyperfine spectroscopy of hydrogen and antihydrogen in ASACUSA". In: *Hyperfine Interactions* 240 (2019), pp. 1–7.

[52] Lowell S Brown. "Geonium lineshape". In: *Annals of Physics* 159.1 (1985), pp. 62–98.

[53] Lowell S Brown and Gerald Gabrielse. "Geonium theory: Physics of a single electron or ion in a Penning trap". In: *Reviews of Modern Physics* 58.1 (1986), p. 233.

[54] Christian Smorra et al. "BASE–the baryon antibaryon symmetry experiment". In: *The European Physical Journal Special Topics* 224 (2015), pp. 3055–3108. URL: https://link.springer.com/article/10.1140/epjst/e2015-02607-4.

[55] S. Ulmer et al. *BASE - Annual Report 2024*. Tech. rep. Geneva: CERN, 2025. URL: https://cds.cern.ch/record/2923879.

[56] C Smorra et al. *Technical Design Report of BASE-STEP*. Tech. rep. Geneva: CERN, 2021. URL: https://cds.cern.ch/record/2756508.

[57] Christian Smorra et al. "Proton Transport from the Antimatter Factory of CERN". In: *under Review at Nature* (2024).

[58] Georg Schneider et al. "Double-trap measurement of the proton magnetic moment at 0.3 parts per billion precision". In: *Science* 358.6366 (2017), pp. 1081–1084. URL: www.science.org/doi/abs/10.1126/science.aan0207.

[59] Stefan Ulmer et al. "High-precision comparison of the antiproton-to-proton charge-to-mass ratio". In: *Nature* 524.7564 (2015), pp. 196–199.

[60] James K Thompson, Simon Rainville, and David E Pritchard. "Cyclotron frequency shifts arising from polarization forces". In: *Nature* 430.6995 (2004), pp. 58–61.

[61] AK Bhatia and RJ Drachman. "Polarizability of helium and the negative hydrogen ion". In: *Journal of Physics B: Atomic, Molecular and Optical Physics* 27.7 (1994), p. 1299.

[62] Christian G Parthey et al. "Improved measurement of the hydrogen 1 s–2 s transition frequency". In: *Physical review letters* 107.20 (2011), p. 203001.

[63] S Ulmer et al. *Direct High-Precision Measurement of the g-Factor of a Single Antiproton Stored in a Cryogenic Penning Trap*. Tech. rep. Geneva: CERN, 2012. URL: https://cds.cern.ch/record/1455847.

[64] Christian Smorra et al. "Observation of individual spin quantum transitions of a single antiproton". In: *Physics Letters B* 769 (2017), pp. 1–6.

[65] Barbara M Latacz et al. "BASE—high-precision comparisons of the fundamental properties of protons and antiprotons". In: *The European Physical Journal D* 77.6 (2023), p. 94.

[66] G Gabrielse and J Tan. "Self-shielding superconducting solenoid systems". In: *Journal of Applied Physics* 63.10 (1988), pp. 5143–5148.

[67] Stefan Ulmer. *BASE Annual Report 2018*. Tech. rep. Geneva: CERN, 2019. URL: https://cds.cern.ch/record/2654098.

[68] Stefan Erlewein. "Implementation of a superconducting shimming and shielding system in the BASE experiment". Dissertation. Heidelberg University, Germany, 2024. URL: https://ub.uni-heidelberg.de/archiv/35326.

[69] Samuel Earnshaw. "On the nature of the molecular forces which regulate the constitution of the luminiferous ether". In: *Transactions of the Cambridge Philosophical Society* 7 (1848), p. 97.

[70] Chuanjun Huang and Laifeng Li. "Magnetic confinement fusion: a brief review". In: *Frontiers in Energy* 12.2 (June 1, 2018). ISSN: 2095-1698. URL: https://doi.org/10.1007/s11708-018-0539-1.

[71] Wolfgang Paul and Helmut Steinwedel. "Ein neues Massenspektrometer ohne Magnetfeld". In: *Zeitschrift für Naturforschung A* 8.7 (1953), pp. 448–450.

[72] D. J. Wineland and H. G. Dehmelt. "Principles of the stored ion calorimeter". In: *Journal of Applied Physics* 46.2 (Feb. 1975), pp. 919–930. ISSN: 0021-8979. URL: https://doi.org/10.1063/1.321602.

[73] Ekkehard Peik. *High-accuracy optical clocks with trapped ions*. May 2016. URL: https://www.euramet.org/research-innovation/search-research-projects/details/project/high-accuracy-optical-clocks-with-trapped-ions.

[74] Colin D Bruzewicz et al. "Trapped-ion quantum computing: Progress and challenges". In: *Applied Physics Reviews* 6.2 (2019).

[75] Ulrich Stroth. *Plasmaphysik*. Springer, 2011, pp. 17–20. ISBN: 978-3-662-55236-0.

[76] Lowell S. Brown and Gerald Gabrielse. "Precision spectroscopy of a charged particle in an imperfect Penning trap". In: *Phys. Rev. A* 25 (4 Apr. 1982), pp. 2423–2425. URL: https://link.aps.org/doi/10.1103/PhysRevA.25.2423.

[77] L. Schweikhard et al. "The trapping condition and a new instability of the ion motion in the ion cyclotron resonance trap". In: *International Journal of Mass Spectrometry and Ion Processes* 141.1 (1995), pp. 77–90. ISSN: 0168-1176. DOI: https://doi.org/10.1016/

0168-1176(94)04092-L. URL: https://www.sciencedirect.com/science/article/pii/016811769404092L.

[78] G Gabrielse, L Haarsma, and SL Rolston. "Open-endcap Penning traps for high precision experiments". In: *International Journal of Mass Spectrometry and Ion Processes* 88.2-3 (1989), pp. 319–332.

[79] Ino Ahrens. "Understanding the Limits of the BASE Antiproton Spin State Analysis Trap". (unpublished). Bachelor's Thesis. HHU Düsseldorf, Germany, 2024.

[80] Matthias Borchert. "Challenging the Standard Model by high precision comparisons of the fundamental properties of antiprotons and protons". Dissertation. Gottfried Wilhelm Leibniz University Hannover, Germany, 2021. URL: https://repo.uni-hannover.de/handle/123456789/11655.

[81] Georg Schneider. "300 ppt Measurement of the Proton g-Factor". Dissertation. Johannes Gutenberg-University Mainz, Germany, Dec. 2017. URL: https://openscience.ub.uni-mainz.de/server/api/core/bitstreams/4b84bd7c-fd1b-47e6-a935-6555333d4509/content.

[82] Sven Sturm et al. "Phase-Sensitive Cyclotron Frequency Measurements at Ultralow Energies". In: *Phys. Rev. Lett.* 107 (14 Sept. 2011), p. 143003. URL: https://link.aps.org/doi/10.1103/PhysRevLett.107.143003.

[83] Rima Xenia Schüßler. "First High-Precision Mass Measurements at PENTATRAP on highly charged Xe and Re ions". Dissertation. Heidelberg University, Germany, Dec. 2019. URL: https://archiv.ub.uni-heidelberg.de/volltextserver/27646/.

[84] Jochen Ketter et al. "First-order perturbative calculation of the frequency-shifts caused by static cylindrically-symmetric electric and magnetic imperfections of a Penning trap". In: *International Journal of Mass Spectrometry* 358 (2014).

[85] Fouad G Major, Viorica N Gheorghe, and Günter Werth. *Charged particle traps: physics and techniques of charged particle field confinement*. Vol. 37. Springer Science & Business Media, 2005.

[86] Hiroki Nagahama. "High-Precision Measurements of the Fundamental Properties of the Antiproton". Dissertation. University of Tokyo, Japan, 2017. URL: https://inspirehep.net/files/4c752b24721bbfec607cc82013b70c28.

[87] Markus Fleck. "Towards a Tenfold Improvement on the Measurement of the Antiproton Magnetic Moment". Dissertation. University of Tokyo, Japan, 2022.

[88] Ian Hickman. *Analog Electronics: Analog Circuitry Explained*. Newnes, 2013. ISBN: 978-1483129860.

[89] Harry Nyquist. "Thermal agitation of electric charge in conductors". In: *Physical review* 32.1 (1928), p. 110.

[90] Gerhard Heinzel, Albrecht Rüdiger, and Roland Schilling. "Spectrum and spectral density estimation by the Discrete Fourier transform (DFT), including a comprehensive list of window functions and some new flat-top windows". In: Feb. 15, 2002.

[91] Alan Sokal. *Introduction to Perturbation Theory*. Feb. 2024. URL: https://www.ucl.ac.uk/~ucahad0/0054_handout_10.pdf.

[92] M. Hussey. *Fundamentals of Mechanical Vibrations*. Macmillan, 1983. ISBN: 9780333324363. URL: https://books.google.ch/books?id=yRtEAQAAIAAJ.

[93] Herbert B. Callen and Theodore A. Welton. "Irreversibility and Generalized Noise". In: *Phys. Rev.* 83 (1 July 1951), pp. 34–40. URL: https://link.aps.org/doi/10.1103/PhysRev.83.34.

[94] *SR780 User's Manual*. Stanford Research Systems. July 2014. URL: https://www.thinksrs.com/downloads/pdfs/manuals/SR780m.pdf.

[95] Brian Richard D'Urso. "Cooling and self-excitation of a one-electron oscillator". Dissertation. Harvard University, 2003. URL: https://cfp.physics.northwestern.edu/documents/2003_Durso_Brian.pdf.

[96] Jost Herkenhoff et al. "A digital feedback system for advanced ion manipulation techniques in Penning traps". In: *Review of Scientific Instruments* 92.10 (2021).

[97] Eric A Cornell et al. "Mode coupling in a Penning trap: π pulses and a classical avoided crossing". In: *Physical Review A* 41.1 (1990), p. 312.

[98] Martin Kretzschmar. "A quantum mechanical model of Rabi oscillations between two interacting harmonic oscillator modes and the interconversion of modes in a Penning trap". In: *AIP Conference Proceedings*. Vol. 457. 1. American Institute of Physics. 1999, pp. 242–251.

[99] S. Eliseev et al. "Octupolar-Excitation Penning-Trap Mass Spectrometry for Q-Value Measurement of Double-Electron Capture in ^{164}Er". In: *Phys. Rev. Lett.* 107 (15 Oct. 2011), p. 152501. URL: https://link.aps.org/doi/10.1103/PhysRevLett.107.152501.

[100] Daniel Zeuch et al. "Exact rotating wave approximation". In: *Annals of Physics* 423 (2020), p. 168327. ISSN: 0003-4916. DOI: https://doi.org/10.1016/j.aop.2020.168327. URL: https://www.sciencedirect.com/science/article/pii/S000349162030261X.

[101] *Instruction-based control & qubit characterization*. Oct. 2024. URL: https://www.quantum-machines.co/solutions/superconducting-qubits.

[102] Yicheng Wu, Manoj Kumar Sharma, and Ashok Veeraraghavan. "WISH: wavefront imaging sensor with high resolution". In: *Light: Science & Applications* 8.1 (May 1, 2019). Number: 1 Publisher: Nature Publishing Group, p. 44. ISSN: 2047-7538. URL: https://www.nature.com/articles/s41377-019-0154-x (visited on 01/10/2024).

[103] Juan Martinez-Carranza, Konstantinos Falaggis, and Tomasz Kozacki. "Fast and accurate phase-unwrapping algorithm based on the transport of intensity equation". In: *Appl. Opt.* 56.25 (Sept. 2017), pp. 7079–7088. URL: https://opg.optica.org/ao/abstract.cfm?URI=ao-56-25-7079.

[104] A. Schubert et al. "Extraction of surface topography from SAR stereo pairs using an airborne X-band sensor: preliminary results". In: *Retrieval of Bio- and Geo-Physical Parameters from SAR Data for Land Applications*. Ed. by A. Wilson and S. Quegan. Vol. 475. ESA Special Publication. Jan. 2002, pp. 151–156.

[105] Robby G. Mckilliam et al. "Frequency estimation by phase unwrapping". English. In: *IEEE Transactions on Signal Processing* 58.6 (June 2010), pp. 2953–2963. ISSN: 1053-587X. DOI: 10.1109/TSP.2010.2045786.

[106] Richard M Goldstein, Howard A Zebker, and Charles L Werner. "Satellite radar interferometry: Two-dimensional phase unwrapping". In: *Radio science* 23.4 (1988), pp. 713–720.

[107] C.E. Shannon. "Communication in the Presence of Noise". In: *Proceedings of the IRE* 37.1 (1949), pp. 10–21. DOI: 10.1109/JRPROC.1949.232969.

[108] H. Nyquist. "Certain Factors Affecting Telegraph Speed". In: *Transactions of the American Institute of Electrical Engineers* XLIII (1924), pp. 412–422. DOI: 10.1109/T-AIEE.1924.5060996.

[109] Johannes Thomae. *Einleitung in die Theorie der bestimmten Integrale: von Joh. Thomae*. Nebert, 1875.

[110] Jorge J Moré. "The Levenberg-Marquardt algorithm: implementation and theory". In: *Numerical analysis: proceedings of the biennial Conference held at Dundee, June 28–July 1, 1977*. Springer. 2006, pp. 105–116.

[111] Pauli Virtanen et al. "SciPy 1.0: Fundamental Algorithms for Scientific Computing in Python". In: *Nature Methods* 17 (2020), p. 261. DOI: 10.1038/s41592-019-0686-2.

[112] R Bartolini et al. “Precise measurement of the betatron tune”. In: *Part. Accel.* 55 (1996), pp. 1–10.

[113] Jacques Laskar, Claude Froeschlé, and Alessandra Celletti. “The measure of chaos by the numerical analysis of the fundamental frequencies. Application to the standard mapping”. In: *Physica D: Nonlinear Phenomena* 56 (1992), pp. 253–269. URL: https://api.semanticscholar.org/CorpusID:120448200.

[114] S. Miller and D. Childers. *Probability and Random Processes: With Applications to Signal Processing and Communications*. Elsevier Science & Technology Books, 2004. ISBN: 9781493300266. URL: https://books.google.ch/books?id=eXsfogEACAAJ.

[115] *Spectrum Analyzer Measurements and Noise, Application Note 1303*. Hewlett Packard. Aug. 5, 1998. URL: https://g8fek.com/uploads/9/4/4/3/94435411/hp_sa_and_noise_5966-4008e_an_1303.pdf.

[116] Fabienne Landua. *The CERN accelerator complex layout in 2022*. General Photo. URL: https://cds.cern.ch/record/2813716.

[117] *The Antiproton Decelerator*. Nov. 2024. URL: https://www.home.cern/science/accelerators/antiproton-decelerator.

[118] Ana Lopez. *New antimatter gravity experiments begin at CERN*. Nov. 2018. URL: https://www.home.cern/news/news/experiments/new-antimatter-gravity-experiments-begin-cern.

[119] Ana Lopez. *CERN approves two new experiments to transport antimatter*. Mar. 2021. URL: https://www.home.cern/news/news/physics/cern-approves-two-new-experiments-transport-antimatter.

[120] T Aumann et al. *PUMA: antiprotons and radioactive nuclei*. Tech. rep. Geneva: CERN, 2019. URL: https://cds.cern.ch/record/2691045.

[121] Vinod Chohan et al. *Extra Low ENergy Antiproton (ELENA) ring and its Transfer Lines: Design Report*. Tech. rep. CERN, July 2014.

[122] Barbara M Latacz et al. “Ultra-thin polymer foil cryogenic window for antiproton deceleration and storage”. In: *Review of Scientific Instruments* 94.10 (2023).

[123] Christian Smorra et al. “A reservoir trap for antiprotons”. In: *International Journal of Mass Spectrometry* 389 (2015), pp. 10–13.

[124] DS Hall and G Gabrielse. “Electron cooling of protons in a nested Penning trap”. In: *Physical review letters* 77.10 (1996), p. 1962.

[125] CH Tseng and G Gabrielse. “One-electron parametric oscillator”. In: *Applied Physics B* 60 (1995), pp. 95–102.

[126] Ivana Kovacic, Richard Rand, and Si Mohamed Sah. “Mathieu’s equation and its generalizations: overview of stability charts and their features”. In: *Applied Mechanics Reviews* 70.2 (2018), p. 020802.

[127] S. Navas et al. “Review of particle physics”. In: *Phys. Rev. D* 110.3 (2024), p. 030001. DOI: 10.1103/PhysRevD.110.030001.

[128] Michael Anbar and Rafael Schnitzer. “Doubly Charged Negative Atomic Ions of Hydrogen”. In: *Science* 191.4226 (1976), pp. 463–464. URL: https://science.org/doi/abs/10.1126/science.191.4226.463.

[129] B. M. Latacz et al. “Orders of Magnitude Improved Cyclotron-Mode Cooling for Nondestructive Spin Quantum Transition Spectroscopy with Single Trapped Antiprotons”. In: *Phys. Rev. Lett.* 133 (5 Aug. 2024), p. 053201. URL: https://link.aps.org/doi/10.1103/PhysRevLett.133.053201.

[130] Philip Geissler. *RISE DAAD Project Notes, Production of new E-gun tips. E-gun: electron field emission gun*. Tech. rep. CERN, 2021. URL: https://cds.cern.ch/record/2918065.

[131] S Ulmer et al. “A cryogenic detection system at 28.9 MHz for the non-destructive observation of a single proton at low particle energy”. In: *Nucl. Instrum. Methods Phys. Res. A* 705 (2013), pp. 55–60.

[132] Radha Setty. *I&Q Mixers, Image Reject Down-Conversion & Single Sideband (SSB) Up-Conversion*. Nov. 2022. URL: https://blog.minicircuits.com/iq-mixers-image-reject-down-conversion-single-sideband-ssb-up-conversion/.

[133] *IEEE Standard Codes, Formats, Protocols, and Common Commands For Use with ANSI/-IEEE Std 488.1-1987 IEEE Standard Digital Interface for Programmable Instrumentation*. Section 11. IEEE. 1988. URL: https://ieeexplore.ieee.org/document/19528.

[134] Sophocles Orfanidis. *Applied Optimum Signal Processing*. http://eceweb1.rutgers.edu/~orfanidi/aosp//index.html. self-published, 2018, pp. 631–633.

[135] Philip Geissler. *Varactor Boards, HV Connections & BASE Upkeep*. 2022. URL: https://cds.cern.ch/record/2827408.

[136] Sven Sturm et al. “High-precision measurement of the atomic mass of the electron”. In: *Nature* 506.7489 (2014), pp. 467–470.

[137] To Tran, Ingvar Claesson, and Mattias Dahl. “Design and Improvement of Flattop Windows with Semi-Infinite Optimization”. In: *The 6th International Conference on Optimization: Techniques and Applications*. 2004.

Scientific Instrument Reference

[138] *SR1 Audio Analyzer Operation Manual*. Stanford Research Systems. Jan. 2014. URL: https://www.thinksrs.com/downloads/pdfs/manuals/SR1am.pdf.

[139] *FD 1-40 Frequency Downconverter, Instructions and Manual*. Stahl-Electronics. Feb. 5, 2014. URL: https://www.stahl-electronics.com/bilder/FD40-Manual_1V1.pdf.

[140] *Keysight Trueform Series Waveform Generator Operation and Service Guide*. Keysight Technologies, Inc. Oct. 2015. URL: https://rfmw.em.keysight.com/bihelpfiles/Trueform/webhelp/US/Default.htm?id=2197433.

[141] *FS725 Rubidium Frequency Standard, Operation and Service Manual*. Stanford Research Systems. Aug. 18, 2023. URL: https://www.thinksrs.com/downloads/pdfs/manuals/FS725m.pdf.

[142] *DG645, Digital Delay Generator, User manual*. Stanford Research Systems. Aug. 18, 2023. URL: https://www.thinksrs.com/downloads/pdfs/manuals/DG645m.pdf.

[143] Elisa Elena Jacquet. *Phase Methods for Precision Measurements at BASE*. July 28, 2022. URL: https://cds.cern.ch/record/2820017.

[144] *Absorptive SPDT RF Switch ZASWA-2-50DRA+*. Mini-Circuits. Sept. 18, 2019. URL: https://www.minicircuits.com/pdfs/ZASWA-2-50DRA+.pdf.

[145] *ZFRSC-42-S+, 2 Ways Resistive Power Splitter, DC - 4200 MHz, 50Ω*. Mini-Circuits. Apr. 23, 2019. URL: https://www.minicircuits.com/pdfs/ZFRSC-42+.pdf.

[146] *ZFRSC-2050+, 2 Ways Resistive Power Splitter, DC - 2000 MHz, 50Ω*. Mini-Circuits. Aug. 11, 2020. URL: https://www.minicircuits.com/pdfs/ZFRSC-2050+.pdf.

[147] *RC-8SPDT-A18, Absorptive SPDT, Mechanical Switch, DC - 18000 MHz, 50Ω*. Mini-Circuits. Apr. 1, 2024. URL: https://www.minicircuits.com/pdfs/RC-8SPDT-A18.pdf.

[148] *BBP-27R5+, Lumped LC Band Pass Filter, 24 - 31 MHz, 50Ω*. Mini-Circuits. Nov. 30, 2020. URL: https://www.minicircuits.com/pdfs/BBP-27R5+.pdf.

[149] *SHP-25+, Lumped LC High Pass Filter, 27.5 - 800 MHz*. Mini-Circuits. May 22, 2022. URL: https://www.minicircuits.com/pdfs/SHP-25+.pdf.

[150] *Magnetic Field Sensor FLC 100, Miniature fluxgate sensor*. Stefan Mayer Instruments. Nov. 9, 2021. URL: https://stefan-mayer.com/images/datasheets/Data-sheet_FLC-100.pdf.

[151] *Magnetic Field Sensor FLC3-70, Triaxial fluxgate sensor*. Stefan Mayer Instruments. Nov. 9, 2021. URL: https://stefan-mayer.com/images/datasheets/Data-sheet_FLC3-70.pdf.

[152] *MA46H073-1056, MA46 Series, Surface Mount GaAs Tuning Varactors*. Macom. Aug. 13, 2015. URL: https://cdn.macom.com/datasheets/MA46%20Series.pdf.